Studies of III-V ferromagnetic semiconductors

Mu Wang, B.Sc

Thesis submitted to the University of Nottingham

for the degree of Doctor of Philosophy

March 2012

Abstract

The III-V ferromagnetic semiconductor Gallium Manganese Arsenide ((Ga,Mn)As) is one of the most interesting and well studied materials in spintronics research area.

The first chapter is a brief introduction to spintronics, the properties of (Ga,Mn)As and the growth technique molecular beam epitaxy (MBE). Then the thesis presents a detailed study of the effect on the Curie temperature (T_C) of varying the growth conditions and post-growth annealing procedures for epitaxially grown (Ga,Mn)As materials. The results indicate that it is necessary to optimize the growth parameters and post-growth annealing procedure to obtain the highest T_C. From detailed magnetotransport studies, the carrier densities of high T_C (Ga,Mn)As and H-doped (Ga,Mn)As have been achieved. It is found that the anomalous Hall resistance is the dominant contribution even at room temperature for these samples, which means it is incorrect to obtain carrier densities directly from Hall slope at high temperature. The results also show that the as-grown and lightly annealed H-doped (Ga,Mn)As samples have relatively high Curie temperatures down to low carrier density which make them good candidates for showing strong gate control of ferromagnetism.

Besides (Ga,Mn)As, this thesis also discusses the studies of III-V ferromagnetic semiconductors (Ga,Mn)(As,P), (Al,Ga,Mn)As and some heterostructures based on these materials. The experimental investigation shows that a (Ga,Mn)(As,P) single layer grown on GaAs substrate has perpendicular anisotropy easy axis after annealing. It also demonstrates a method to suppress the diffusion of interstitial Mn ions during low temperature annealing from specific layers in (Al,Ga,Mn)As based heterostructures. The magnetometry study shows that the individual layers in the heterostructure have tailored magnetic properties, which makes this material useful for the further investigation of tunnelling magnetoresistance and spin transfer torque phenomena.

Acknowledgements

I want to thank all the people who supported me and offered me help during my Ph.D study. First and foremost, I owe my sincere gratitude to my supervisor Professor Bryan Gallagher for giving me the opportunity to study in University of Nottingham, one of the most famous universities in the world. Meanwhile, I greatly appreciate the academic staff in our group, Dr. Andrew Rushforth and Dr. Kevin Edmonds. They offered me a lot of suggestions on experiments and theory background since the first day when I joined the group. This thesis would not have been possible without their guidance and advice.

I want to express my thankfulness to Dr. Richard Campion and Prof. Tom Foxon for providing high quality samples. I want to give my special thanks to Christopher Pallender for supplying liquid helium whenever I needed it. I would also like to thank Dr. Oleg Makarovsky, Dr. Lyudmila Turyanska, Umaima Elfurawi, Ateeq Nasir and Nilanthy Balakrishnan for the support when I was using the large cryostat system in Wendy house. I am grateful to Dr. Aidan Hindmarch and Chris Staddon for helping me to complete X-ray reflectivity experiments. My thanks to Jas Chauhan, Dave Taylor and Dr. Chris Mellor for the clean room training, the help with fabrication work and the using of plasma enhanced chemical vapor deposition (PECVD) system. I would like to extend my thanks to the ever pleasant and helpful staff in School of Physics and Astronomy, David Holt, Robert Chettle, David Laird, Stephen Booth, Michael Parker for their technical support when the equipments failed to work.

I am indebted to my colleagues to support me, Dr Khashayar Khazan, Dr. Samanta Piano, Dr. Ehsan Ahmad, Dr. Adam Freeman, Dr. Victoria Grant, Dr. Chris King, Dr. Devin Giddings, Dr. Jacqueline Hall, Robin Marshall, Peter Wadley, Arianna Casiraghi, James Haigh, Lucy Goff, Duncan Parkes, Fintan McGee, and Bryn Howells. Many thanks for the friendship and great help during my stay in Nottingham. It is an amazing experience to study and work with them. Thanks to our collaborator, Prof. Kaiyou Wang and Dr. Lixia Zhao from SKLSM, Institute of Semiconductors, Chinese Academy of Sciences, Prof. Tomas Jungwirth, Dr. Kamil Olejník, and Dr. Jan Zemen from the Institute of Physics, Czech Academy of Sciences, and Prof. Andrew Irvine, Prof. Andrew Ferguson, Dr. Fang Dong, Chiara Ciccarelli from the University of Cambridge.

Finally, I should thank all my relatives and friends, especially my parents who I missed so much during the time when I was studying in England. Mum and Dad, thank you for the love and support.

List of Publications

M. Wang, R. P. Campion, A. W. Rushforth, K. W. Edmonds, C. T. Foxon and B. L .Gallagher "Achieving high Curie temperatures in (Ga,Mn)As" Appl. Phys. Lett. **93**, 132103 (2008).

A. W. Rushforth, M. Wang, N. R. S. Farley, R. P. Campion, K. W. Edmonds, C. R. Staddon, C. T. Foxon and B. L. Gallagher "Molecular beam epitaxy grown (Ga,Mn)(As,P) with perpendicular to plane easy axis" J. Appl. Phys. **104**, 073908 (2008).

J. A. Haigh, M. Wang, A. W. Rushforth, E. Ahmed, K. W. Edmonds, R. P. Campion, C. T. Foxon and B. L. Gallagher "Manipulation of the magnetic configuration of (Ga,Mn)As nanostructures" Appl. Phys. Lett. **95**, 062502 (2009).

A. Casiraghi, A. W. Rushforth, M. Wang, N. R. S. Farley, P. Wadley, J. L. Hall, C. R. Staddon, K. W. Edmonds, R. P. Campion, C. T. Foxon, and B. L. Gallagher "Tuning perpendicular magnetic anisotropy in (Ga,Mn)(As,P) by thermal annealing" Appl. Phys. Lett. **97**, 122504 (2010).

S. Piano, R. Grein, C. J. Mellor, K. Výborný, R. Campion, M. Wang, M. Eschrig, and B. L. Gallagher "Spin polarization of (Ga,Mn)As measured by Andreev spectroscopy: The role of spin-active scattering" Phys. Rev. B **83**, 081305(R) (2011).

S. Piano, X. Marti, A. W. Rushforth, K. W. Edmonds, R. P. Campion, M. Wang, O. Caha, T. U. Schülli, V. Holý, and B. L. Gallagher "Surface morphology and magnetic anisotropy in (Ga,Mn)As" Appl. Phys. Lett. **98**, 152503 (2011).

P. Wadley, A. Casiraghi, M. Wang, K. W. Edmonds, R. P. Campion, A. W. Rushforth, B. L. Gallagher, C. R. Staddon, K. Y. Wang, G. van der Laan, and E. Arenholz "Polarized x-ray spectroscopy of quaternary ferromagnetic semiconductor(Ga,Mn)(As,P) thin films" Appl. Phys. Lett. **99**, 022502 (2011).

M. Wang, A.W. Rushforth, A. T. Hindmarch, K.W. Edmonds, R.P. Campion, C.T. Foxon, B.L. Gallagher "Suppression of interstitial Mn ion diffusion in (Al,Ga,Mn)As based heterostructures" In preparation.

List of Acronyms

AC	Alternating Current
ALD	Atomic Layer Deposition
AMR	Anisotropic Magnetoresistance
BEP	Beam Equivalent Pressure
CGS	Centimetre–Gram–Second system of units
DC	Direct Current
DMS	Dilute Magnetic Semiconductor
GMR	Giant Magnetoresistance
MBE	Molecular Beam Epitaxy
MPMS	Magnetic Property Measurement System
MRD	Materials Research Diffractometer
PECVD	Plasma Enhanced Chemical Vapor Deposition
PID	Proportional-Integral-Derivative
RHEED	Reflected High Energy Electron Diffraction
RSO	Reciprocating Sample Option
SI	International system of units
SOC	Spin-Orbit Coupling
SQUID	Superconducting Quantum Interference Device
STT	Spin Transfer Torque
TAMR	Tunnelling Anisotropic Magnetoresistance
TMR	Tunnelling Magnetoresistance
UHV	Ultra-High Vacuum
XRR	X-Ray Reflectivity

Contents

Appendix

Chapter 1

Introduction and background

This chapter is a brief introduction to spintronics in material science research. It presents the development of ferromagnetic semiconductor materials which is one of the most interesting topics in spintronics research area. Basic theories and experimental results, including structure, transport and magnetic properties of ferromagnetic semiconductor materials are discussed. The last section is an introduction to the molecular beam epitaxy (MBE) growth technique which is a standard method to produce ferromagnetic semiconductor materials.

1.1 Introduction to spintronics

Since the 1980s, the information revolution has changed people's daily life enormously and brought a new age based on the semiconductor industry. As time goes on the semiconductor devices become smaller, faster and more densely-packed, the existing materials and technologies are approaching their physical limits - the size of an atom or a molecule. Even before reaching this ultimate limit, the quantum effects increase significantly and need to be taken into account. For the development of future information technology, scientists are seeking new techniques concerning the design of both devices and system architecture.

In 1988, the giant magnetoresistance (GMR) effect was independently discovered by the research team of Peter Grünberg and the group of Albert Fert, which started a brand new research topic - spintronics. [1,2] Spintronics which refers to spin transport electronics is an emerging technology that exploits the intrinsic spin of the electron and its associated magnetic moment, in addition to its fundamental electronic charge, in solid-state devices. [3,4,5] A spintronics device needs two systems as a basic requirement. One can generate a spin polarized electron current, another should be sensitive to the electrons' spin polarization.

The spin-polarized current can be generated by using the GMR effect - a quantum mechanical effect that can be observed in thin film structures made up of alternating ferromagnetic and non-magnetic metal or semiconductor layers. The structure shows a significant decrease in electrical resistance when applying an external magnetic field. A typical GMR device consists of at least two layers of ferromagnetic materials separated by a spacer layer. When the magnetization direction of the ferromagnetic layers is anti-parallel with the electron spin direction, the electrons suffer high resistance due to magnetic scattering; conversely the parallel direction means low magnetic scattering and all the electrons can pass through the layers. When there is no applied magnetic field, the direction of magnetization of adjacent ferromagnetic layers is anti-parallel due to a weak anti-ferromagnetic coupling between layers. Because all the electrons need to pass at least one anti-parallel magnetization layer, the resistance is high. (Figure **1.1** right) When an external field is applied, all the magnetization directions of ferromagnetic layers become parallel. The electrons

whose spins are parallel with the direction of magnetization can go freely through the films, so the resistance becomes low. (Figure **1.1** left) At the same time a spin-polarized current can also be generated. This effect is very useful in modern hard drives, magnetic sensors, magneto-resistive random access memory (MRAM) and many other applications.

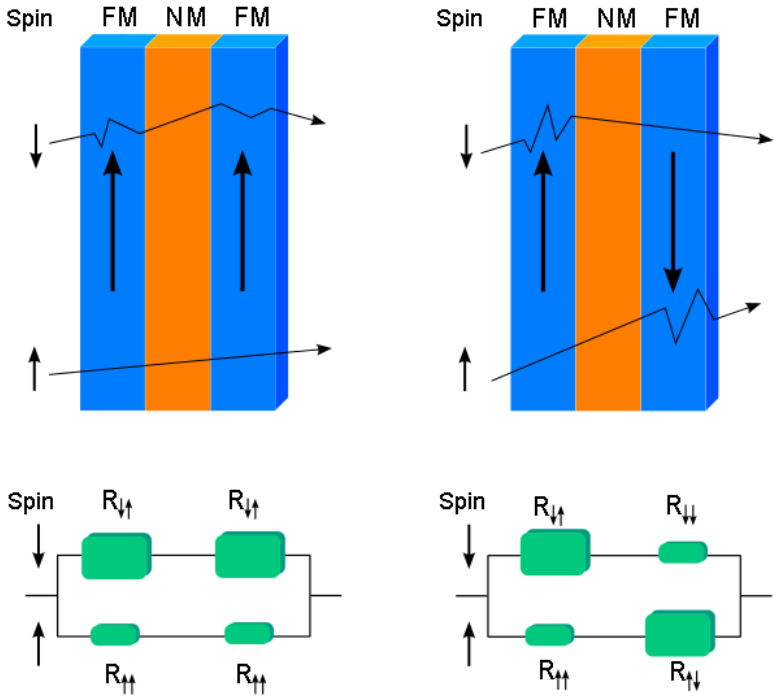

Figure 1.1 *Sketch map of Giant Magneto Resistance (GMR) effect.*

1.2 Diluted magnetic semiconductors (DMS)

1.2.1 Introduction

Many kinds of ferromagnetic materials can be used for making GMR structures and related devices. Magnetic semiconductor, which combines the properties of semiconductor and magnetic systems, is one of the most attractive spintronics materials. Semiconductors and magnetic materials are the most important components for making all kinds of electronics devices. As early as the 1970s, people began research work on alloying non-magnetic semiconductors with magnetic elements. [6,7] During that time, the work was mainly focused on the II-VI based semiconductors. These materials can show paramagnetic, spin glass, and ultimately long range anti-ferromagnetic behavior due to the anti-ferromagnetic exchange

among the spins. On the other hand, the (III,Mn)V based DMS developed very quickly, and a lot of progress has been made during the last 20 years.

1.2.2 The (III,Mn)V DMS system

Since the 1990s, with development of the non-equilibrium crystal growth technique, the (III,Mn)V ferromagnetic semiconductors have been produced. The first one, (In,Mn)As has been grown by Ohno *et al.* in 1992, [8] with the Curie temperature (T_C) approximately 7K. Four years later, in 1996, the (Ga,Mn)As with much higher T_C (75K) was produced by Ohno *et al.* [9] The percentage of Mn in these systems is high enough for interesting magnetic activity.

Compared to II-VI DMS systems, ferromagnetic (Ga,Mn)As could be more useful for making magnetic field controllable devices. Since GaAs is already a widely used semiconductor material, it would be much easier for (Ga,Mn)As based devices to be integrated with traditional semiconductor technology. The Mn atoms also introduce hole carriers, making (Ga,Mn)As a p-type semiconductor which can be used as a source of spin-polarized currents. Thus, (Ga,Mn)As becomes a good candidate for making spintronics devices and is the most widely-studied ferromagnetic semiconductor.

1.2.3 Introduction to the Gallium Manganese Arsenide

The III-V semiconductor Gallium Arsenide (GaAs) has a zinc-blende (also named sphalerite) crystal structure, which comprises of two interpenetrating face-centered cubic (fcc) sub-lattices, one of gallium ions and one of arsenide ions, displaced by a quarter of a lattice parameter along the [111] direction. The lattice constant is 5.653Å, the band gap at 300K is 1.424eV, and the magnetic behavior is diamagnetic.

The lattice structure of (Ga,Mn)As is identical to GaAs, except a few percent of Ga atoms have been substituted by Mn atoms, and each substitutional Mn contributes $5\mu_B$ local moment and one hole. (Figure **1.2**) As the Mn acts as the source of the hole and spin, the (Ga,Mn)As does not only exhibit the p-type semiconductor transport phenomena, but also has some correlated ferromagnetic properties.

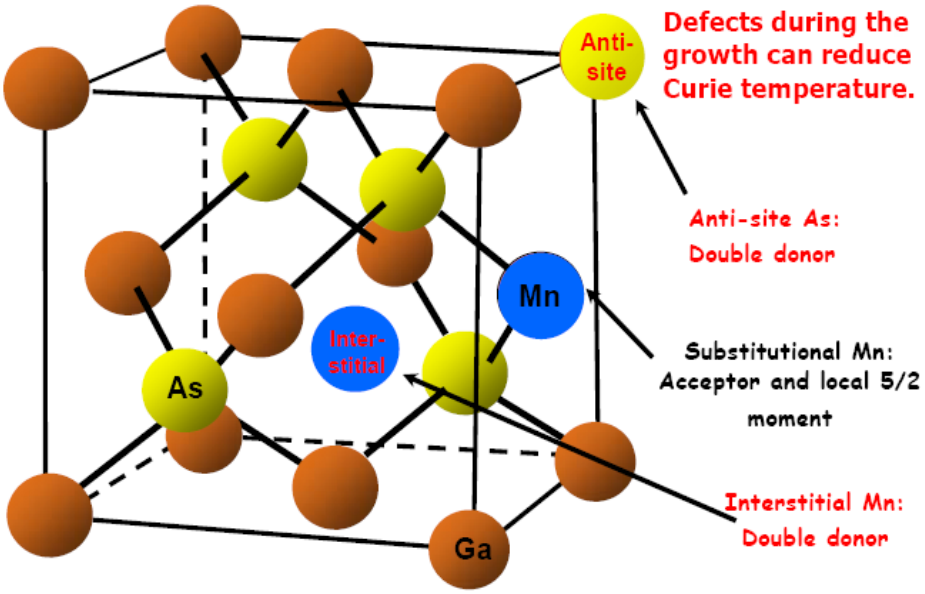

Figure 1.2 *The crystal structure of (Ga,Mn)As.*

The Zener model, [10,11] originally proposed for magnetic metals, can be used to describe the delocalized or weakly localized hole-mediated ferromagnetism in (Ga,Mn)As [12]. In (Ga,Mn)As, the indirect exchange between local d-shell moments of the Mn atoms is mediated by the p-band itinerant holes. Through the anti-ferromagnetic Mn-hole exchange interaction, the substitutional Mn can order ferromagnetically. This model predicts a relation between Curie temperature (T_C), the effective Mn density (Mn_{eff}) and the carrier density (p) in the form:

$$T_C \propto Mn_{eff}\, p^{1/3} \tag{1-1}$$

which has been proved experimentally. [13,14]

In addition to the substitutional Mn, there are some defects in the (Ga,Mn)As system during the non-equilibrium MBE growth. One of the most important defects is the interstitial Mn [15] (Figure **1.2**), which form naturally when the Mn doping levels greater than ~2.5%. [14] The interstitial Mn ions act to compensate the charge carriers (holes) that mediate the ferromagnetic interaction and the magnetic moments of the substitutional Mn ions, and result in a decrease of the electrical conductivity, the density of effective Mn (the density of substitutional Mn subtracts interstitial Mn) and the T_C. The post-growth annealing at low temperatures (~200°C, <growth temperature) allows interstitial Mn ions to be removed from the lattice by diffusion of the ions to the surface where they are passivated. [16] Hence, this procedure

increases the density of effective Mn and holes which leads to a higher T_C. [17,18]. Chapter 2 will present detail study of post-growth annealing procedure of (Ga,Mn)As. There are also some other defects such as As anti-sites [19] and metallic MnAs clusters, which are complicated but less important compare to the interstitial Mn defect. [16]

Although the amount of Mn is relatively small in (Ga,Mn)As, it gives a dramatic modification of the magnetic properties. However, the highest T_C is still well below 200K, [20,21] (Figure **1.3**) and it is necessary to increase the T_C above room temperature for (Ga,Mn)As to be useful in device applications.

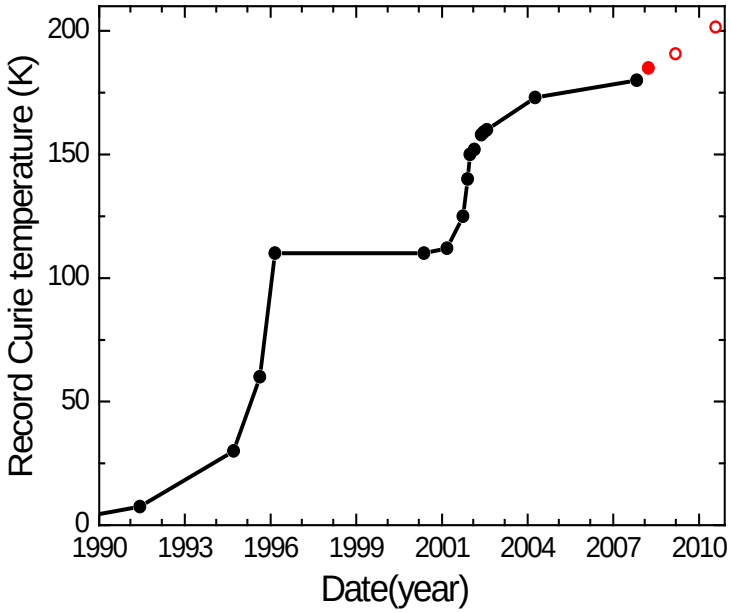

Figure 1.3 *Record Curie temperature of ferromagnetic semiconductor (Ga,Mn)As. For the red points there are some problems in the way the T_C values were obtained (see discussion in Section 1.5.4).*

1.3 Magnetic anisotropy and anisotropy magnetoresistance

1.3.1 Magnetic anisotropy

Magnetic anisotropy is the dependence of internal energy of a ferromagnetic material on the direction of its magnetization. There are several types of anisotropy, magnetocrystalline anisotropy (crystal anisotropy), shape anisotropy, stress anisotropy, exchange anisotropy and anisotropy induced by magnetic annealing,

plastic deformation, and irradiation. [22]

Only the magnetocrystalline anisotropy is an intrinsic property of the material, and it is due mainly to the spin-orbit coupling (SOC) [22] which is an interaction of an electron's spin with the orbital motion. The SOC in most materials is weak compared to the spin-spin and orbit-lattice coupling. The energy to rotate the moments away from easy direction (called anisotropy energy) is just the energy required to overcome the SOC, and the density of the anisotropy energy in the crystal is measured by the magnitude of the anisotropy constants K_1, K_2, *etc*. It is usually impossible to calculate the values of these constants from the first principles because the complexity of the electronic structure, [22] but semi-quantitative values can be obtained in the case of (Ga,Mn)As. [13,23] A lot of experimental research on the magnetic anisotropy in (Ga,Mn)As has been done and the result shows (Ga,Mn)As films have in-plane uniaxial magnetic anisotropy. [24,25,26,27] Most of the (Ga,Mn)As films studied in this thesis with high T_C, have uniaxial anisotropy with the easy axis along [1-10] crystal orientation. (See Chapter 2)

As to the extrinsic properties of the material, the shape anisotropy is due to the shape of a grain or the shape of the single crystal material, and the stress anisotropy is created by the mechanical stress in the crystal structure. The shape anisotropy is not important in (Ga,Mn)As material due to its small saturation magnetization. The details of stress anisotropy in (Ga,Mn)As thin film can be found in Chapter 3 of C. S. King's thesis (University of Nottingham). More information about magnetic anisotropy can be found in ref. 22 and 28.

1.3.2 Magnetoresistance in (Ga,Mn)As

Magnetoresistance is the change of resistance when applying an external magnetic field. Figure **1.4** shows a typical magnetoresistance measurement at 4.2K for a fully annealed 12% Mn (Ga,Mn)As sample in which the current is along the [1-10] direction. This sample has a magnetic easy axis along the [1-10] direction.

The longitudinal resistance (R_{xx}) firstly shows positive magnetoresistance at low fields when the external magnetic field is applied along the [110] and [001]

directions. This is attributed to the rotation of the magnetization from the magnetic easy axis into the magnetic field direction. This effect originates from the magnetic anisotropy [29,30], and is discussed in the next section. R_{xx} then shows negative magnetoresistance with increasing magnetic field, with a slope that is independent of the direction of magnetic field. One explanation is ascribed to increasing magnetic order [31] or to the weak localization in ferromagnetic (Ga,Mn)As at low temperature which can be suppressed by a sufficiently strong magnetic field. [32,33]

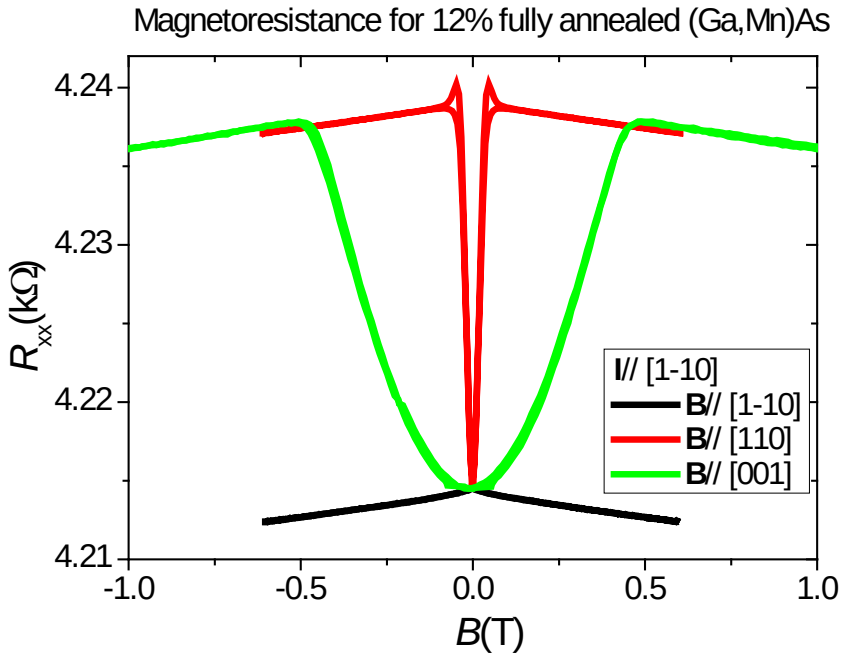

Figure 1.4 *Magnetoresistance of 12% fully annealed (Ga,Mn)As measured at 4.2K*

1.3.3 Anisotropic magnetoresistance (AMR) in (Ga,Mn)As

The AMR is the change of resistance as a function of the angle of magnetization with respect to the crystal orientation and current direction. It is intrinsically related to the SOC, which induces the mixing of spin-up and spin-down spin states. The mixing of states depends on the magnetization direction. [34]

In (Ga,Mn)As, the substitutional Mn is in a d^5 high-spin state, with small orbital moment. The anisotropy effects are therefore due to the p-d interactions between Mn and charge carriers, which reside in the valence band of the host semiconductor, where spin-orbit coupling is large. A (Ga,Mn)As thin film has a relatively strong spin-orbit coupling, hence it can show relatively strong anisotropic

magnetoresistance. [29,35] (Polar plots of the AMR measured for two Hall bars fabricated from a fully annealed 12% (Ga,Mn)As film are shown in Figure **1.5**) The phenomenological decomposition of the AMR of (Ga,Mn)As into various terms allowed by symmetry is obtained by extending the standard phenomenology [36] to systems with cubic [100] plus uniaxial [110] anisotropy. The AMR of the Hall bar measurements can be written as follows, ignoring the negligible higher-order crystalline and crossed terms. [37]

$$\frac{\Delta\rho_{xx}}{\rho_{av}} = \frac{(\rho_{xx} - \rho_{av})}{\rho_{av}} = C_I \cos 2\phi + C_U \cos 2\psi + C_C \cos 4\psi + C_{IC} \cos(4\psi - 2\phi) \quad (1\text{-}2)$$

where ρ_{av} is the ρ_{xx} averaged over 360^o in the plane of the film, C_I, C_U, C_C and $C_{I,C}$ are the coefficients of the noncrystalline term, the lowest order of uniaxial and cubic crystalline terms, and a crossed noncrystalline/ crystalline term respectively. ϕ is the angle between the magnetization vector **M** and the current **I**, and ψ is the angle between **M** and the [110] crystal direction. $\psi = \phi - 90°$ when the current is along [1-10], and $\psi = \phi$ when current is along [110].

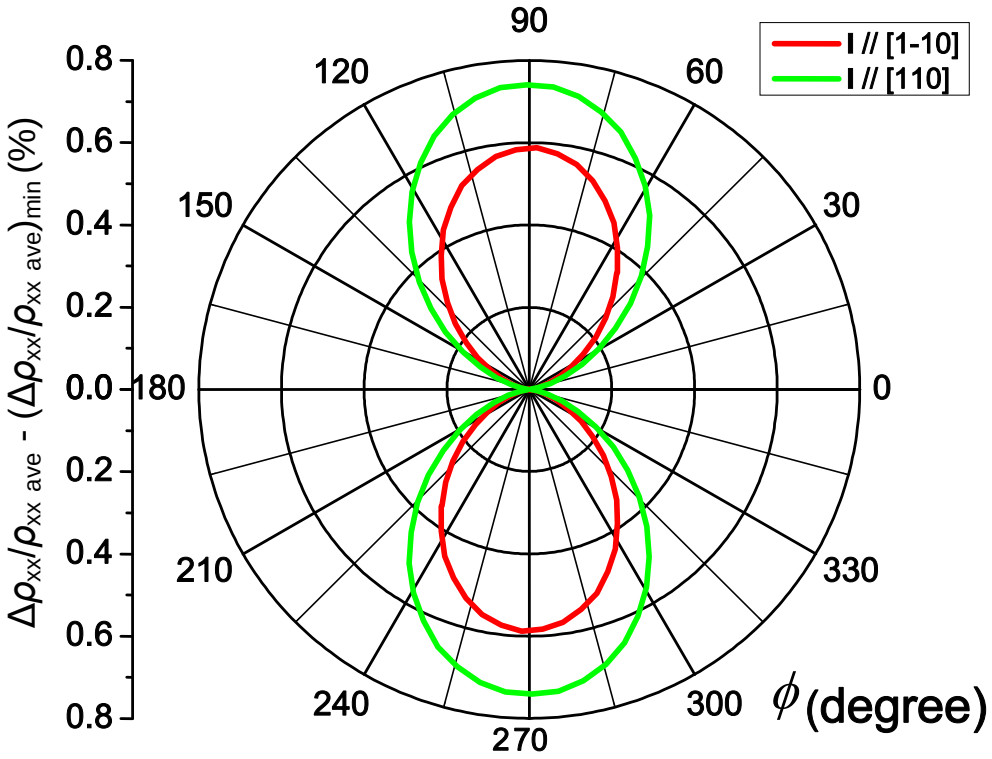

Figure 1.5 *The AMR of two nominal 12% Mn fully annealed (Ga,Mn)As Hall bars, measured at 4.2K with B= 0.6T. ϕ is the angle between the magnetization vector* **M** *and the current* **I**

The combination of an AMR effect of up to several percent and a large absolute value of the sheet resistance gives rise to a giant transverse AMR. This effect arises as a result of the non-equivalence of components of the resistivity tensor which are perpendicular and parallel to the magnetization direction, leading to the appearance of off-diagonal resistivity components. (Figure **1.6**) The transverse AMR can be described in the form: [37]

$$\frac{\Delta\rho_{xy}}{\rho_{av}} = \frac{(\rho_{xy} - \rho_{av})}{\rho_{av}} = C_I \sin 2\phi - C_{IC} \sin(4\psi - 2\phi) \qquad (1\text{-}3)$$

The ρ_{av} is still the ρ_{xx} averaged over 360° in the plane of the film.

Details studies on anisotropic magnetoresistance properties of (Ga,Mn)As are presented in ref. 37.

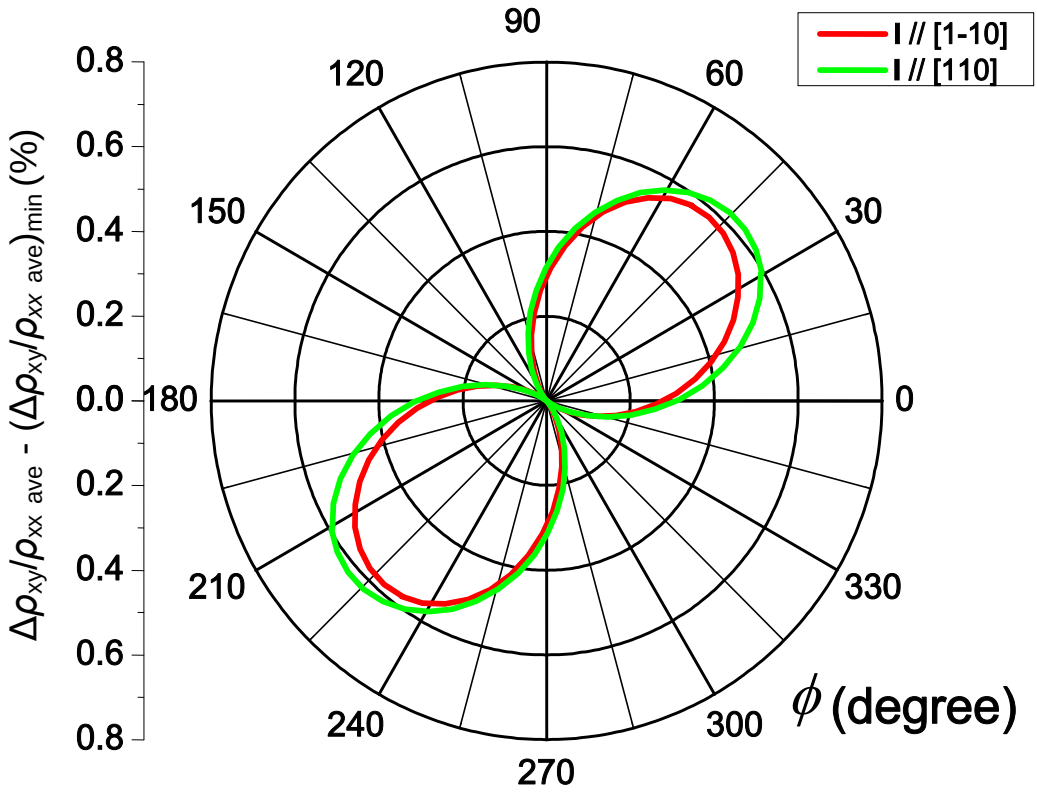

Figure 1.6 *The transverse AMR of two nominal 12% Mn fully annealed (Ga,Mn)As Hall bars, measured at 4.2K with 0.6T magnetic field. ϕ is the angle between the magnetization vector* **M** *and the current* **I**

1.4 Hall Effect

1.4.1 Ordinary Hall Effect

The Hall Effect which was found in 1879 by Edwin H. Hall [38] is a very important discovery in the material science research area. It provides a simple way to get the information of carrier type and carrier densities of the semiconductor materials.

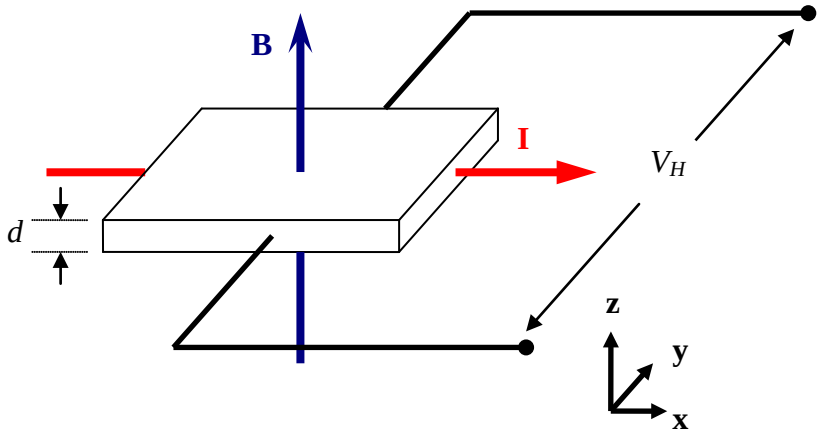

Figure 1.7 *The vector diagram for the Hall Effect. Current carriers is (1) positively charged (p type) holes, $V_H>0$ (2) negative charged (n type) electrons $V_H<0$*

A typical experimental geometry is presented in Figure **1.7**. The charge carriers moving in a direction (**x** axis) perpendicular to an applied magnetic field (**z** axis), have been “pressed toward one side of the conductor" (**y** axis) [38] by the Lorentz force.

Charge builds up on the surface of the side of conductor, and the potential drop across the two sides of the sample is known as the Hall voltage (V_H).V_H has a relation with the current (**I**), the perpendicular magnetic induction (**B**), the sample thickness (*d*), and the carrier density (*p*) in the form:

$$V_H = \frac{IB}{ped} \tag{1-4}$$

where *e* is the elementary charge. The carrier density and the type of the carrier can be determined by measuring the Hall voltage. Rearranging Eq. 1-4, the Hall resistance is described:

$$R_{xy} = \frac{V_H}{I} = R_0 B \text{ with } R_0 = \frac{1}{ped} \tag{1-5}$$

1.4.2 Anomalous Hall Effect

One year after the discovery of the Hall Effect, Edwin H. Hall found that the "pressing electricity" effect was ten times larger in the ferromagnetic conductor iron [39] than in non-magnetic conductors, which came to be known as the Anomalous Hall Effect (AHE) in the ferromagnetic materials. This additional contribution to the Hall resistance depends on the magnetization of the materials and can be described in the form $R_A \mu_0 M$, where M is the value of perpendicular magnetization component, and $\mu_0 = 4\pi \times 10^{-7}\ \mathrm{N/A^2}$ is the permeability of free space.

In a ferromagnetic semiconductor (Ga,Mn)As, the anomalous term gives a non-zero contribution to the Hall slope even at high magnetic fields, due to the isotropic negative magnetoresistance. (Section 1.3.2 discussed the magnetoresistance of (Ga,Mn)As) The anomalous coefficient R_A is an unknown function of the resistivity, which in turn is dependent on the magnetic field, and is typically larger than Ordinary Hall resistance (R_0) by a factor of ~100-1000. It has been found that R_A has a relation with the longitudinal resistance (R_{xx}) in the form:

$$R_A \propto R_{xx}^n \tag{1-6}$$

The Hall resistance in the ferromagnetic materials can be described by the sum of ordinary and anomalous terms.

$$R_{xy} = R_0 B + R_A \mu_0 M = R_0 B + C R_{xx}^n M \tag{1-7}$$

There are a lot of theories on the scaling exponent n for (Ga,Mn)As. In the extrinsic mechanism models, n is equals to 1 (skew-scattering [40]) or 2 (side-jump [41]). In the intrinsic mechanism models, T. Jungwirth *et al.* obtained the anomalous Hall conductance of (Ga,Mn)As from the Berry phase accumulated by a quasi-particle wave function upon traversing closed paths on the spin-split Fermi surface of a ferromagnetic state and predicts n is equals to 2. [42] There is also a lot of experimental work on the anomalous Hall Effect of (Ga,Mn)As. [43-46] Chapter 2 will discuss some of my experimental work on obtaining carrier densities of (Ga,Mn)As from Hall measurement.

1.5 The Curie temperature of ferromagnetic (Ga,Mn)As

1.5.1 The introduction to Curie temperature

The Curie temperature (T_C) (named after Pierre Curie who discovered this transition in the ferromagnetic substances) is the temperature at which materials show very strong critical behavior of changing from the ferromagnetic (a state has some alignment of the magnetic moments and a spontaneous magnetization) into paramagnetic phase (a completely disordered state). [47] Figure **1.8** shows the computed values of the T_C for various p-type semiconductors with Mn concentration equals to 5% and carrier density equals to $3.5\times10^{20}\,cm^{-3}$ by T. Dietl *et al.* [12] The next section will present several methods that are used to obtain the T_C of (Ga,Mn)As.

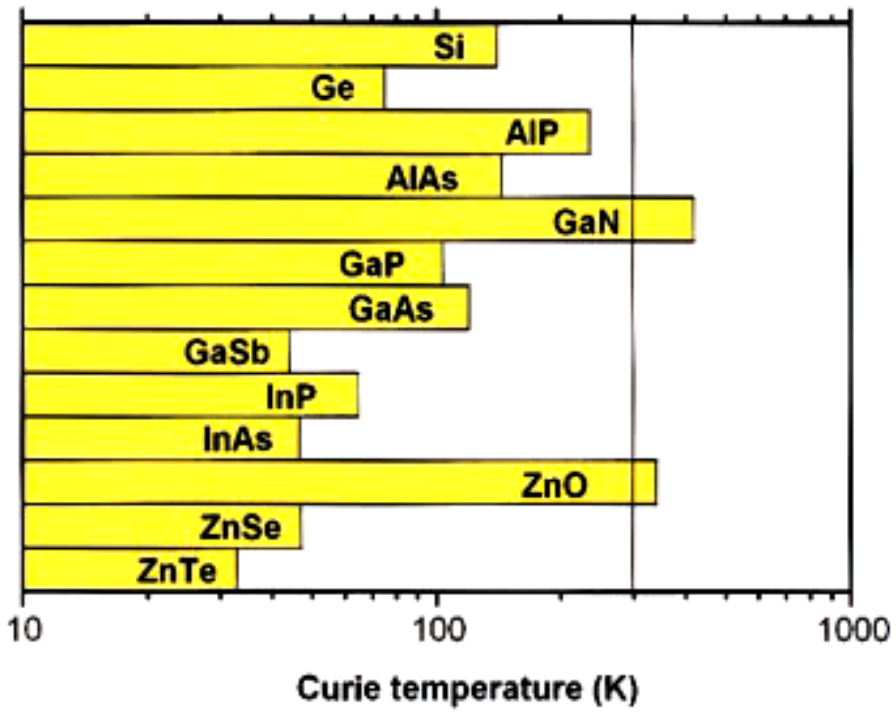

Figure 1.8 *The computed values of the T_C for various p-type semiconductors with 5% Mn and $p=3.5\times10^{20}\,cm^{-3}$ by Zener model.* [12]

1.5.2 Magnetometry measurement

A standard method to obtain T_C is from the temperature dependent remnant magnetization by magnetometry measurements. The measurement was always made after a 1000 Oe field cool to 2K. Figure **1.9** shows a projection of this curve along [1-10] axis for a (Ga,Mn)As sample with 12% Mn. Because this high T_C (Ga,Mn)As sample has strong uniaxial anisotropy and is single domain, the remnant magnetization equals the projection of remnant magnetization along [1-10] easy axis.[27,48] The magnetization is reduced sharply to nearly zero at 177K (Inset) and changes are tiny above that temperature. Sometimes a small tail of the curve can be observed, due to the inhomogeneity of the sample and the small external magnetic field that remains in the system.

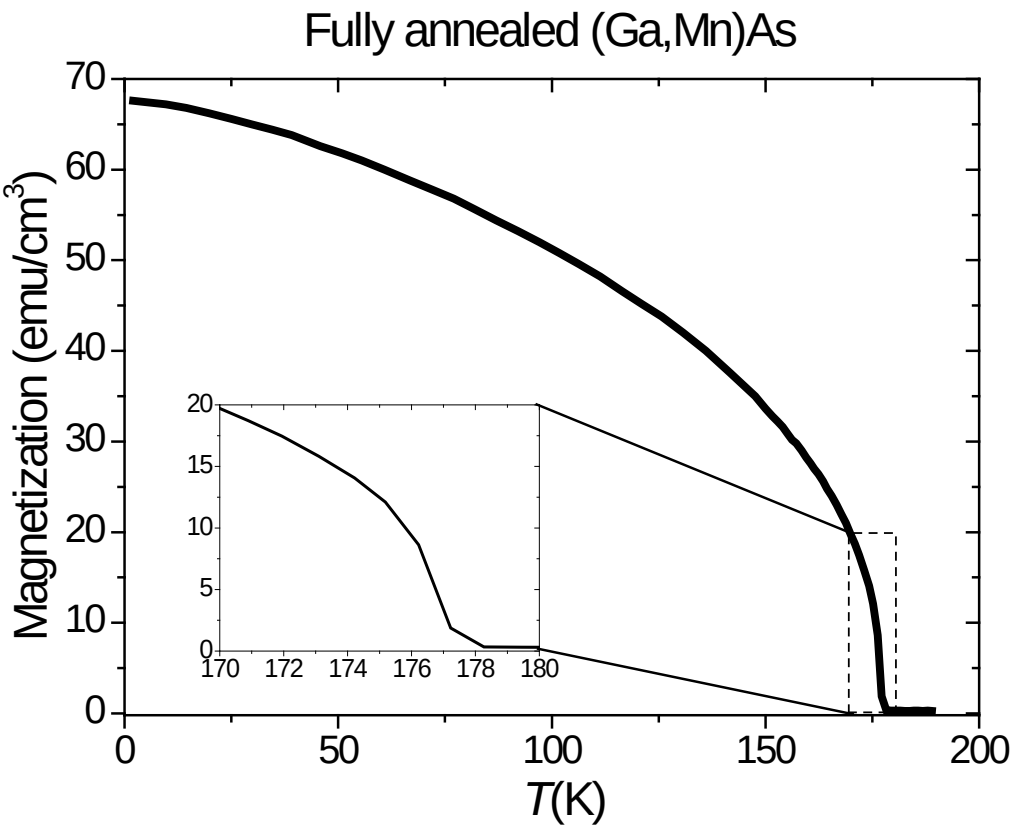

Figure 1.9 *Projection of the temperature dependent remnant magnetization along [1-10] for fully annealed 12% (Ga,Mn)As sample with T_C around 177K.*

1.5.3 Arrott plots

The T_C of ferromagnetic materials can also be obtained by using the Arrott plots method. [49,50] In the Landau theory of second-order transitions (including the paramagnetic/ferromagnetic phase transition at the Curie point), [51] the free energy F of the ferromagnetic system can be expanded in terms of the order parameter (the magnetization, **M**) as follows:

$$F = F_0 - HM + aM^2 + bM^4 \tag{1-8}$$

where a and b are the coefficients. By minimizing the free energy F,

$$\frac{dF}{dM} = -H + 2aM + 4bM^3 = 0 \tag{1-9}$$

The relation between H/M and M^2 is

$$M^2 = \frac{1}{4b}\frac{H}{M} - \frac{a}{2b} \tag{1-10}$$

The relation between magnetic induction and magnetic field intensity in SI units is

$$\mathbf{B} = \mu_0(\mathbf{H} + \mathbf{M}) \Rightarrow \mathbf{H} = \frac{\mathbf{B}}{\mu_0} - \mathbf{M} \tag{1-11}$$

The Eq. 1-10 can be written as

$$M^2 = \frac{1}{4b}\frac{B}{\mu_0 M} - \frac{a + 0.5}{2b} \tag{1-12}$$

So M^2 is linearly related to B/M. The intercept on the M^2 axis determines the magnetic state since it is positive below T_C and negative above T_C.

It is expected that (Ga,Mn)As shows non-mean-field behavior when close to T_C, and it is better to use modified Arrott plots [52] to get a more accurate description.

$$\left(\frac{M}{M_1}\right)^{1/\beta} = \left(\frac{H}{M}\right)^{1/\gamma} - \frac{T - T_C}{T_1} \tag{1-13}$$

In this equation, M_1 and T_1 are the constants. β and γ are the critical exponents, which have different values in different theory models (mean field, Heisenberg, Ising). In mean-field theory, with β =0.5 and γ =1, Eq. 1-13 turns back to Eq. 1-10.

However, modified Arrott plots with critical exponents from three different models give similar results for determining T_C. (Less than 1K in difference) The details of critical behaviors of (Ga,Mn)As can be found in 3rd Chapter of R. A. Marshall's

Thesis (University of Nottingham).

Because of the presence of anomalous Hall Effect, magnetotransport measurements provide information on the magnetic properties of (Ga,Mn)As layer. As mentioned before, the anomalous part is much larger than the ordinary part. In that case, Eq. 1-7 can be changed to

$$R_{xy} \approx R_A \mu_0 M = C R_{xx}^n \mu_0 M$$

$$\Rightarrow M \propto \frac{R_{xy}}{R_{xx}^n} \tag{1-14}$$

which means the temperature dependence of the remnant magnetization **M** can be described by R_{xx} and R_{xy} .

Eq. 1-12 can be rewritten in the form:

$$\left(R_{xy} \middle/ R_{xx}^n \right)^2 = C_1 \frac{B}{R_{xy} \middle/ R_{xx}^n} - C_2 \tag{1-15}$$

This suggests that the T_C can be obtained from magnetotransport measurements by using Arrott plots. Figure **1.10** is an example of Arrott plots for a 12% (Ga,Mn)As sample (using n=2) which shows T_C is around 179K.

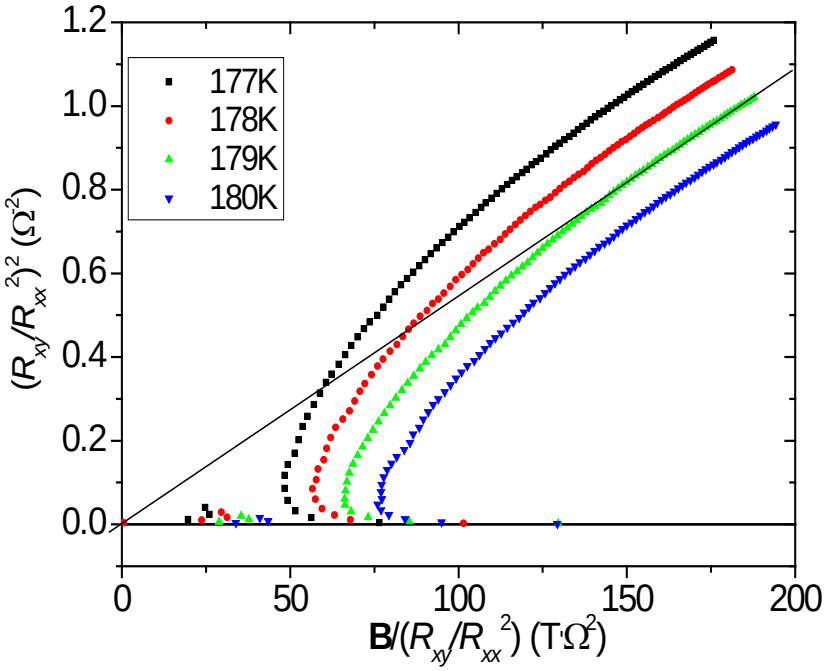

Figure 1.10 *Arrott plots graph of a previous 12% (Ga,Mn)As sample which shows the T_C is around 179K. The sample was measured in the ^{4}He cryostat system with ±0.6T external magnetic field.*

1.5.4 Transport measurement without magnetic field

(Ga,Mn)As has some unique magnetic and magnetotransport properties, and there are still a lot of questions about the description of the critical contribution to resistivity. In previous studies, it has been noticed that the peak point of the *R vs. T* curve is close to T_C. [53, 54] (Figure **1.11**) With the theories of coherent scattering from long wavelength spin fluctuations [55], Haas et al. explained this behavior in Eu-chalcogenide magnetic semiconductors, [56] which can be used for the (Ga,Mn)As system. Without applying any magnet field during the measurement, this method could be useful to obtain the T_C of (Ga,Mn)As sample. In 2011, Zhao's group reported a new record for (Ga,Mn)As with T_C above 200K with a error bar of ±5K, by defining T_C as the peak point of R_{xx} *vs. T* curve. [57] (Figure **1.12**, also red points in Figure **1.3**)

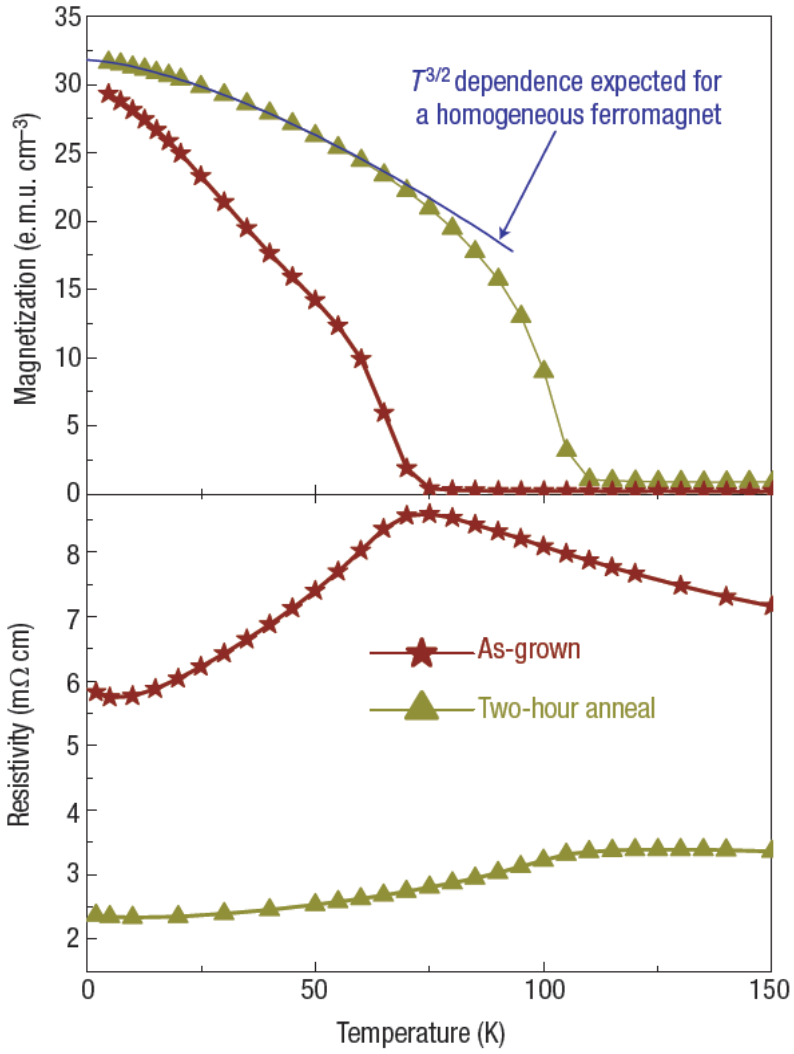

Figure 1.11 *The temperature dependence of the magnetization and resistivity of (Ga,Mn)As (As-grown and annealed)* [54]

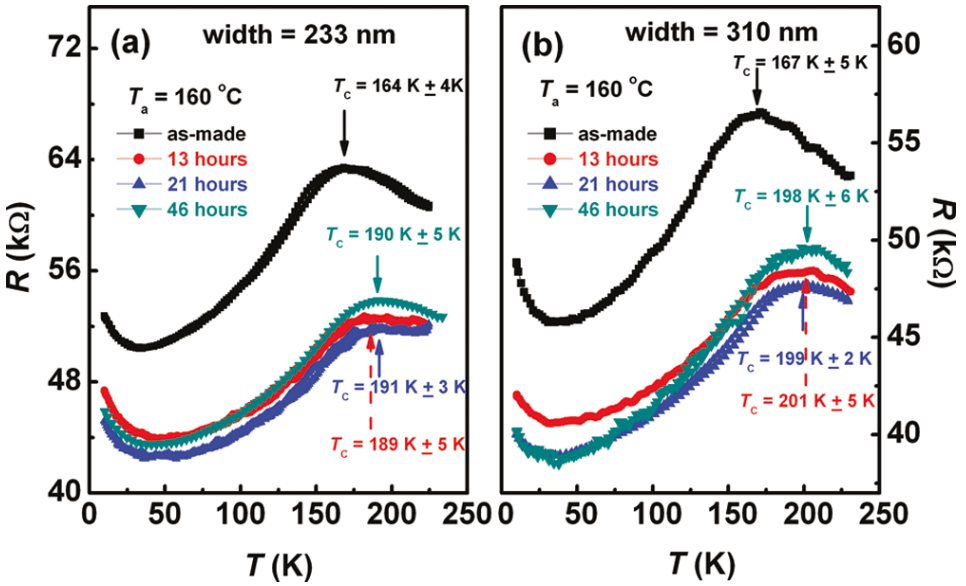

Figure 1.12 *The temperature dependent longitudinal resistance (R_{xx}) curves of two series of nano-wires with widths of 233 nm (a) and 310 nm (b) in the as-made state and after different annealing times as indicated.* [57] *It shows the "new record" T_C above 200K for (Ga,Mn)As nano-wires.*

At the same time, there is another method to achieve T_C by transport measurement. In 2008, Novák *et al.* [21] reported that there is a pronounced peak at T_C in dR_{xx}/dT curves in thin (Ga,Mn)As epilayers prepared under optimized growth and post-growth annealing conditions, with nominal Mn doping ranging from 4.5% to 12.5% and corresponding Curie temperatures from 81 to 185 K. (Figure **1.13**) It is associated with the critical behavior and can be explained in terms of large wave vector scattering of carriers from spin fluctuations, which is based on the theory from Fisher and Langer [58]. They compared the data from magnetometry and transport measurements, and shown the T_C is more close to the singularity point of dR_{xx}/dT curves for the annealed sample. However, it is difficult to make that comparison because the two samples from same wafer have been measured in two different cryostat systems. Due to the inhomogeneity of the sample wafer and the different thermometers in two systems, there could be a relatively large error of T_C and temperature for a proper critical behavior study.

Recently, the group in Nottingham started to introduce transport measurements into the SQUID system, which makes it is possible to obtain the magnetic and transport properties of one sample at the same time. From a series of detailed measurements (measurements were taken in 0.1K per step), it has been proved that the T_C is close to

the peak point of dR_{xx}/dT rather than of R_{xx} *vs.* T for several fully annealed high T_C samples. Figure **1.14** shows the results of one sample with T_C around 183K and the peak point of R_{xx} *vs.* T is between 195K and 200K. Because of the precise temperature control system of the SQUID, the study of critical phenomena also has been done at the same time. More details of the measurements can be found in R. A. Marshall's thesis.

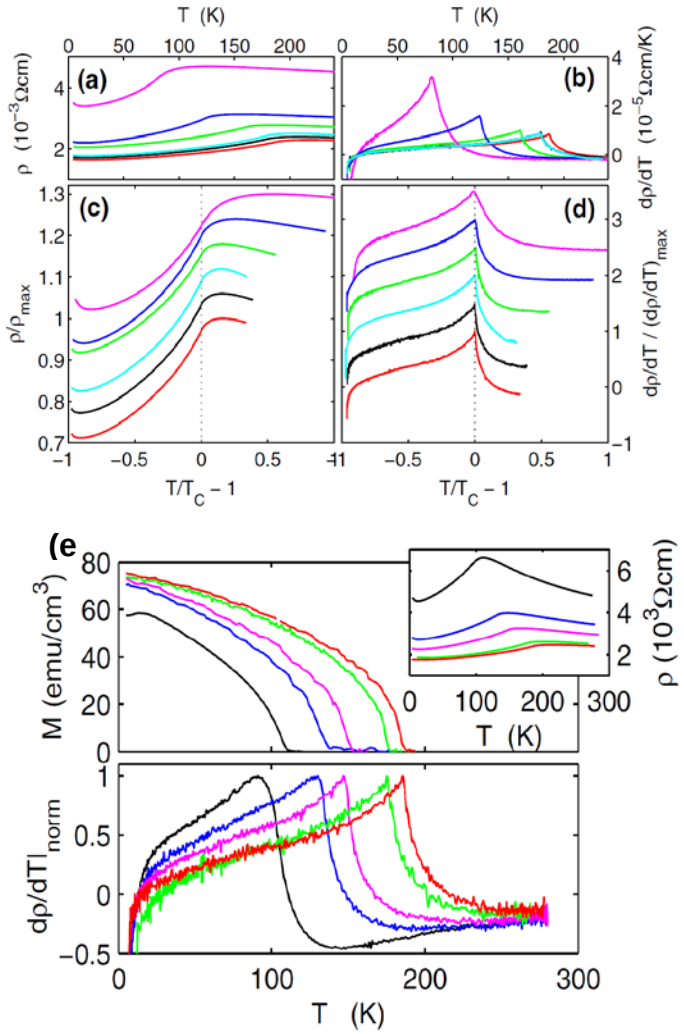

Figure 1.13 *(a) Resistivities ρ(T) and (b) temperature derivatives dρ/dT for optimized (Ga,Mn)As films (of thicknesses between 13 and 33 nm) prepared in Prague and Nottingham MBE systems. Data normalized to maximum ρ(T) and dρ/dT are plotted in (c) and (d), respectively. Curves in (a), (c), and (d) are ordered from top to bottom according to increasing Mn doping and Tc: 4.5% Mn-doped sample with T_C=81 K, 6% with 124 K, 10% with 161 K, 12% with 179 K (Prague and Nottingham samples), and 12.5% doped sample with 185 K Curie temperature. In (c) and (d), curves are offset for clarity. (e) Upper panel: Magnetization curves of one 12.5% Mn-doped (Ga,Mn)As specimen annealed in several successive steps. From left to right: as grown, 10, 40, and 120 minutes, and 14 hours annealed at 160ºC in air. Bottom panel: Normalized dρ/dT curves measured in the same annealing steps. Resistivity curves are shown in the inset with the highest ρ(T) corresponding to the as-grown state of the sample.* [21]

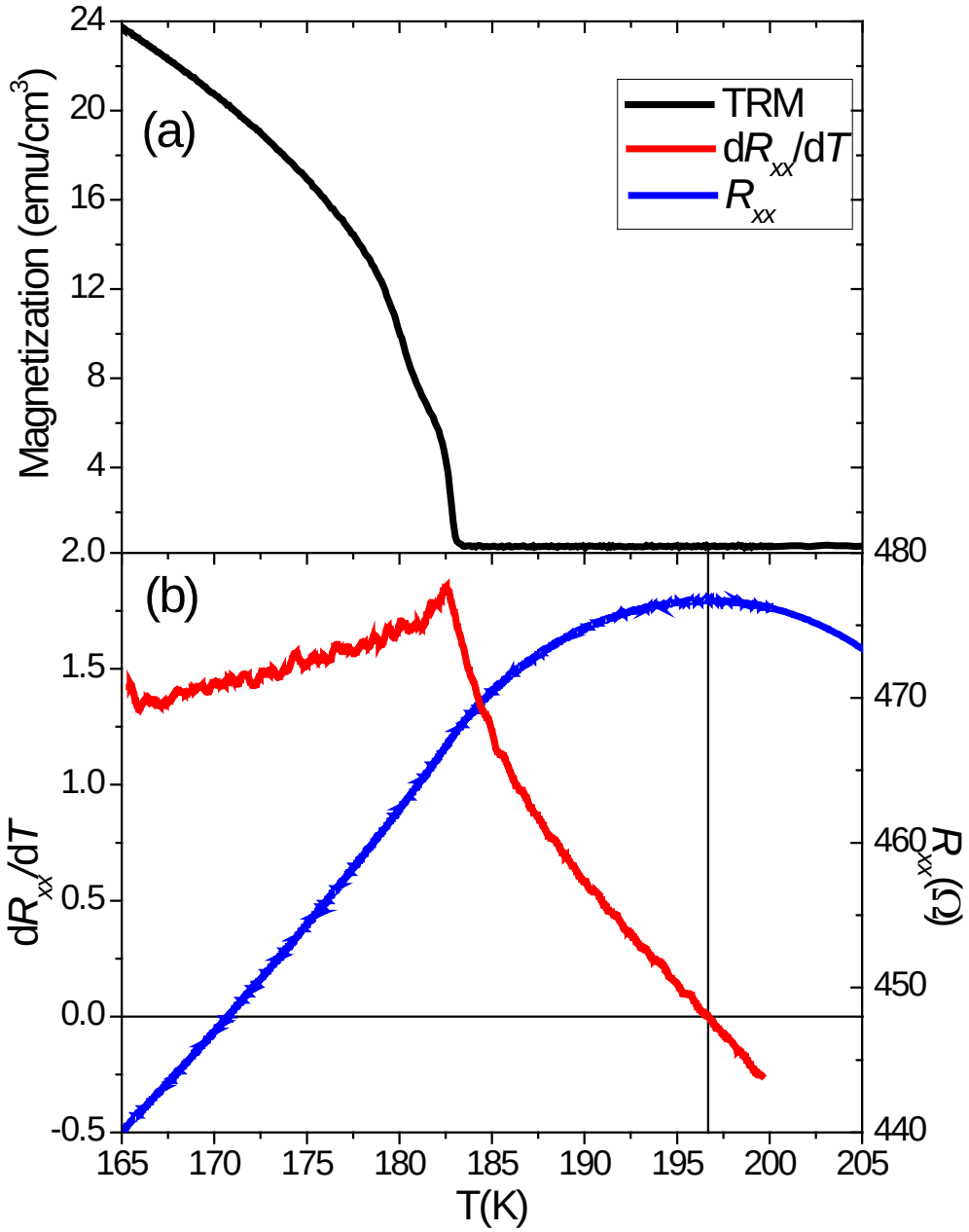

Figure 1.14 *(a) The temperature dependent remnant magnetization around T_C, (b) the dR_{xx}/dT and R_{xx} vs. T curve from transport measurement. The results come from the same sample measured at the same time in the SQUID magnetometer.*

1.6 Introduction to the molecular beam epitaxy (MBE) system

Ferromagnetic (Ga,Mn)As is intrinsically a non-equilibrium material, so it is very hard to put high percentage of Mn by using normal techniques (roughly 0.1% can be put into the GaAs system at equilibrium). As low temperature molecular beam epitaxy (LTMBE) growth allows Mn to be incorporated in GaAs at levels much higher than the equilibrium solubility limit, it has become a standard method of producing (Ga,Mn)As.

MBE is one kind of method to deposit single crystalline thin films, which allows precise control of the alloy composition, doping level and thickness of the layer down to a single layer of atoms. Epitaxy refers to the method of depositing a mono-crystalline film on a mono-crystalline substrate. The deposited film is called an epitaxial film or epitaxial layer. It was invented in the late 1960s at Bell Telephone Laboratories by A. Y. Cho and J. R. Arthur. [59]

Among several methods of depositing single crystals, MBE can grow materials one layer at a time - about 5nm per minute. However, the slow deposition rates require high vacuum or ultra-high vacuum (UHV)-10^{-8}Pa in order to achieve the same purity levels as other deposition techniques. In the MBE system, ultra-pure elements such as gallium, arsenic, manganese and other materials are heated in separate quasi-Knudsen effusion cells. They slowly sublimate and evaporate into the MBE chamber. Due to the ultra-high vacuum, the evaporated atoms have long mean free paths. The gaseous elements do not interact with each other or any other vacuum chamber gases until they reach the wafer. On the surface of the wafer, they may react with each other and form a single-crystal material. The growth surface, local bonding and topography as well as the relative size, abundance, diffusion length, supply and desorption rates of the adatoms are all factors that affect the growth.

The most important aspect of MBE is the slow deposition rates that allow surface kinetics to dominate the growth, especially at low temperatures. [60] Another important aspect is that growth is not necessarily a thermal equilibrium process. The resultant material can be meta-stable and therefore modified by annealing. However,

large deviations from equilibrium can lead to the introduction of unwanted phase separation or defects, such as when attempting to introduce very high doping levels. Defects that act to reduce the doping level may be encouraged, for example the formation of anti-site defects. Such a process is known as self compensation.

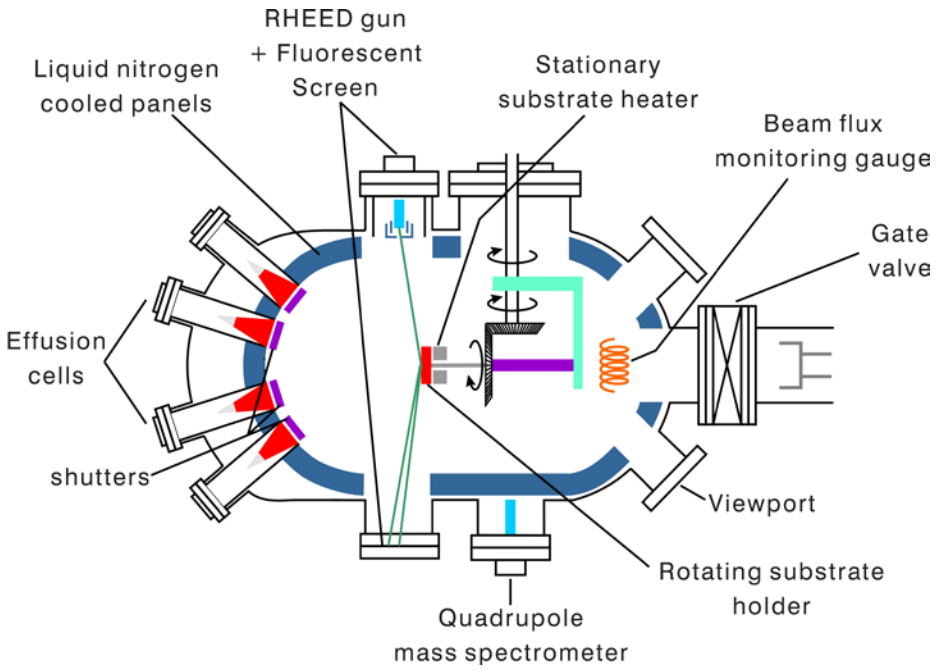

Figure 1.15 *The schematic of MBE chamber (from web page of MBE Laboratory in the Institute of Physics of the ASCR, Czech Republic)*

Because of the UHV environment in the MBE chamber, (Figure **1.15**) one of the most important factors - the growth temperature (T_g) at the surface of substrate - is quite difficult to measure. The way to get the temperature is from the heating of a thermocouple due to the re-radiation reflection from substrate. Normally thermocouples or optical pyrometers are used to monitor the temperature, however both of these two methods have problems for the MBE system. The thermocouples are more sensitive to the heater rather than the sample itself, while optical pyrometers are of limited use at temperatures less than 500ºC and are surface emissivity dependent. We need a bulk property that can be calibrated outside of the vacuum system. With the advent of sensitive reliable solid state spectrometers with nanometer resolution, real time band edge spectroscopy is viable and provides the solution of detecting T_g. It works by illuminating the sample with white light and passing the resultant reflected light to the spectrometer via an optic fibre. The

temperature dependence of the band gap has been experimentally determined, so that by measuring the wavelength of a material's absorption edge, the band edge spectroscopy is able to infer the band gap energy and therefore the temperature.

Reflection high energy electron diffraction (RHEED) is often used to monitor the growth of crystal layers during the operation. A RHEED system consists of an electron source (gun) and photo luminescent detector screen. The electron gun generates a beam of electrons which strike the sample at a very small angle relative to the sample surface. Incident electrons diffract from atoms at the surface of the sample, and a fraction of the diffracted electrons interfere constructively at specific angles and form regular patterns on the detector. The electrons interfere according to the position of atoms on the sample surface, so the diffraction pattern at the detector is a function of the sample surface. Therefore RHEED can provide information about the sample surface.

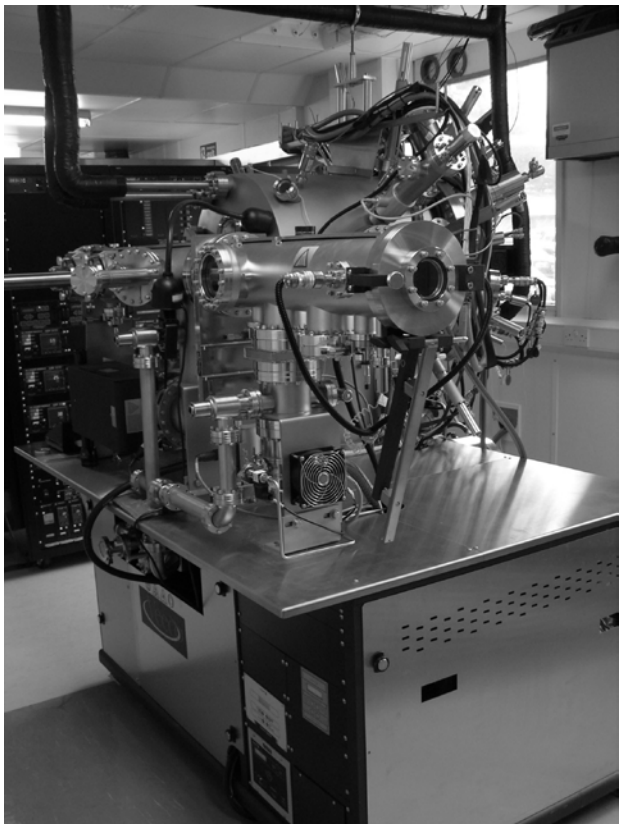

Figure 1.16 *The VARIAN GEN-III MBE system in the MBE group of School of Physics and Astronomy, University of Nottingham.*

The standard (Ga,Mn)As films were grown on (001) oriented semi-insulating GaAs substrates by a modified VARIAN GEN-III MBE system. (Figure **1.16**) The arsenic (As) flux was provided by a VEECO MK5 valved cracker, set to produce As_2. On a separate test sample, the growth rate was calibrated using RHEED oscillations [61] and the valve setting for As stoichiometry at 580ºC was found. The stoichiometric point was found by observing the transition from the As-rich 2×4 to the Ga-rich 4×2 surface reconstruction.[62] The re-evaporation rate of As at 580ºC is much higher than at approximately 200ºC, which was found to correspond to ~10% higher As incorporation, allowing a low temperature stoichiometric point to be calculated. Relative adjustments were then made by varying the beam equivalent pressure (BEP). Before moving into the MBE growth chamber, the GaAs substrate is first warmed up to 400ºC in the buffer chamber to remove the water vapor adsorbed on the surface. Then, under the As flux, the oxidized surface of substrate is removed at about 580ºC in the growth chamber. After that, a 100-nm thick high-temperature (HT) GaAs buffer layer is deposited before cooling down to the T_g of (Ga,Mn)As. According to experience, the best T_C is obtained by growing a sample close to the 3D RHEED and 2D RHEED phase boundary which occurs at $T_g \approx 200$ to 250ºC depending on the Mn doping level. In order to let the films reach thermal equilibrium at this lower temperature, a 50 nm thick low-temperature (LT) GaAs layer was grown before starting the (Ga,Mn)As growth. Finally, a high quality (Ga,Mn)As layer can be grown with the thickness from few nanometers to few hundred nanometers. The percentage of Mn is determined by the Mn/Ga flux ratio, which has been calibrated by the mass spectrometry method.

More details of the MBE growth technique can be found in the ref. [59,60,63,64]. All the wafers which have been studied in this thesis were grown by Dr. R. Campion from the MBE group of University of Nottingham.

1.7 Thesis

This thesis consists of three main parts and four appendices. The first part (Chapter 1) is a literature review of my research area of ferromagnetic material and semiconductor material. It also includes some introduction and basic theory background of the DMS system, which are important and will be used in the next few chapters. The second part (Chapters 2, 3 and 4) discusses the three parts of experimental my work and the results of PhD study. Chapter 2 talks about the work of achieving the world record T_C of (Ga,Mn)As samples with nominal Mn percentages above 10%. The work contains the improvement of the MBE growth technique and the post-growth annealing. Chapter 3 is based on the magnetotransport measurement of hydrogen doped (Ga,Mn)As samples. It has relatively high Curie temperature with quite low carrier density, which exceeds the theory (Zener kinetic-exchange model) prediction. Chapter 4 introduces a bi-layer system (Ga,Mn)As with (Al,Ga,Mn)As/(Ga,Mn)(As,P), which has different magnetic anisotropy easy axis for each layer and could be useful in the research of tunnelling magnetoresistance (TMR), tunnelling anisotropic magnetoresistance (TAMR) and spin transfer torque(STT). It also presents the magnetometry study of (Ga,Mn)(As,P) based heterostructures. Part 3(Chapter 5) is the conclusion and future work, which suggests some interesting future work on gate structures and (Ga,Mn)Sb samples.

Appendix A discusses part of my early research work on (Ga,Mn)(As,P) samples. Appendix B contains some basic information of the instruments which have been used for materials characterization: The Quantum design Magnetic Property Measurement System (MPMS) Superconducting Quantum Interference Device (SQUID), the Oxford Instruments “Variox” ^{4}He cryostat system with up to 0.6T external magnet, the Cryogenic ^{4}He magneto-cryostat system with up to 16T superconducting magnet and the Philips X’Pert Materials Research Diffractometer (MRD) system for x-ray reflectivity (XRR). Appendix C presents the Magnetization Units used in this thesis.

References

[1] M. N. Baibich, J. M. Broto, A. Fert, F. Nguyen Van Dau, F. Petroff, P. Etienne, G. Creuzet, A. Friederich, and J. Chazelas, Phys. Rev. Lett. **61**, 2472 (1988).

[2] G. Binasch, P. Grünberg, F. Saurenbach, and W. Zinn, Phys. Rev. B. **39**, 4828 (1989).

[3] S. A. Wolf, D. D. Awschalom, R. A. Buhrman, J. M. Daughton, S. von Molnár, M. L. Roukes, A. Y. Chtchelkanova, and D. M. Treger, Science **294** (5546), 1488 (2001).

[4] G. A. Prinz, Science **282**, 1660 (1998).

[5] D. D. Awschalom, M. E. Flatté, and N. Samarth, Scientific American **5**, 53 (2002).

[6] J. K. Furdyna, J. Appl. Phys. **64**, R29 (1988).

[7] J. K. Furdyna and J. Kossut, "Semiconductors and Semimetals" Vol. **25**, Academic Press, New York (1988)

[8] H. Ohno, H. Munekata, T. Penney, S. von Molnár, L. L. Chang, Phys. Rev. Lett. **68**, 2664 (1992).

[9] H. Ohno, A. Shen, F. Matsukura, A. Oiwa, A. Endo, S. Katsumoto, and Y. Iye., Appl. Phys. Lett. **69**, 363 (1996)

[10] C. Zener, Phys. Rev. **81**, 440 (1950).

[11] C. Zener, Phys. Rev. **83**, 299 (1951).

[12] T. Dietl, H. Ohno, F. Matsukura, J. Cibert, D. Ferrand, Science **287**, 1019 (2000).

[13] T. Dietl, H. Ohno, and F. Matsukura, Phys. Rev. B **63**, 195205 (2001).

[14] T. Jungwirth, K. Y. Wang, J. Mašek, K. W. Edmonds, J. König, J. Sinova, M. Polini, N. A. Goncharuk, A. H. MacDonald, M. Sawicki, A. W. Rushforth, R. P. Campion, L. X. Zhao, C. T. Foxon, and B. L. Gallagher, Phys. Rev. B **72**, 165204 (2005).

[15] J. Mašek and F. Máca, Phys. Rev. B **69** 165212 (2004).

[16] K. W. Edmonds, P. Boguslawski, K. Y. Wang, R. P. Campion, S. V. Novikov, N. R. S. Farley, B. L. Gallagher, C. T. Foxon, M. Sawicki, T. Dietl, M. B. Nardelli, and J. Bernholc, Phys. Rev. Lett. **92**, 037201 (2004).

[17] T. Hayashi, Y. Hashimoto, S. Katsumoto, and Y. Iye, Appl. Phys. Lett. **78**, 1691 (2001).

[18] S. J. Potashnik, K. C. Ku, S. H. Chun, J. J. Berry, N. Samarth, and P. Schiffer, Appl. Phys. Lett. **79**, 1495 (2001).

[19] B. Grandidier, P. Condette, B. Grandidier, J. P. Nys, G. Allan, D. Stiévenard, Ph. Ebert, H. Shimizu, and M. Tanaka, Appl. Phys. Lett. **77**, 4001 (2000).

[20] M. Wang, R. P. Campion, A. W. Rushforth, K. W. Edmonds, C. T. Foxon, and B. L. Gallagher, Appl. Phys. Lett. **93**, 132103 (2008).

[21] V. Novák, K. Olejník, J. Wunderlich, M. Cukr, K. Vyborny, A. W. Rushforth, K. W. Edmonds, R. P. Campion, B. L. Gallagher, J. Sinova, and T. Jungwirth, Phys. Rev. Lett. **101**, 077201 (2008).

[22] B. D. Cullity and C. D.Graham, "Introduction to Magnetic Materials (Second edition)", IEEE press, John Wiley & Sons (2009).

[23] J. Zemen, J. Kučera, K. Olejník, and T. Jungwirth, Phys. Rev. B **80**, 155203 (2009).

[24] T. Hayashi, Y. Hashimoto, S. Katsumoto, A. Endo, M. Kawamura, M. Zalalutdinov and Y. Iye, Physica B **284**, 1175 (2000).

[25] D. Hrabovsky, E. Vanelle, A. R. Fert, D. S. Yee, J. P. Redoules, J. Sadowski, J. Kanski, and L. Ilver, Appl. Phys. Lett. **81**, 2806 (2002)

[26] H. X. Tang, R. K. Kawakami, D. D. Awschalom, and M. L. Roukes, Phys. Rev. Lett. **90**, 107201 (2003)

[27] U. Welp, V. K. Vlasko-Vlasov, X. Liu, J. K. Furdyna, and T. Wojtowicz, Phys. Rev. Lett. **90**, 167206

[28] A. Aharoni, "Introduction to the Theory of Ferromagnetism", Oxford University Press (2000).

[29] K. Y. Wang, K. W. Edmonds, R. P. Campion, L. X. Zhao, C. T. Foxon, and B. L. Gallagher, Phys. Rev. B **72**, 085201 (2005).

[30] D. V. Baxter, D. Ruzmetov, and J.a Scherschligt , Y. Sasaki, X. Liu, J. K. Furdyna, and C. H. Mielke, Phys. Rev. B **65**, 212407 (2002).

[31] E. L. Nagaev, Phys. Rev. B **58**, 816 (1998).

[32] F. Matsukura, M. Sawicki, T. Dietl, D. Chiba, H. Ohno Physica E (Amsterdam) **21**, 1032(2004).

[33] D. Neumaier, K. Wagner, S. Geißler, U. Wurstbauer, J. Sadowski, W. Wegscheider, and D. Weiss, Phys. Rev. Lett. **99,** 116803 (2007)

[34] R. I. Potter, Phys. Rev. B **10**, 4626 (1974).

[35] T. Jungwirth, J. Sinova, K. Y. Wang, K.W. Edmonds R. P. Campion B. L. Gallagher C. T. Foxon Q. Niu, and A. H. MacDonald, Appl. Phys. Lett. **83**, 320 (2003).

[36] W. Doring, Ann. Phys. (Leipzig) **424**, 259 (1938).

[37] A. W. Rushforth, K. Výborný, C. S. King, K. W. Edmonds, R. P. Campion, C. T. Foxon, J. Wunderlich, A. C. Irvine, P. Vašek, V. Novák, K. Olejník, J. Sinova, T. Jungwirth, and B. L. Gallagher, Phys. Rev. Lett. **99**, 147207 (2007).

[38] E. H. Hall, American Journal of Mathematics **2**, 287 (1879).

[39] E. H. Hall, Philos. Mag. **12**, 157 (1881).

[40] J. Smit, Physica (Amsterdam) **21**, 877 (1955).

[41] L. Berger, Phys. Rev. B **2**, 4559 (1970).

[42] T. Jungwirth, Q. Niu, and A. H. MacDonald, Phys. Rev. Lett. **88**, 207208 (2002).

[43] S. Shen, X. Liu, Z. Ge, J. K. Furdyna, M. Dobrowolska, and J. Jaroszynski, J. Appl. Phys. **103**, 07D134 (2008).

[44] M. Glunk, J. Daeubler, W. Schoch, R. Sauer, and W. Limmer, Phys. Rev. B **80**, 125204 (2009).

[45] T. Fukumura, H. Toyosaki, K. Ueno, M. Nakano, T. Yamasaki, and M. Kawasaki, Jpn. J. Appl. Phys. **46**, pp. L642-L644 (2007).

[46] D. Ruzmetov, J. Scherschligt, D. V. Baxter, T. Wojtowicz, X. Liu, Y. Sasaki, J. K. Furdyna, K. M. Yu, and W. Walukiewicz, Phys. Rev. B **69**, 155207 (2004).

[47] J. J. Binney , N. J. Dowrick, A. J. Fisher, and M. E. J. Newman, “The Theory of Critical Phenomena: An Introduction to the Renormalization Group”, Clarendon Press, Oxford (reprinted 1999).

[48] K. Y. Wang, M. Sawicki, K. W. Edmonds, R. P. Campion, S. Maat, C. T. Foxon, B. L. Gallagher, and T. Dietl, Phys. Rev. Lett. 95, 217204 (2005)

[49] A. Arrott, Phys. Rev. **108**, 1394 (1957).

[50] K. P. Belov, “Magnetic Transitions”, Boston Technical, Boston (1965).

[51] Daniel I. Khomskii, “Basic Aspects of the Quantum Theory of Solids: Order and Elementary Excitations”, Cambridge University Press (2010).

[52] A. Arrott and J. E. Noakes, Phys. Rev. Lett. 19, 786 (1967).

[53] S. J. Potashnik, K. C. Ku, S. H. Chun, J. J. Berry, N. Samarth, and P. Schiffer, Appl. Phys. Lett. **79,** 1495 (2001).

[54] A. H. Macdonald, P. Schiffer and N. Samarth, Nature Materials 4, 195 (2005).

[55] P. G. de Gennes and J. Friedel, J. Phys. Chem. Solids **4**, 71 (1958).

[56] C. Haas, Crit. Rev. Solid State Sci. **1**, 47 (1970).

[57] L. Chen, X. Yang, F. Yang, J. H. Zhao, J. Misuraca, P. Xiong, and S. von Molnár, Nano Lett. **11**, 2584 (2011).

[58] M. E. Fisher and J. S. Langer, Phys. Rev. Lett. **20**, 665 (1968).

[59] A. Y. Cho and J. R. Arthur, “Molecular beam epitaxy”, Prog. Solid State Chem. **10**, 157 (1975).

[60] B. A. Joyce, D. D. Vvedensky, C. T. Foxon, “Growth mechanisms in MBE and CBE of III–V compounds”, in: T. S. Moss (Ed.), Handbook on Semiconductors, North-Holland, Amsterdam, Vol. **3**, ch. 1 & 4 (1994).

[61] J.J. Harris, B.A. Joyce and P.J. Dobson, Surf. Sci. Lett. **103**, L90 (1981).

[62] A. Y. Cho, J. Appl. Phys **42**, 2074 (1971).

[63] R. P. Campion, K. W. Edmonds, L. X. Zhao, K. Y. Wang, C. T. Foxon, B. L. Gallagher, and C. R. Staddon, J. Crystal Growth **247**, 42 (2003).

[64] R. P. Campion, K. W. Edmonds, L. X. Zhao, K. Y. Wang, C. T. Foxon, B. L. Gallagher, and C. R. Staddon, J. Crystal Growth **251**, 311 (2003).

Chapter 2

Achieving high Curie Temperatures in (Ga,Mn)As

This chapter describes a detailed study of the effect on T_C of the growth condition and post-growth annealing procedures for epitaxially grown ($Ga_{1-x}Mn_x$)As layers with x_{total} (the sum of the number of substitutional and interstitial Mn) up to 12% and T_C up to 185 K. The highest T_C values are obtained for growth temperatures very close to the two-dimensional (2D) – three-dimensional (3D) growth phase boundary. The increase in T_C, due to the removal of interstitial Mn by post-growth annealing, is counteracted by a second process, which reduces T_C and which is more effective at higher annealing temperatures. These results show that it is necessary to optimize the growth parameters and post-growth annealing procedure to obtain the highest T_C.

Statement: the MBE growth of material was carried by Dr. Richard Campion. I carried out all the annealing studies, post-growth processing of materials, magnetic measurements and extraction of T_C. The high T_C was ultimately achieved in an interactive process with my results motivating further MBE materials development.

2.1 Introduction

As mentioned in the first Chapter, (Ga,Mn)As is one of the most widely studied DMS systems exhibiting carrier mediated ferromagnetism. For this material to be useful in device applications, it will be necessary to increase the T_C above room temperature. Theory predicts that T_C is proportional to the saturation magnetization, which depends upon the density of substitutional Mn ions. [1,2] This trend has been confirmed experimentally for samples with substitutional Mn density (x_s) up to 6.8% grown by MBE with T_C reaching 173 K. [2] x_s ~6.8% is achieved for total Mn concentration x_{total} ~9% with the additional about 2.2% incorporated as interstitial Mn, which can be removed by post-growth annealing.[3,4] Many attempts to grow (Ga,Mn)As with larger x_{total} have failed to achieve T_C in excess of the previous record [2] and have produced conflicting results with T_C decreasing, [5] saturating, [6] or increasing [7] with increasing x_{total}. In Ref. 6, it was found that T_C saturated at 165 K for x_{total} ~10%, leading the authors to suggest that the Zener model may not be applicable in the heavily alloyed regime. However, in another study, Olejnik *et al.* [8] reported T_C =180 K for x_{total} =11%, obtained by etching and annealing the sample. These studies used SQUID magnetometry [6,8] or anomalous Hall Effect [5,7] to determine T_C. Both methods are established techniques for determining T_C. The range of different results obtained by different groups for x_{total} >10% indicates that more research is required to understand how growth parameters and post-growth annealing procedures affect the achievable T_C when x_{total} >10%. The next few sections will present the results which show the effects of growth temperature, Ga:As ratio, and post-growth annealing procedure on the Curie temperature (T_C) of (Ga,Mn)As layers grown by LT-MBE system.

2.2 The control of growth parameters to achieve high T_C

A series of 25nm thick $(Ga_{0.88}Mn_{0.12})As$ films have been grown on GaAs(001) substrate under different growth conditions. Figure **2.1** shows the configuration diagram of each layer. Each wafer was cut into samples with dimensions $5mm \times 4mm$ which were then annealed at the temperatures below the growth temperature. As explained in chapter 1, this is an established method [3] for the

removal of interstitial Mn and achieving high T_C. T_C was determined from the measurements of the temperature dependent remnant magnetization in a Quantum Design MPMS SQUID magnetometer. The technical details of the SQUID will be presented in Appendix B. Each sample was cooled in a field of 1000 Oe before measuring remanence as a function of increasing temperature in zero applied magnetic field.

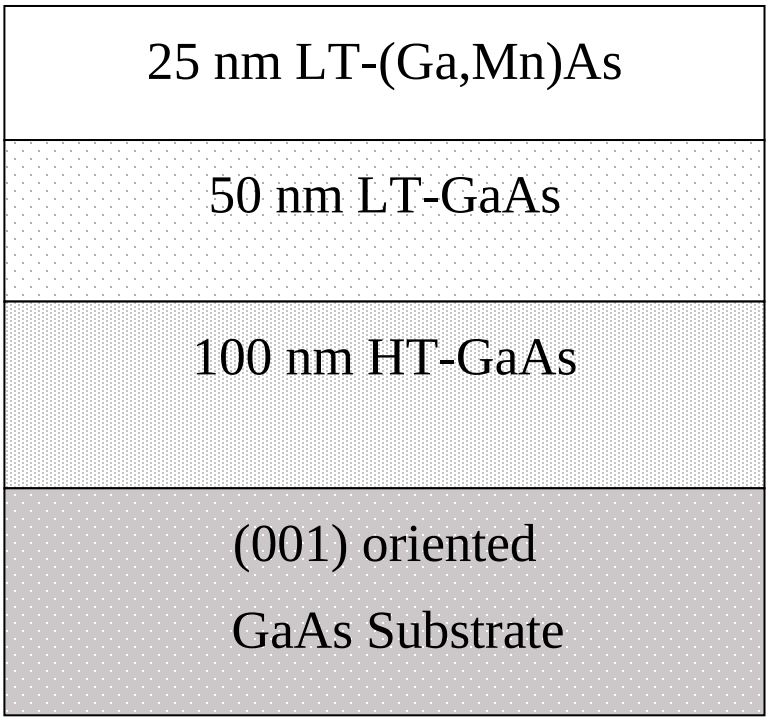

Figure 2.1 *The layer structure of (Ga,Mn)As samples*

2.2.1 The control of As:(Ga+Mn) growth ratio

Excess As or Ga has been shown to lead to the formation of As_{Ga} antisites or 3D growth of GaAs, respectively. [9] The study of As:(Ga+Mn) growth ratio is the first step for achieving high T_C in the heavy doping (Ga,Mn)As materials. Different samples (with wafer No.1-4) were grown with the ratio ranging from 1 to 1.15, and the 18 hours of 190ºC post-growth annealing was applied to all the samples which were taken from the centre of each wafer.

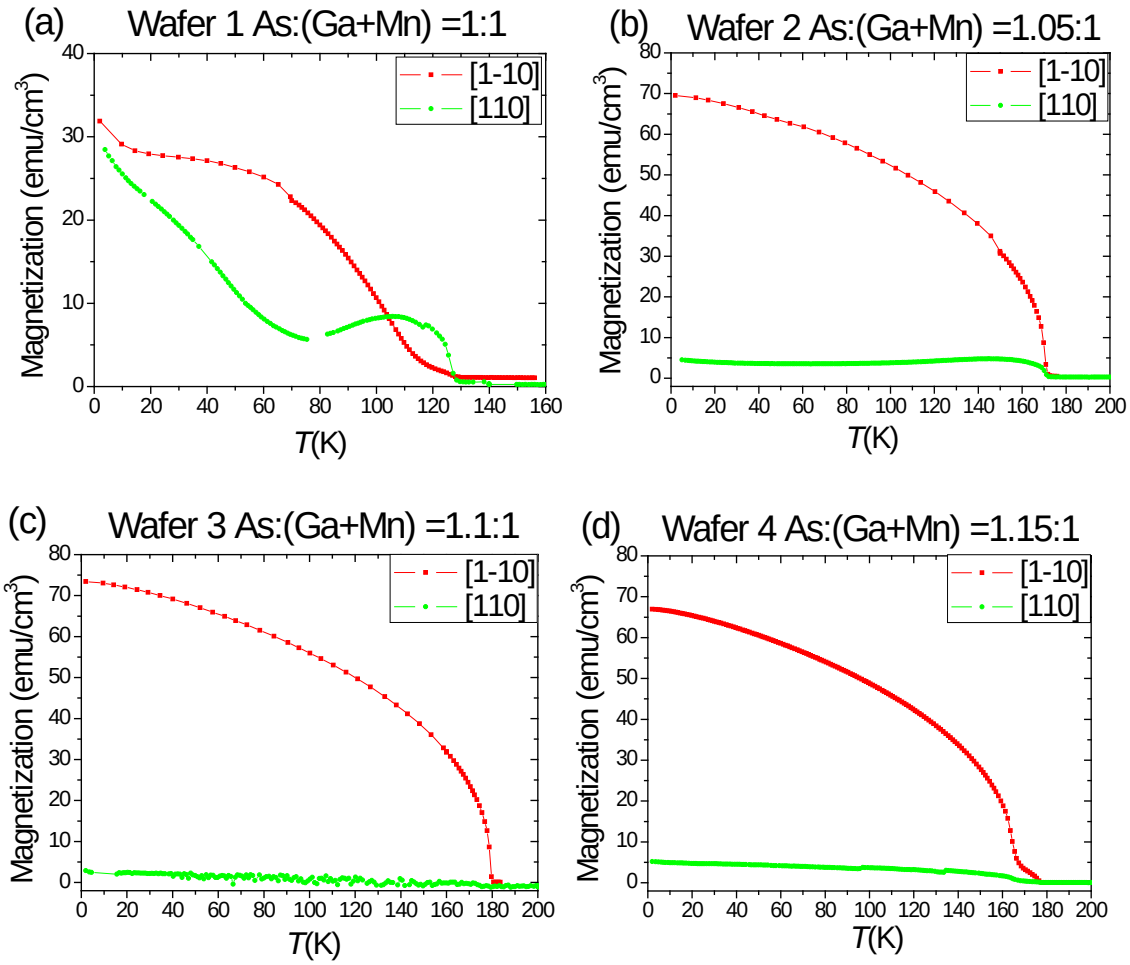

Figure 2.2 *Projection of the temperature dependent remnant magnetization after 1000 Oe field cool for the samples with different As:(Ga+Mn) growth ratio*

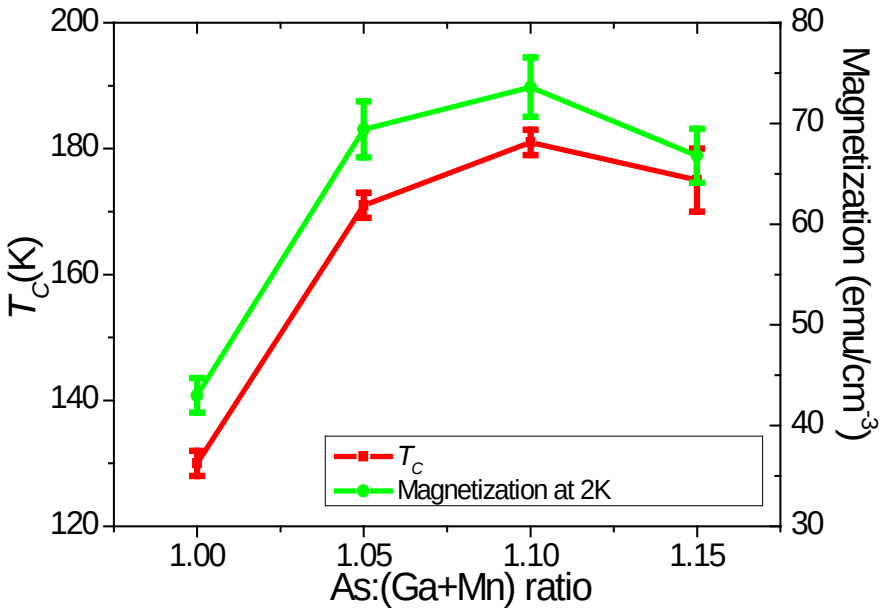

Figure 2.3 *T_C and saturation magnetization of the samples with different As:(Ga+Mn) growth ratio. All the samples were taken from the centre of the wafer and have been annealed for 18h at 190ºC.*

In agreement with previous studies [6,9], the results show not only the T_C but also the magnetization and magnetic anisotropy are highly sensitive to the As:(Ga+Mn) ratio. In compressively strained (Ga,Mn)As films, magnetic domains can be very large, extending over several millimeters [10], and the films tend to stay in a single-domain state during the temperature dependent remnant magnetization measurement. Figure **2.2** shows the projection of the temperature dependent remnant magnetization along [1-10] and [110] directions of the four annealed samples. All the samples show very strong uniaxial magnetic anisotropy along [1-10] direction, except the first one (grown under the ratio of 1:1) shows very different magnetic anisotropy. Besides the different anisotropy easy axis, the reduction of III:V growth ratio from 1.1:1 to 1:1 also leads to a pronounced reduction of the T_C and magnetization. (Figure **2.3**) The highest T_C of 180K comes from the sample with a ratio of 1.1:1, and all the 12% x_{total} samples mentioned in the next section were grown based on this ratio.

2.2.2 The control of growth temperature

The growth temperature is a very important parameter for the MBE growth, and the best results occur when growth temperature is close to the 2D RHEED and 3D RHEED growth phase boundary according to the grower's experience. (Figure **2.4**) The red circle in the figure indicates the best growth temperature, which is around 200ºC-210ºC for 11% and 12% nominal Mn samples.

Three wafers (wafer No.5-7) were grown at different substrate temperatures (T_g) which was measured by a band edge spectrometer (BandiT from K-Space) under reflection geometry. It takes approximately 4.5 minutes to grow 25nm of (Ga,Mn) layer. The first one was grown at a substrate temperature of 205ºC with the centre of the wafer crossing the 2D-3D phase boundary at ~1.25 minutes into the growth. The second was grown at 202ºC, crossing at ~2 minutes and the third was grown at 201ºC, crossing at ~4 minutes. Figure **2.5** shows the change of T_g during the growth of (Ga,Mn)As layer. The quoted growth temperatures are accurate within 1ºC and refer to the temperature at the start of the growth of the (Ga,Mn)As layer. Typically T_g remained constant or increased at $\leq$0.5ºC/min while 2D growth was maintained and then decreased at a similar rate after the 2D-3D phase boundary was crossed, presumably due to a change in surface emissivity. The RHEED pattern measured at

different points across the wafer indicates that the temperature across the wafer during growth decreases by approximately 2ºC from the centre to the edge.

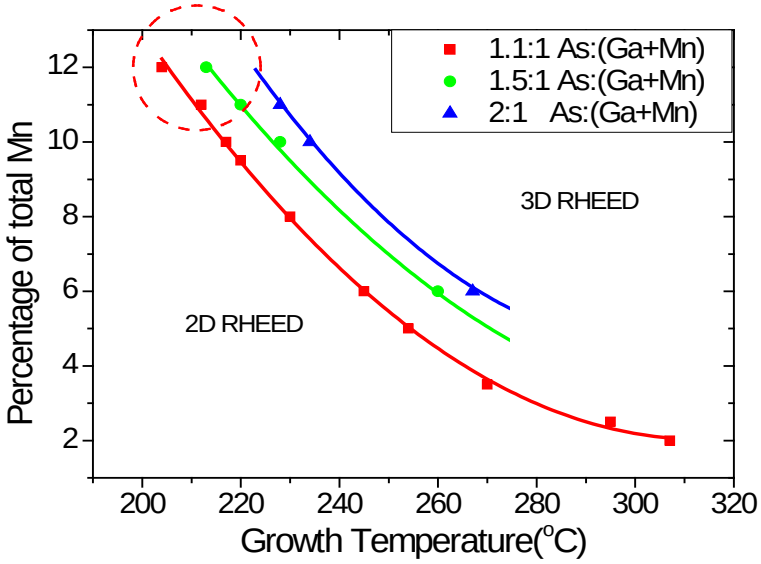

Figure 2.4 *The RHEED growth phase diagram of (Ga,Mn)As, the points are the samples grown by Dr. Richard Campion for adjustment of the phase boundary The lines are drawn to guide the eye.*

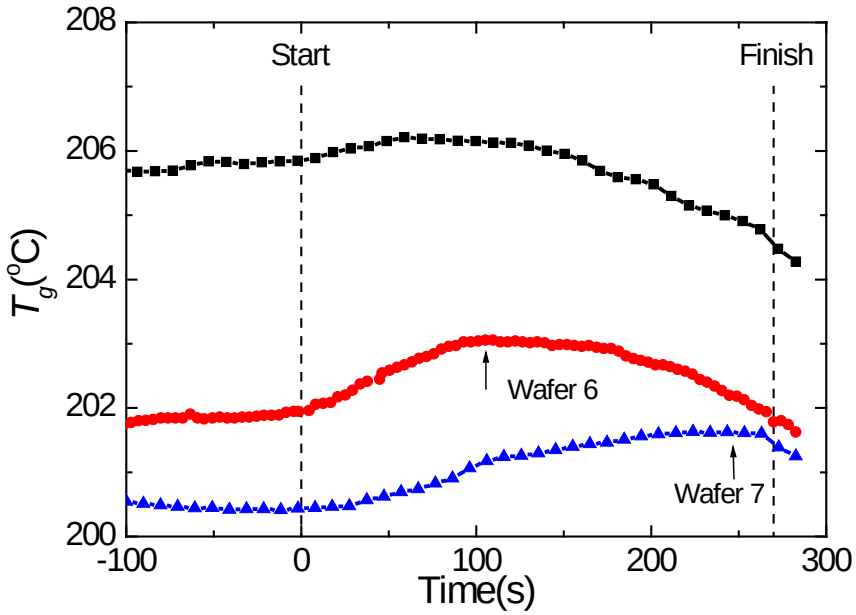

Figure 2.5 *Temperature at the centre of the wafer measured by band edge spectrometry as a function of time during the growth of the (Ga,Mn)As layers. The start and end points of the growth of the (Ga,Mn)As layers are indicated by vertical lines. The arrows indicate the approximate point where the 2D-3D RHEED transition occurs. (The substrate temperature is shown for wafers 6 and 7. For wafer 5 the data was not recorded. Instead data is shown for a wafer grown under similar conditions. For this wafer the initial temperature was 206°C.)*

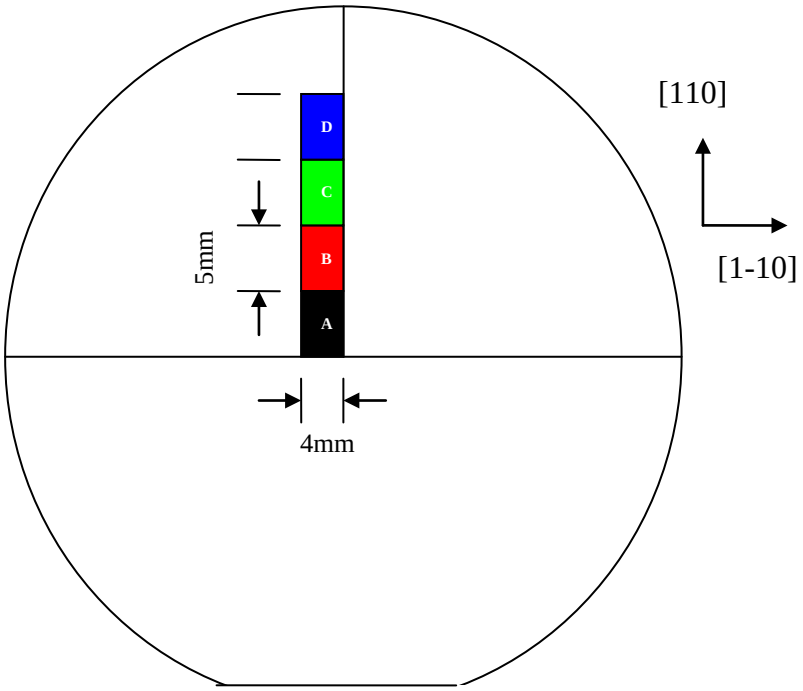

Figure 2.6 *Samples were taken a distance (A) 2.5mm, (B) 7.5mm, (C) 12.5mm and (D) 17.5mm from the centre of the wafer.*

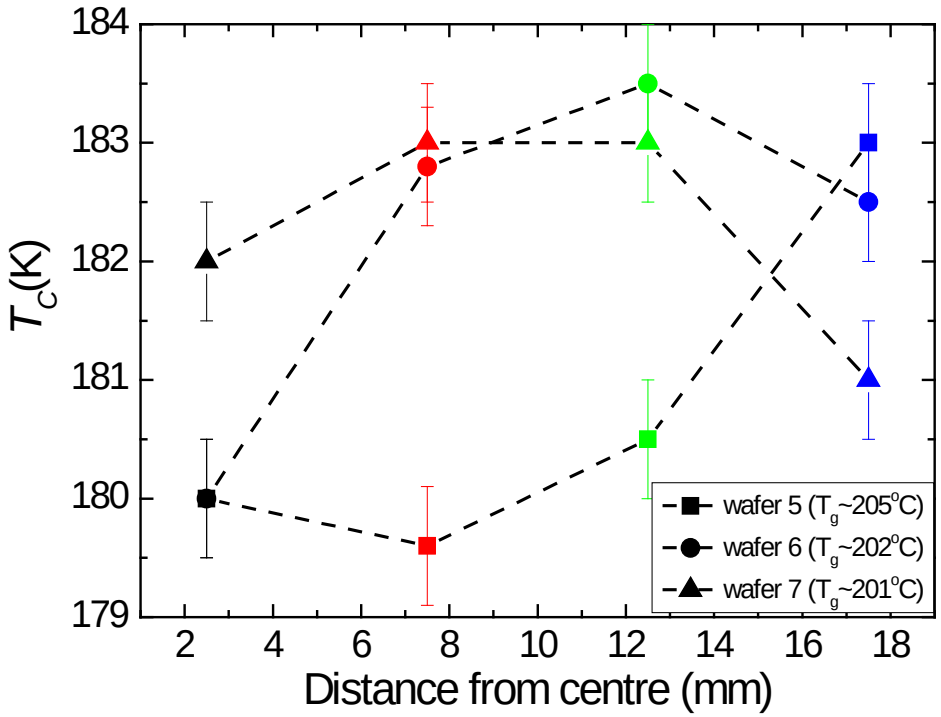

Figure 2.7 *T_C as a function of the distance from the centre of the wafer for wafers 5 (squares) and 6 (circles) annealed at 180ºC for 48 hours and wafer 7 (triangles) annealed at 170ºC for 116 hours. All of them have been fully annealed, which means the further annealing cannot improve the T_C of all the samples.*

Samples were taken from four different distances from the centre of each wafer (Figure **2.6**) and annealed under identical conditions. The distance at which the maximum T_C is obtained moves from the edge of the wafer towards the centre as the growth temperature is decreased. (Figure **2.7**) These results show that the maximum T_C is also highly sensitive to the growth temperature and suggest that the optimum conditions lie very close to the 2D-3D phase boundary which moves closer to the centre of each wafer as the measured substrate temperature is decreased. It is therefore crucial to maintain temperature stability to the accuracy illustrated in Figure **2.5** in order to obtain the highest possible T_C.

2.3 The post-growth annealing to achieve high T_C

Besides the control of growth condition, low temperature post-growth annealing can significantly increase T_C by removing interstitial Mn ions, via diffusion and passivation at the surface, [3] since these are double donors and also couple anti-ferromagnetically with substitutional Mn ions. [11] This is a 1D diffusion function $F = F(\frac{L^2}{Dt})$, where L is the layer thickness, t is the diffusion time (annealing time) and D is the diffusivity of interstitial Mn. [3] Described by Eq. 2-1, D is a function of temperature and characterized by a single activation energy Q=1.4eV. [3] The annealing for 48 hours at 180ºC leads to complete annealing from previous experience, [3] so Eq. 2-2 was used to calculate the full annealing time that would be required for a complete annealing at a different temperature. (Table **2.1**)

$$D(T) \sim e^{-\frac{Q}{kT}} \tag{2-1}$$

$$D(T) \times \mathrm{t} = D(453\mathrm{K}) \times 48 \tag{2-2}$$

Anneal temperature (^{o}C)	160	170	180	190	200	210	220
Anneal time (h)	251	108	48	22.1	10.2	5.2	2.6

Table 2.1 *The anneal time for different annealing temperature*

In this model, the times presented in Table **2.1** should allow T_C to reach a saturation value and further annealing did not significantly increase or decrease T_C.

Furthermore, the resulting T_C should also be the same after different anneal temperatures and times. However, the experimental results show some differences. Figure **2.8** shows the T_C for different annealing temperatures (T_a) varying from 160ºC to 220ºC. It is clear that annealing at higher temperature results in a lower T_C, suggesting that there is a second process, detrimental to ferromagnetism, which is dependent on temperature. The remnant magnetization measured at 2K along [1-10] was assumed to be equal to saturation magnetization, because all these samples show the uniaxial anisotropy easy axis along this direction. In Figure **2.9**, the plot of magnetization did not show a clear trend with annealing temperature. However, one might expect a larger scatter of the points for magnetization than for T_C because the measured moment depends upon the size of the sample (less than 2% error by using the scribe machine) and the alignment (The angle between [1-10] direction and measured direction is within 10º which gives less than 2% error) in the SQUID which could give total ±3% error. Given that the T_C changed by 5% over this range of annealing temperatures, it could be that a similar change in magnetization is obscured by the scatter in the plot below.

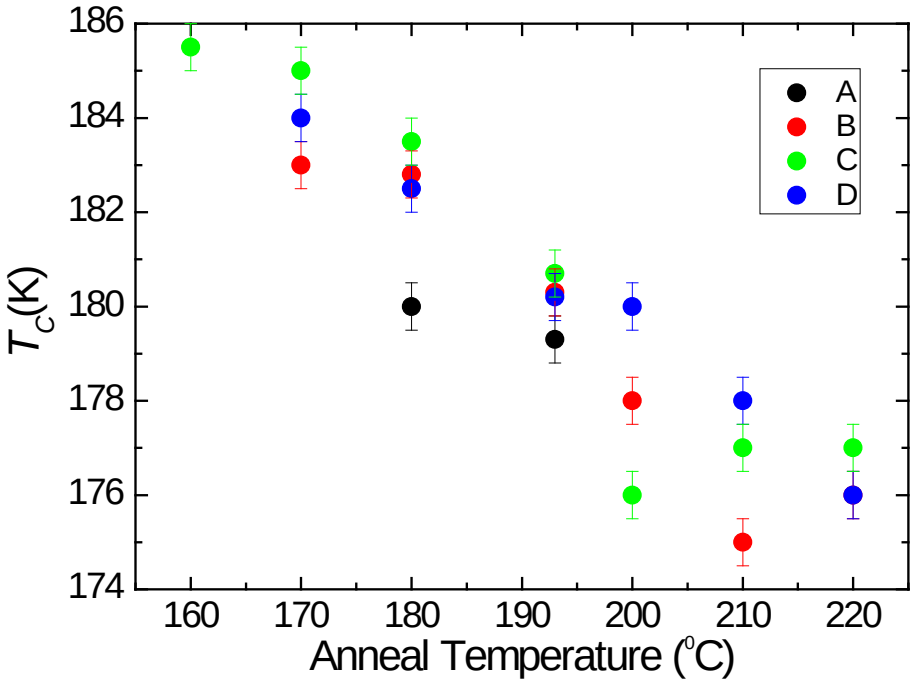

Figure 2.8 *T_C after annealing for 2.6hrs (220ºC), 5.2hrs (210ºC), 13hrs (200ºC), 18hrs (193ºC), 48hrs (180ºC), 110hrs (170ºC) and 280hrs (160ºC) for a series of samples taken from wafer 6*

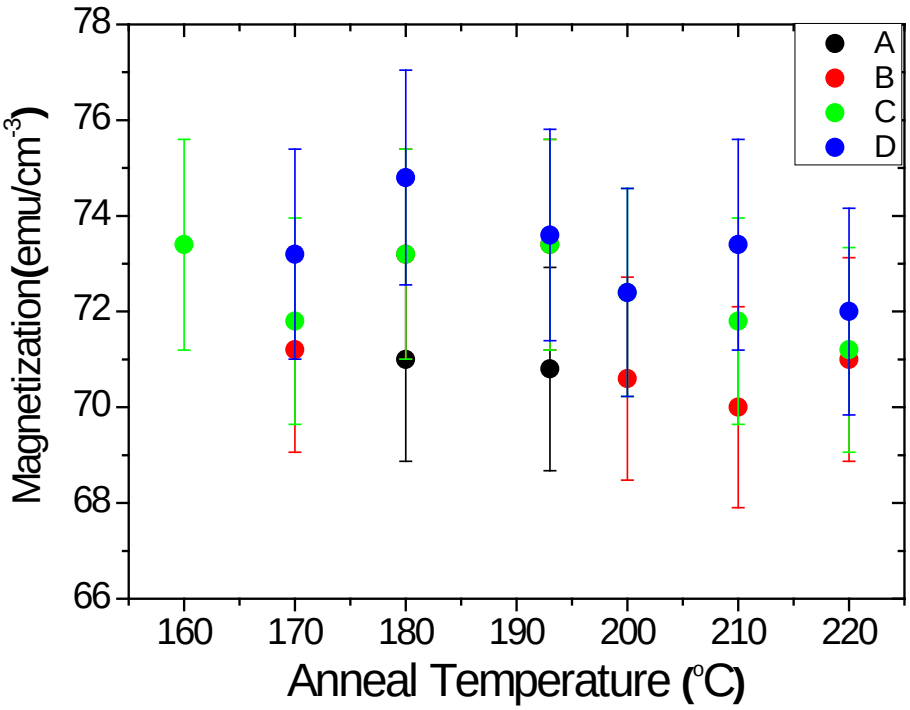

Figure 2.9 *The saturation magnetization for the samples annealed at different temperature.*

One full annealed at 170ºC sample has been put into oven for a few extended annealing steps at 220ºC. As shown in Figure **2.10**, annealing the sample at 220ºC after initially annealing at 170ºC results in a decrease of T_C to a value similar to samples annealed at 220ºC initially. Subsequent annealing at 180ºC does not result in an increase of T_C indicating that the second process is not reversible.

All the behaviors indicate there should be two competing thermally activated processes during the annealing, the first one is the diffusion of interstitial Mn, and the second may be due to the removal of Mn from the electrically active Ga sites, for which the activation energy will be much higher. [12] Other possible mechanisms to explain this phenomenon might involve the loss of substitutional Mn to form MnAs precipitates, or to interstitial sites, also the formation of native defects such as As_{Ga} and Ga_{As} anti-sites which would compensate carriers. Further characterization of the samples will be required to elucidate the mechanism responsible for the decrease T_C at higher annealing temperatures.

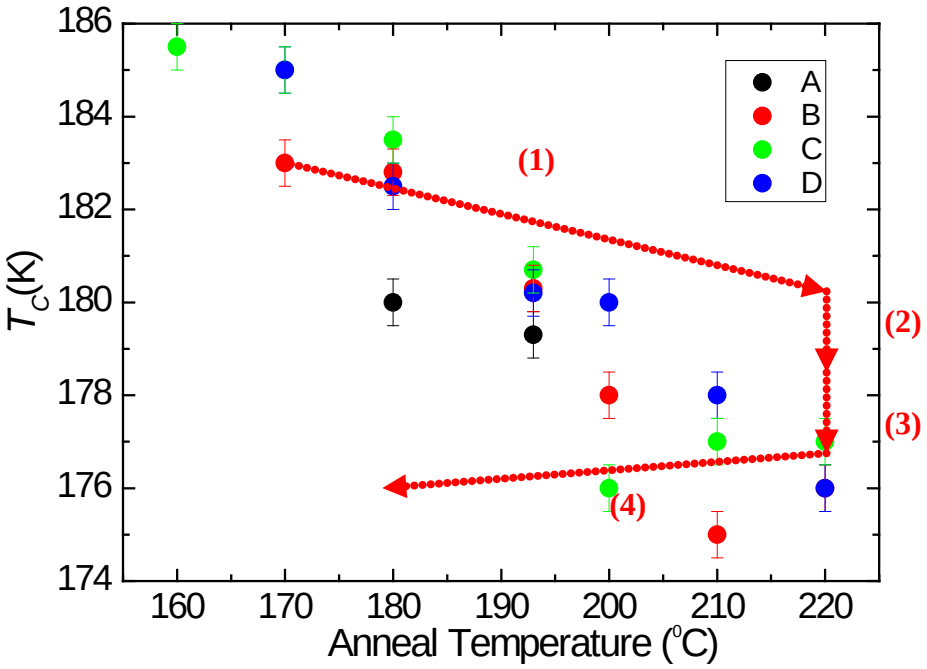

Figure 2.10 *T_C for a sample from series B annealed at 170ºC for 110 hrs then at 220ºC for (1) 1 hour, (2) 2 hour and (3) 2 hour intervals, then (4) at 180ºC for 48 hours.*

2.4 Increasing T_C by chemical etching

Hydrochloric acid (HCl) etching can remove the MnO oxidized surface of the annealed sample which may allow more interstitial Mn ions to diffuse to the surface. [8,13] In that case, the ferromagnetic properties of the high Mn concentration samples can be improved.

First of all, a sample which had been annealed at 170ºC for 110 hours was annealed again for another 28 hours. The T_C does not change significantly after the second annealing (Figure **2.11**), which suggests the diffusion of interstitial Mn becomes saturated.

After that, the sample was etched 30 seconds by 30% diluted HCl and approximately 1nm of the surface has been removed after the process. [8] After rinsing in water (the HCl etched surface is hydrophobic and dries off instantly after the rinsing) the sample was put into the oven for 24 hours additional annealing. Figure **2.12** shows the remanence data along [1-10] direction before and after the process. It is obvious

that the two curves are different; the remnant moment at 2K is reduces about 5% while the T_C increases from 184K to 185K, which is the highest value achieved by Nottingham group.

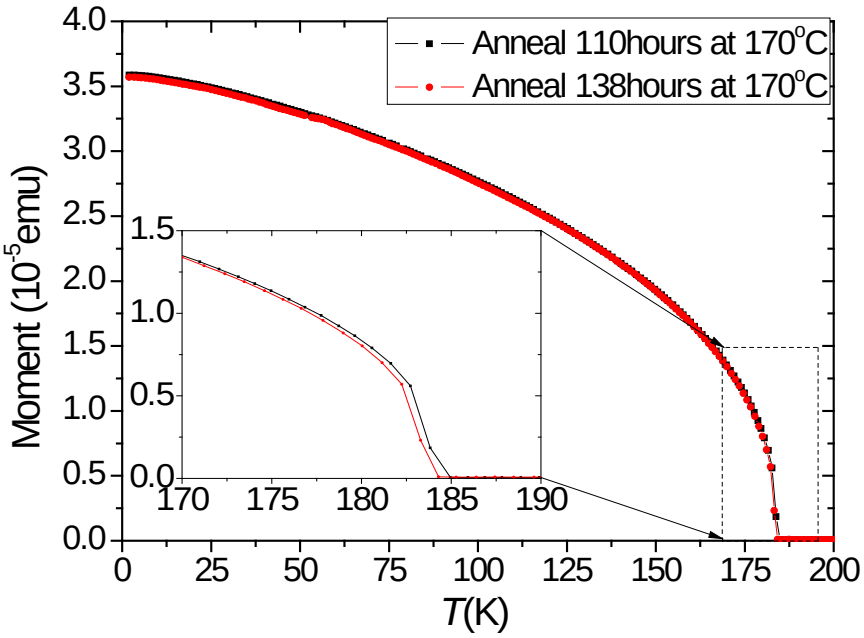

Figure 2.11 *Projection of temperature dependent remnant moment along [1-10] of the sample from wafer 6 which have been annealed at 170ºC for 110 hours and 138 hours, respectively. The inset is the curve around the T_C. The difference is less than 0.5K which is the resolution limit of the measurement.*

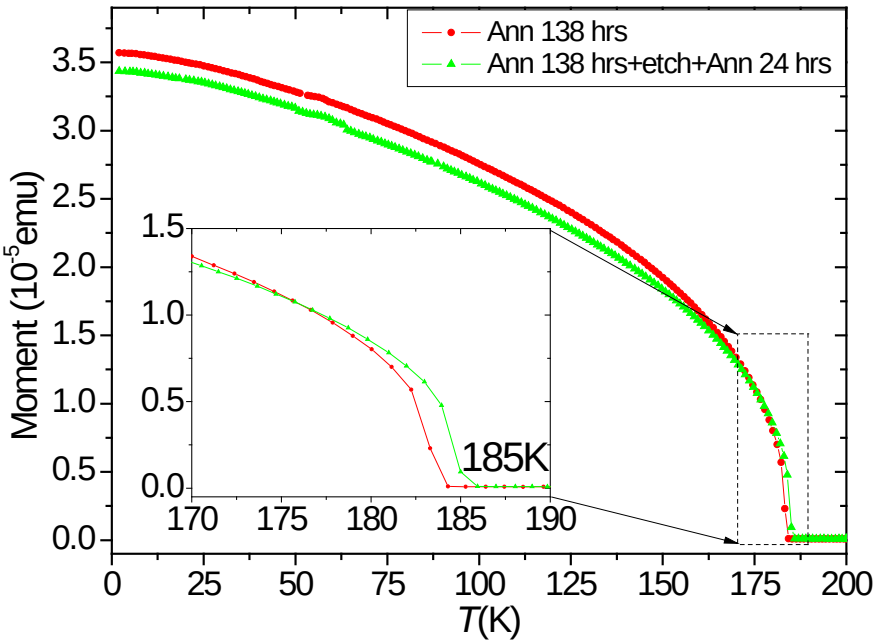

Figure 2.12 *T_C changes after the etching for the sample from wafer 6. Red line: fully annealed sample before etching, Green line: the sample has been etched and annealed again for another 24 hours. The moment reduces 4% at 2K, but the T_C increase about 1.5K after etching.*

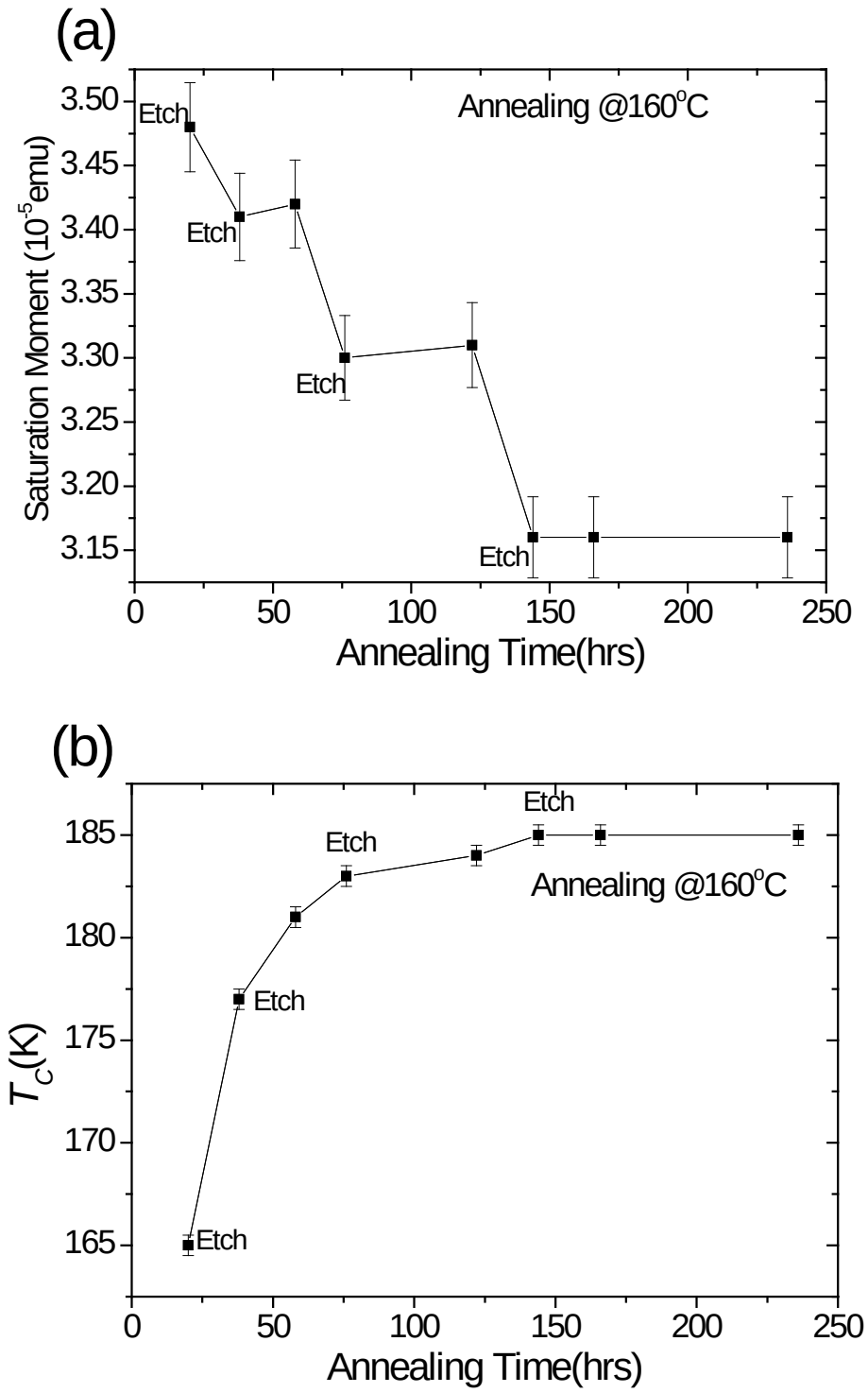

Figure 2.13 *Successive etching with step annealing to achieve high T_C. (a): saturation moment vs. anneal time, (b): Curie temperature versus annealing time*

Another as-grown sample from the same part of the wafer 6 was successively etched and step annealed, and been measured each time after the etching or annealing process. Shown in the Figure **2.13**(a), the saturation moment at 2K reduces about 3%-4% with each etch. Then after few hours annealing at 160ºC, both the moment and the T_C increases. (Figure **2.13**(b)) By four times of etching and about 150 hours annealing, the T_C is saturated at 185K, which is same as the previous etched sample.

Concluded from the two experiments' results, by using the HCl to remove the surface oxide layer which limits the oxidation of interstitial Mn during the annealing process, the T_C of (Ga,Mn)As can be increased.

2.5 Resistance monitored annealing for (Ga,Mn)As samples

2.5.1 Motivation of using resistance monitored annealing method

The conclusion of section 2.3 is the annealing temperature (T_a) has an effect on the resulting T_C. However, because T_a is much higher than the T_C, it is not possible to monitor directly the response of T_C to the post-growth annealing. Monitoring the electrical resistance during annealing can be used to address this problem. As mentioned above, (Ga,Mn)As is a degenerately doped semiconductor with carrier mediated ferromagnetism, for which the mean field Zener model describes the relation between the T_C and carrier density p. We therefore expect T_C to increase monotonically with p, as is observed in ref. 2. The carrier density increases as the interstitial Mn ions diffuse to the surface during the annealing, and it has a relation with longitudinal conductivity σ_{xx} in the form

$$\sigma_{xx} = ep\mu_p \tag{2-3}$$

In this equation, $e \approx 1.602 \times 10^{-19}$ Coulombs is the elementary charge and μ_p is the hole mobility. It has been found that annealing effects μ_p only weakly and so the measured σ_{xx} as a function of annealing gives an indication of how T_C is changing with the annealing. [14,15]

2.5.2 The fabrication of the Hall bars

Standard Hall bars were fabricated on the sample from wafer No.5 by photo-lithography for transport measurements. All the bars were processed on a sample taken from the centre of each wafer in order to make sure that the growth condition of each sample is almost the same. Chemical wet etching method was used to etch down about 1μm of the sample, and evaporated 20nm Ti plus 80nm Au was used for the contacts. (Figure **2.14**) The samples were not annealed significantly during the baking of the photo resist, because the 110ºC baking temperature is much lower than the standard T_a and the length of time is only 2 minutes. Finally, each Hall bar was glued on a 12 pint header and bonded with 17.5μm diameter wires using the wedge bonding machine.

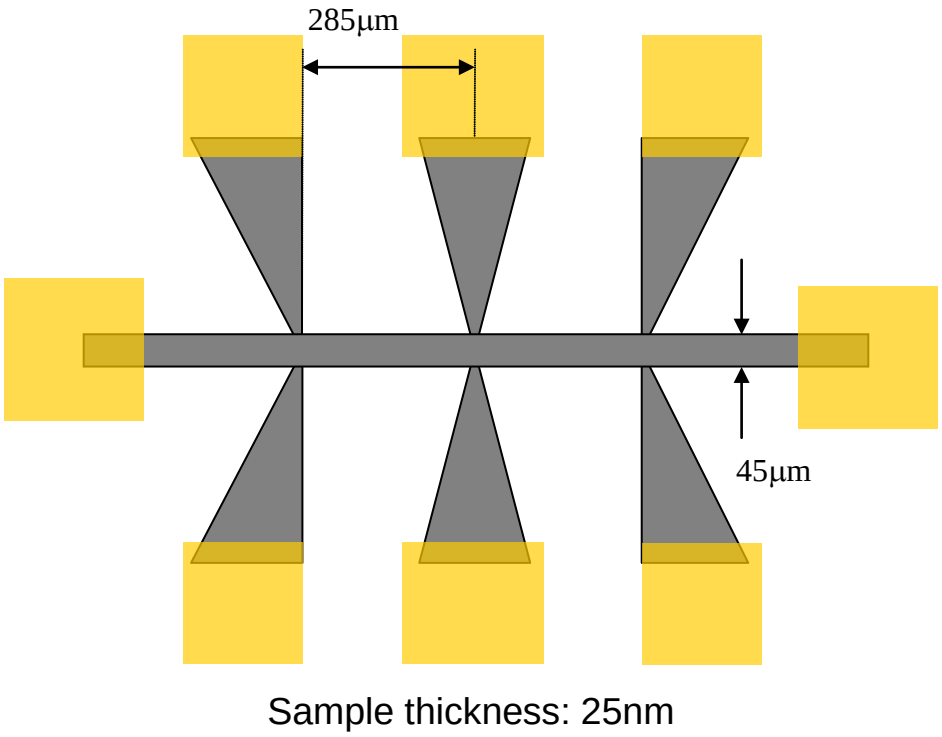

Figure 2.14 *The structure of Hall bar made by photo lithography. Gold colored parts are the Ti/Au contacts.*

2.5.3 The resistance monitored annealing by one step

To start with, an as-grown Hall bar has been put into the oven at 180ºC for a standard annealing. The changes of longitudinal resistance were monitored by the four-terminal method.

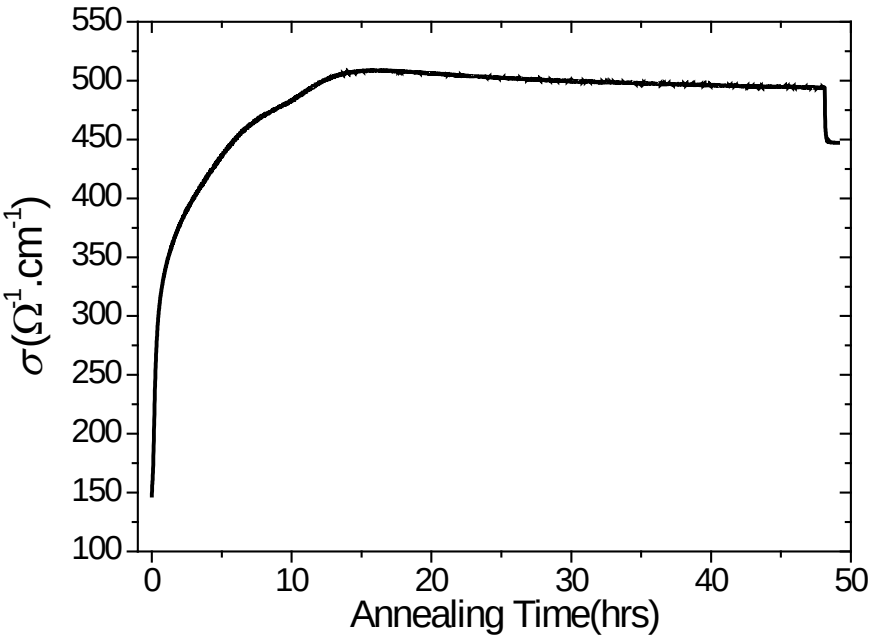

Figure 2.15 *The resistance monitored annealing result for standard 48 hours annealing at 180°C.*

Figure **2.15** shows the relation between conductivity and annealing time. At the beginning of annealing, it took about half hour for the sample to warm up to 180°C (this is proved in the next section on step annealing), and during that time the conductivity increased mainly because the high temperature enhanced the hole mobility μ_p. In the next few hours of annealing, the conductivity kept on increasing sharply because the removal of interstitial Mn donors produced more holes inside the sample, therefore this process can be simulated by the interstitial Mn diffusion model. (Eq. 2-1) [3,12] The conductivity became stable after about 14 hours, which means nearly all the interstitial Mn ions have diffused to the surface of the (Ga,Mn)As layer. After 19 hours, which is earlier than the time required to fully anneal the sample at 180ºC (Table **2.1**), the conductivity started to decrease slowly but continuously. The reason could be the oxidation of the surface reduces the thickness of the (Ga,Mn)As layer, or possibly the second process mentioned in section 2.3 increases some defects after a long time annealing. After 48 hours annealing, the sample was taken out from oven to cool down to room temperature. During that time the conductivity of the sample dropped due to the close relationship between μ_p and the sample temperature.

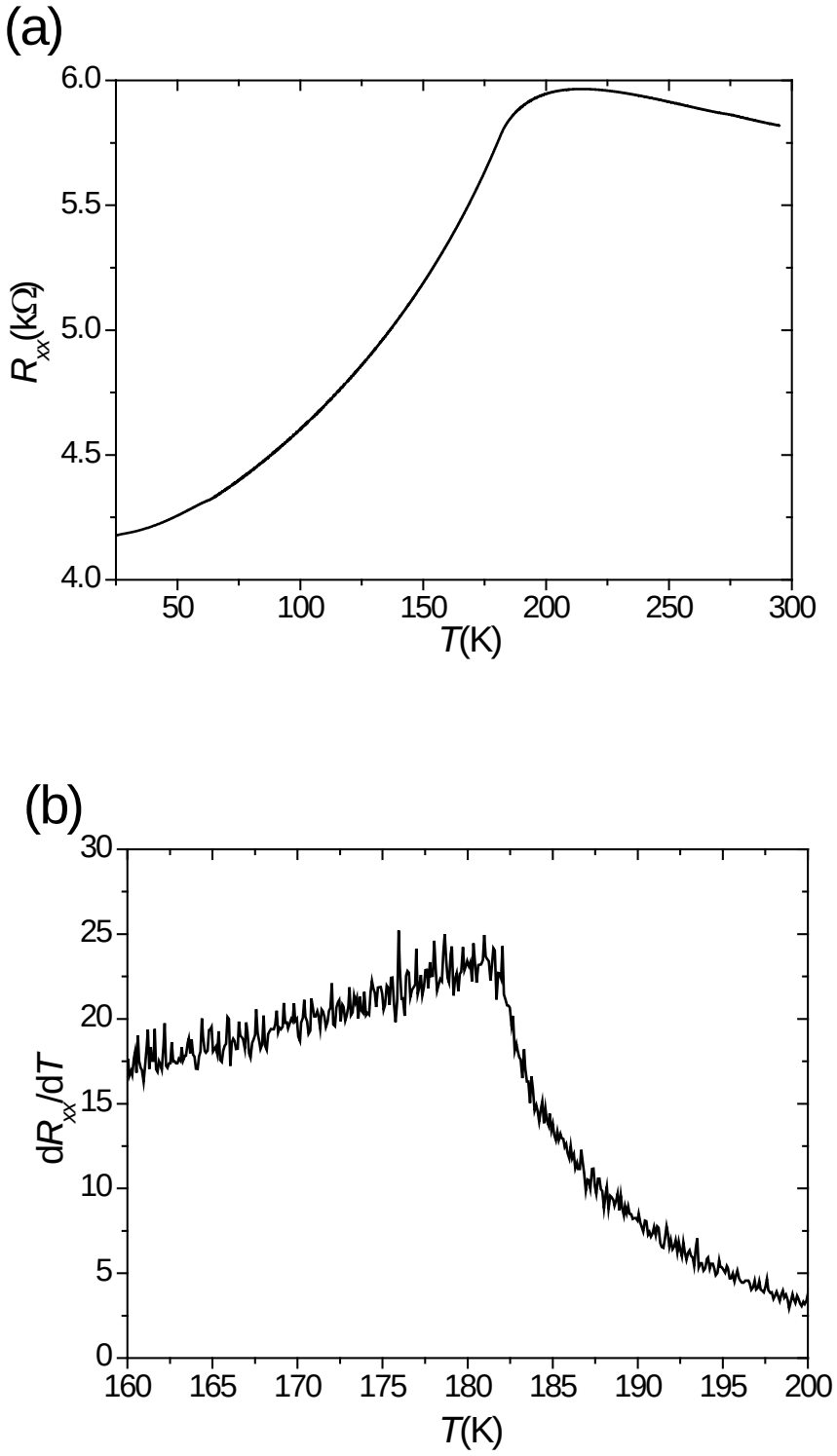

Figure 2.16 *(a) Resistance vs. temperature and (b) the temperature derivatives of resistance. We use the peak point in the graph to determine the* T_C.

The 48 hours annealed sample was put into the Oxford Instruments "Variox" ^{4}He cryostat system to measure the resistance from room temperature to 2K. The T_C was obtained from the peak point of temperature derivatives of resistance (Figure **2.16**(b)). [13] The T_C of the sample is about 182K, which is reasonable close to the SQUID magnetometry result. The difference could be because the piece of the sample which has been processed for the Hall bars and the one used for SQUID measurements are not from the same part of the wafer.

2.5.4 The resistance monitored step annealing

In the second section of the experimental work, the Hall bars were annealed step by step, and between a short time of annealing, the partially annealed samples were taken out from the oven and measured in the cryostat. In that case, the gradual change of the magnetic properties of (Ga,Mn)As can be monitored and the relation between T_C and conductivity can be determined.

Between each annealing step, the T_C was obtained from the peak point of temperature derivatives of resistance (shown in Figure **2.17**(b)). The black curve in Figure **2.18** is the result for the conductivity changes from as-grown to fully annealed at 180ºC. The spike between each annealing step is mainly due to the change of hole mobility during the time (about half hour) when the sample has been warmed up from room temperature to 180ºC. The highest T_C that achieved this time is only 172K, which is much lower than the previous results. One explanation is because the previous sample has been annealed in one step, while this sample has been annealed repeatedly which could introduce some defects. After approximately 50 hours annealing (which includes about 10 hours warming up time), the conductivity started to reduce as found for the previous one step annealing curve. However, the T_C did not change much which suggests the defects caused by the long time annealing reduces the hole mobility rather than the hole density.

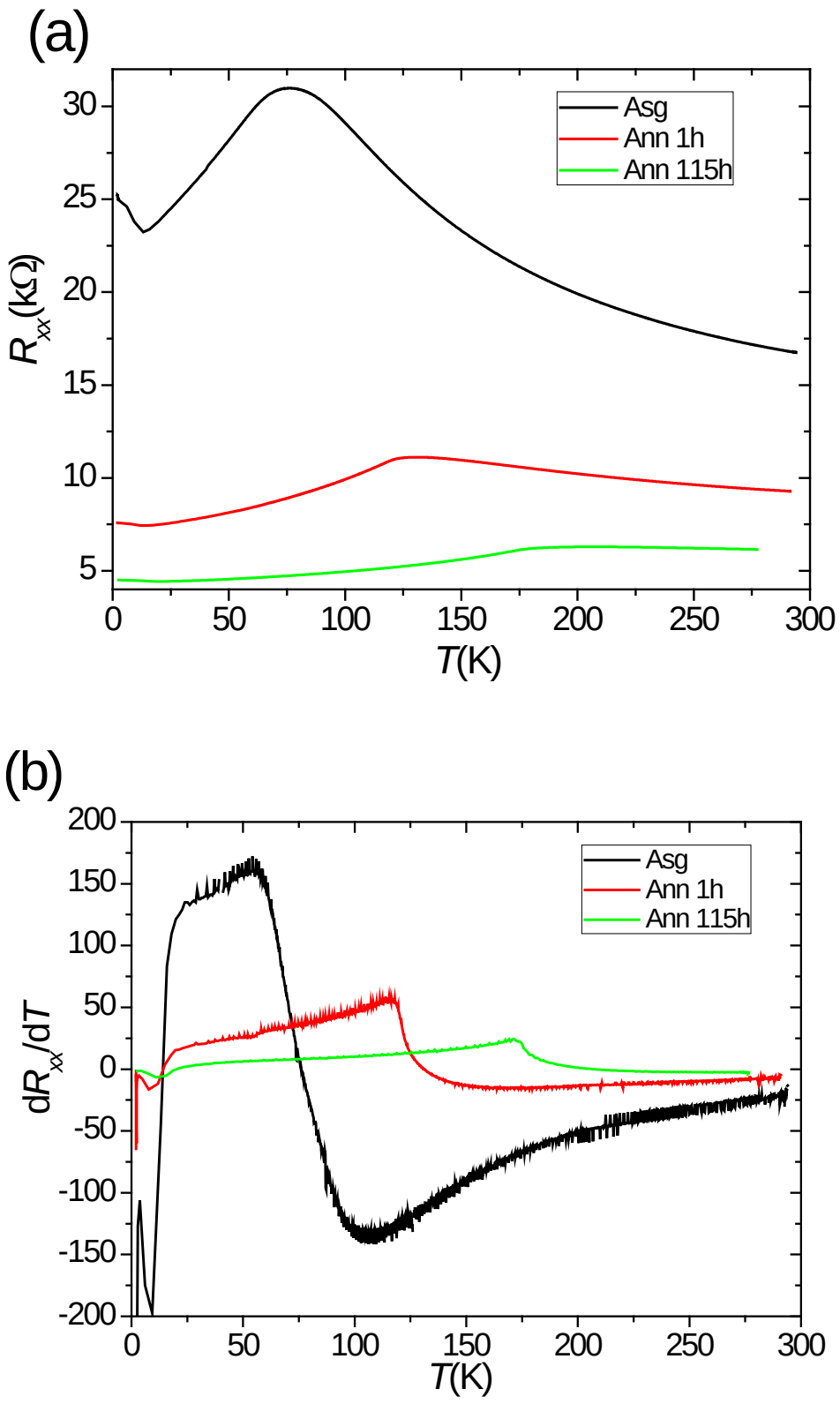

Figure 2.17 *(a) Resistance vs. temperature, (b) the temperature derivative of resistance for the as-grown sample, after 1 hour and 115 hours annealing at 180ºC.*

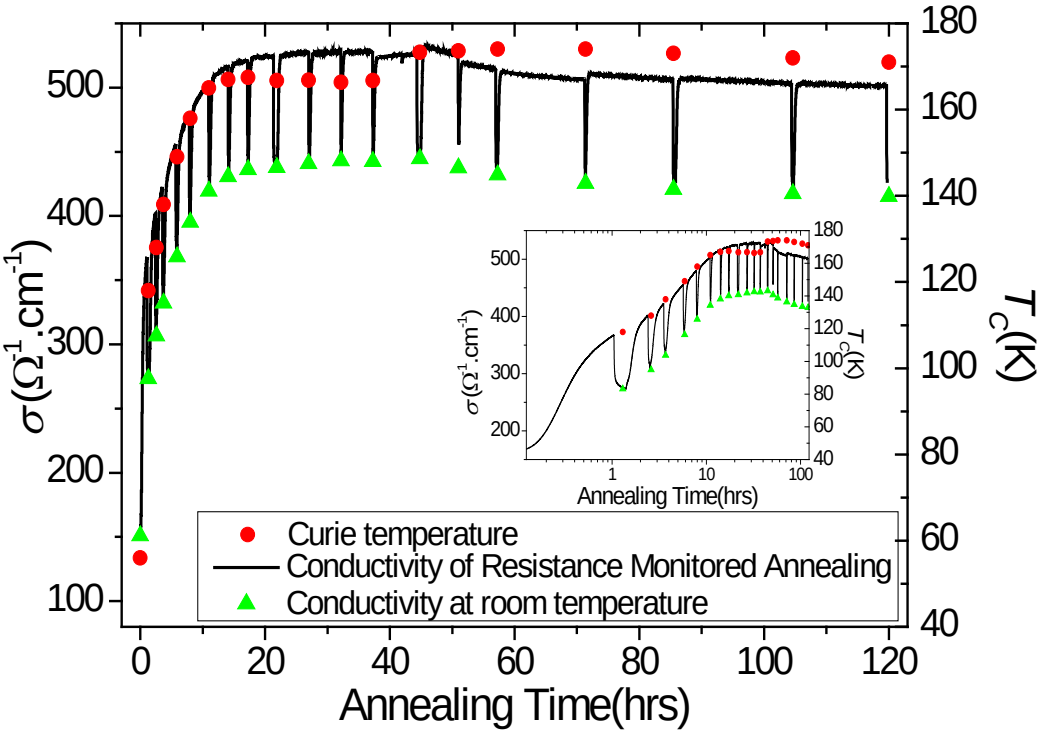

Figure 2.18 *The resistance monitored annealing results at 180ºC for a sample with nominal 12% Mn. The black curve is the conductivity of the sample during the annealing. Each spike on the curve represents one step in which the sample has been taken out from the oven for measurement of the sample's room temperature conductivity and T_C. The green triangle points are the conductivity at 300K, and the red points are the Curie temperatures, which have been obtained from the peak points of temperature derivatives of resistance. Inset: the semi-log plot of annealing time.*

2.5.5 Summary

Besides the samples annealed at 180ºC, another two samples have been fully annealed at two different temperatures 165ºC and 190ºC. Figure **2.19** shows the data of T_C *vs.* room temperature conductivity for samples annealed at 165ºC, 180ºC and 190ºC. It indicates that the resistance monitored step annealing is a good method to show the relation between the magnetic properties and transport properties. The results show that the increase of T_C and conductivity is annealing temperature independent at the beginning of annealing, (Green ellipse) during which the interstitial Mn diffusion is the major process. There is also a second process which can decrease the conductivity, and in this process the relation of T_C and conductivity is annealing temperature dependent. (Red circle) This is consistent with the SQUID results presented in section 2.3.

The results also show that the resistance monitored step annealing method may introduce some unknown defects. For example, something problematic happened after 100 hours (Figure **2.20**) annealing for the sample which has been warmed up to 438K (165ºC) and cooling down to 2K nearly 30 times. The reason could be complicated and may involve not only the sample quality but also the damage of the sample during the fabrication process and annealing schedule.

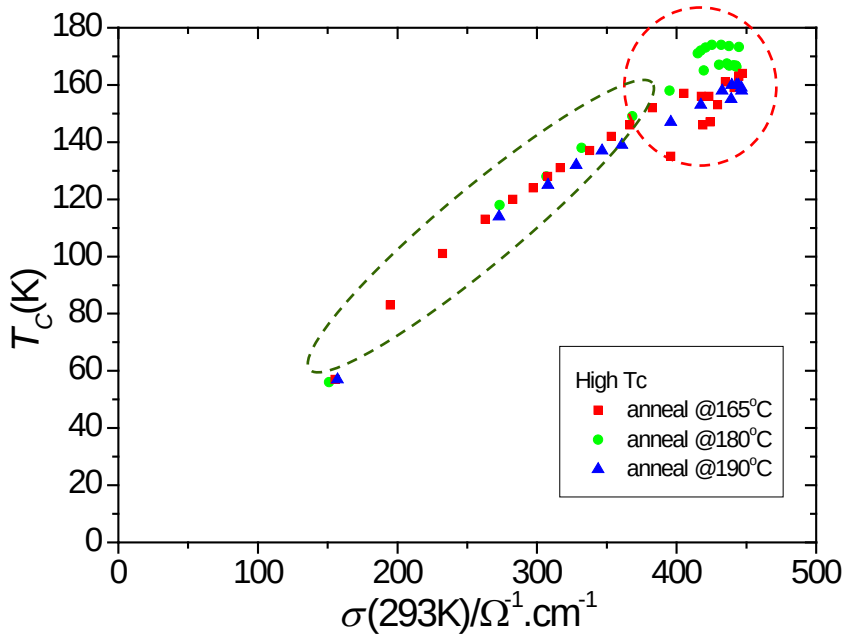

Figure 2.19 *The relation between T_C and room temperature conductivity for samples annealed at different temperatures.*

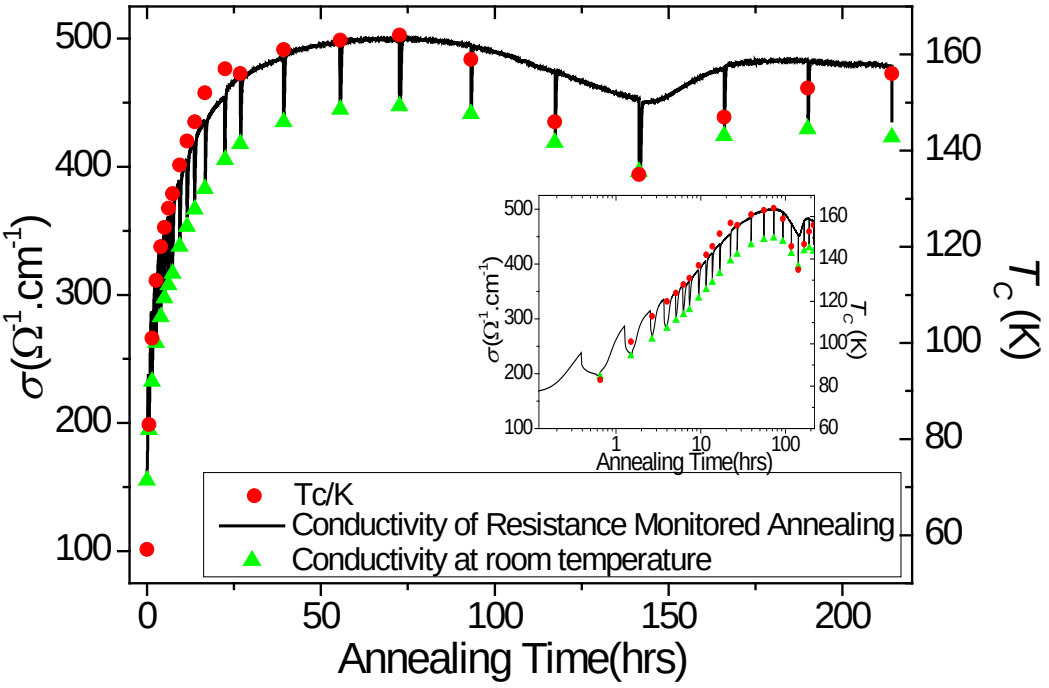

Figure 2.20 *The resistance monitored annealing results of 12% nominal Mn at 165ºC. Inset: the semi-log plot of annealing time.*

2.6 Conclusion of achieving high T_C in (Ga,Mn)As

In addition to the wafers described above, wafers with x_{total} equals to 10% and 11% were grown to obtain the trend of T_C *vs.* saturation magnetization (M_S). The earlier discussion indicated that T_C should increase roughly linearly with x_S but to be more precise T_C should increase roughly linearly with the ferromagnetic Mn magnetization (which can be reduced by moment compensation). Figure **2.21** presents the data of Curie temperature *vs.* saturation magnetization for annealed samples showing the highest T_C for a given x_{total} in this and a previous study of samples grown in Nottingham [6]. For $x_{total} \geq 10\%$ the T_C falls below the previously observed linear trend, which indicated it could become more and more difficult to increase Curie temperature by doping more Mn.

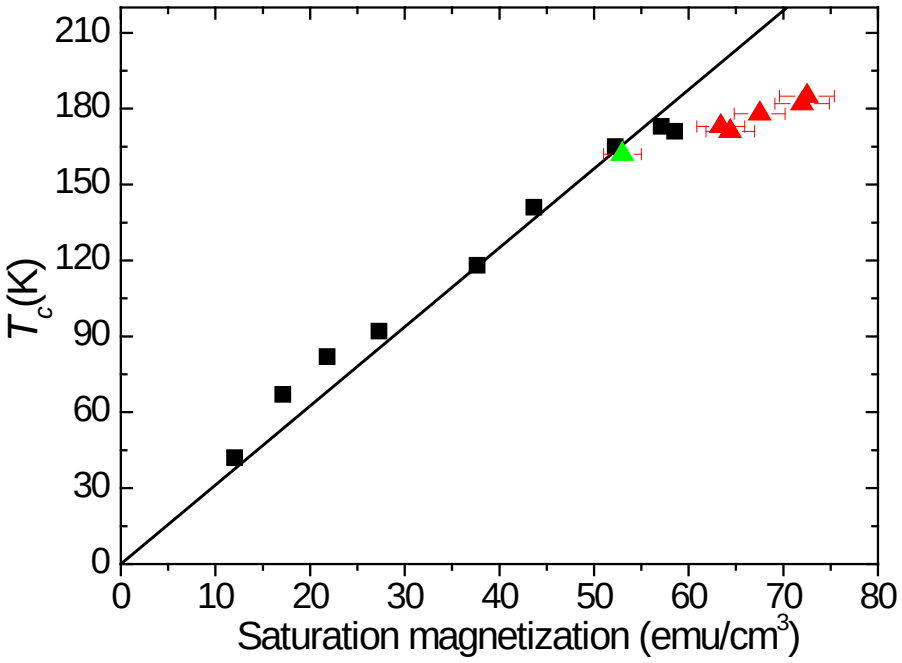

Figure 2.21 *New (red points) T_C vs. saturation magnetization for wafers with x_{total} 10% to 12%. Previous data (black points) comes from ref. 2, 3, 4, the green triangle is the data of H-doped (Ga,Mn)As sample after fully annealed, which will be discuss in next chapter.*

With increasing x_{total}, the growth temperature must be reduced in order to maintain 2D growth, but this increases the probability of forming As_{Ga} antisites and other compensating defects. Hence, precise control over the growth parameters becomes more important for incorporating Mn onto the substitutional sites and for achieving the corresponding increase in T_C. The results show that T_C is sensitive to the growth temperature and As:(Ga+Mn) ratio (extremely sensitive) for MBE grown (Ga,Mn)As layers with x_{total} ≥10%, and also demonstrate that the etching could reduce the annealing time and increase the T_C. Additionally, from the data of SQUID and resistance monitored annealing, the post-growth annealing temperature determines the maximum achievable T_C due to a temperature dependent mechanism in addition to the out diffusion of interstitial Mn. These sensitivities may explain why some previous efforts to improve T_C in material with x_{total} ≥10% have not been successful.

References

[1] T. Dietl, H. Ohno, and F. Matsukura, Phys. Rev. B **63**, 195205 (2001).

[2] T. Jungwirth, K. Y. Wang, J. Mašek, K. W. Edmonds, J. Konig, J. Sinova, M. Polini, N. A. Gonchuruk, A. H. MacDonald, M. Sawicki, A. W. Rushforth, R. P. Campion, L. X. Zhao, C. T. Foxon, and B. L. Gallagher, Phys. Rev. B **72**, 165204 (2005).

[3] K. W. Edmonds, P. Bogusławski, K. Y. Wang, R. P. Campion, S. V. Novikov, N. R. S. Farley, B. L. Gallagher, C. T. Foxon, M. Sawicki, T. Dietl, M. B. Nardelli, and J. Bernholc, Phys. Rev. Lett. **92**, 037201 (2004).

[4] K. W. Edmonds, P. Bogusławski, K. Y. Wang, R. P. Campion, S. V. Novikov, N. R. S. Farley, B. L. Gallagher, C. T. Foxon, M. Sawicki, T. Dietl, M. B. Nardelli, and J. Bernholc, Phys. Rev. Lett. **94**, 139702 (2005).

[5] S. Ohya and M. Tanaki, Appl. Phys. Lett. **90**, 112503 (2007).

[6] S. Mack, R. C. Myers, J. T. Heron, A. C. Gossard, and D. D. Awschalom, Appl. Phys. Lett. **92**, 192502 (2008).

[7] D. Chiba, Y. Nishitani, F. Matsukura, and H. Ohno, Appl. Phys. Lett. **90**, 122503 (2007).

[8] K. Olejník, M. H. S. Owen, V. Novák, J. Mašek, A. C. Irvine, J. Wunderlich, and T. Jungwirth, Phys. Rev. B **78**, 054403 (2008).

[9] C. Myers, B. L. Sheu, A. W. Jackson, A. C. Gossard, P. Schiffer, N. Samarth, and D. D. Awschalom, Phys. Rev. B **74**, 155203 (2006).

[10] U. Welp, V. K. Vlasko-Vlasov, X. Liu, J. K. Furdyna, T. Wojtowicz, Phys. Rev. Lett. **90**, 167206 (2003).

[11] J. Blinowski and P. Kacman, Phys. Rev. B **67**, 121204 (2003).

[12] K. W. Edmonds, K. Y. Wang, R. P. Campion, A. C. Neumann, N. R. S. Farley, B. L. Gallagher, and C. T. Foxon, Appl. Phys. Lett. **81**, 4991 (2002).

[13] V. Novák, K. Olejník, J. Wunderlich, M. Cukr, K. Vyborny, A. W. Rushforth, K. W. Edmonds, R. P. Campion, B. L. Gallagher, J. Sinova, and T. Jungwirth, Phys. Rev. Lett. **101**, 077201 (2008).

[14] K. W. Edmonds, K. Y. Wang, R. P. Campion, A. C. Neumann, C. T. Foxon, B. L. Gallagher, and P. C. Main, Appl. Phys. Lett. **81**, 3010 (2002).

[15] T. Jungwirth, J. Sinova, A. H. MacDonald, B. L. Gallagher, V. Novák, K. W. Edmonds, A. W. Rushforth, R. P. Campion, C. T. Foxon, L. Eaves, E. Olejník, J. Mašek, S.-R. Eric Yang, J. Wunderlich, C. Gould, L. W. Molenkamp, T. Dietl, and H. Ohno, Phys. Rev. B **76**, 125206 (2007).

Chapter 3

Carrier density of hydrogen doping (Ga,Mn)As sample

This Chapter discusses the possibility of producing low carrier density high saturation magnetization ferromagnetic semiconductor (Ga,Mn)As (with nominal Mn 12%) by introducing interstitial hydrogen donor during the MBE growth.

From detailed temperature-dependent measurements of the Hall resistance and magnetic susceptibility, it is found that the anomalous Hall resistance is the dominant contribution even at room temperature, which indicates that the carrier density obtained directly from the linear Hall slope is incorrect. On the other hand, the systematic fitting procedures of low temperature high magnetic field Hall effect data on step-annealed samples with a wide range of conductivity can yield reasonably values of carrier density. The results show that these as-grown and lightly annealed H-doped samples have relatively high Curie temperatures down to low carrier density which make them good candidates for showing strong gate control of ferromagnetism.

3.1 Introduction of hydrogen doped (Ga,Mn)As samples

Post growth annealing of (Ga,Mn)As layers is an established method to increase the Curie temperature by the out diffusion of interstitial Mn ions [1]. The interstitial Mn are double donors in (Ga,Mn)As, so they compensate the itinerant holes responsible for mediating the ferromagnetic interaction between the substitutional Mn ions, resulting in a decrease of the Curie temperature and the electrical conductivity. For Mn doping levels larger than ~2.5%, [2] it becomes energetically favorable for interstitial Mn to form in order to compensate the large hole density created by the substitutional Mn.

One strategy that has been proposed to prevent the formation of interstitial Mn is to incorporate some other compensating atom during the growth of the layer. If a large density of such compensating atoms is incorporated during the growth then it may cause more Mn ions to be incorporated onto substitutional sites than would otherwise be possible under the same growth conditions. In theory, hydrogen is the best candidate. Because the hydrogen atoms are much smaller than the other atoms in the (Ga,Mn)As system, it is anticipated that they will occupy interstitial sites in the (Ga,Mn)As lattice during the growth and act to compensate the hole density. It should then be relatively easy to remove these atoms by out diffusion during post-growth annealing in order to increase the hole density.

Several 25nm ($Ga_{0.88}Mn_{0.12}$)As layers have been grown by Dr. R. Campion in the MBE system with the presence of atomic hydrogen, and the growth temperature is around 205ºC. In the next part we investigate the effects of growing in the presence hydrogen on the Curie temperature, the electrical resistivity and carrier density, in comparison to the (($Ga_{0.88}Mn_{0.12}$)As control sample discussed in Chapter 2 which was grown under the same growth conditions, but without the presence of hydrogen). The dependence of the Curie temperature, carrier density and conductivity on the annealing time and the annealing temperature is also investigated. Appendix B will present the technical details of instruments which have been used for the research in this chapter, including the MPMS SQUID magnetometer, the Oxford Instruments "Variox" ^{4}He cryostat system with up to 0.6T external magnet, and the Cryogenic ^{4}He magneto-cryostat system with up to 16T superconductor magnet.

3.2 The SQUID magnetometer measurements of H-doped sample

To start with, SQUID magnetometer measurements were performed on step annealed films of H-doped 12% nominal Mn samples to get the relationship between T_C and saturation magnetization.

The sample has been put into the SQUID and warmed up to 400K (which is high enough to cause some diffusion of hydrogen and is also the maximum temperature for the standard Quantum Design MPMS-XL system) for step annealing. In order to measure the change of magnetic properties after each step, the sample was cooled down to 2K with 1000Oe magnetic field applied and the remanence measurement was performed from 2K to 100K. Figure **3.1** is the remanence of the sample along [1-10], which shows that both the T_C and magnetic moment increased after annealing. It was also found that the magnetic anisotropy changed from [100]/[010] bi-axial to [1-10] uniaxial easy axis.

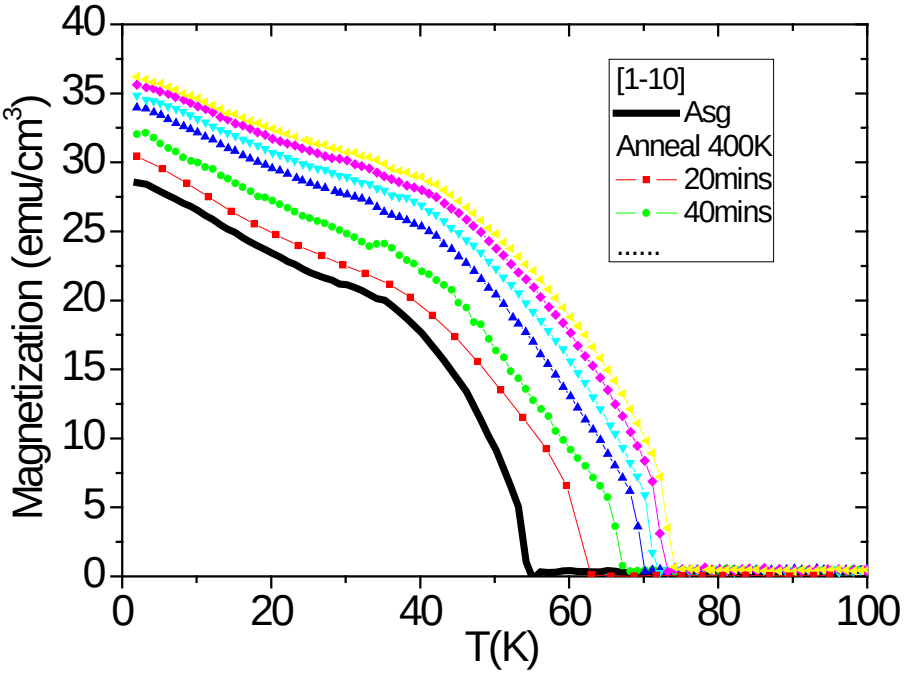

Figure 3.1 *Projection of temperature dependent remnant magnetization along [1-10] direction of the H-doped sample which has been step annealed in the SQUID at 400K, 20mins for each step.*

In order to reduce the time of achieving fully annealed status, the sample was taken out from the SQUID after 6 steps (about 2 hours) annealing (because the change of magnetic property became tiny when annealing in the SQUID) to the oven for a 48 hours standard annealing at 180ºC. Figure **3.2** shows the temperature dependence of the remnant magnetization for the fully annealed sample. It has uniaxial anisotropy with easy axis along [1-10], which is the same as the standard nominal 12% Mn sample's results (control sample) presented in Chapter 2. However, the values of T_C and magnetization at 2K for this sample (165K and 53emu/cm^{-3} respectively) are much lower than the control sample (182K and 72emu/cm^{-3} respectively). The relation between T_C and the saturation magnetization (M_s which equals magnetization measured at 2K) by step annealing is shown in Figure **3.3**. The data for fully annealed sample has been shown in the Figure **2.11** as well, which close to the previous nominal 8% (Ga,Mn)As sample's result.

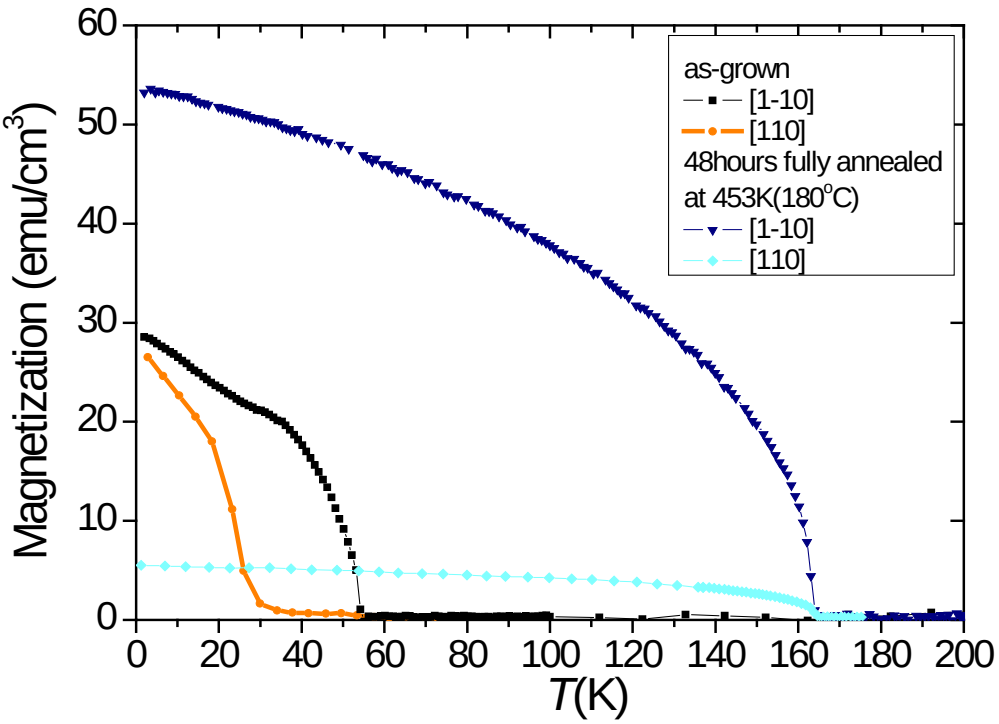

Figure 3.2 *Projection of temperature dependent remnant magnetization along [1-10] and [110] directions of the H-doped sample as-grown and fully annealed at 127ºC (400K) for 2 hours plus 180ºC for 48hours.*

Why the H-doped sample has a lower T_C and saturation magnetization than the control sample is not currently known, but may be related to an effect of the presence of hydrogen on the As pressure during the growth. As shown in Chapter 2, a low

As:(Ga+Mn) ratio can result in a remarkable reduction of the T_C and M_s. Therefore, if the hydrogen results in an effective decrease in the As pressure (for example, by the formation of As hydrides which desorbs readily from the surface), then this may explain the reduced T_C and M_s.

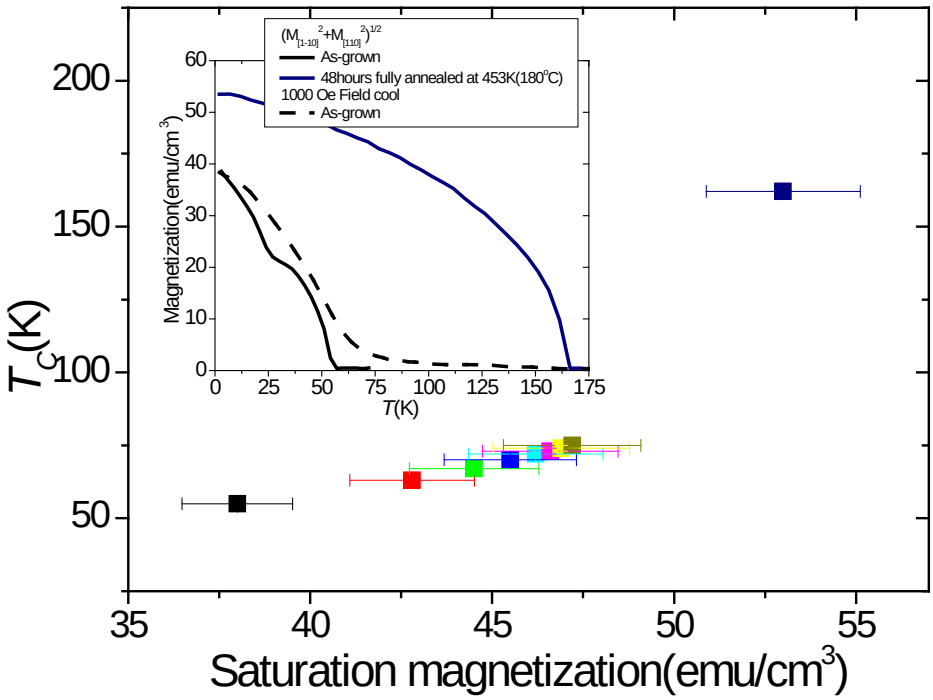

Figure 3.3 *Curie temperature vs. saturation magnetization in step annealed H-doped samples. Inset is the remnant magnetization of as-grown and fully annealed samples. The kink at 25K for the as-grown remnant magnetization curve is due to the re-orientation of the magnetization, where the single domain model is not suitable to be used. The 1000 Oe field cool curve for as-grown sample is presented as well, and the value of magnetization at 2K is around 38emu/cm^3 for both field cool and remnant magnetization curves.*

The density of effective Mn can be calculated from the saturation magnetization. In the following discussion, it is assumed that any interstitial Mn present is attracted to a substitutional Mn acceptor and that the pair couples anti-ferromagnetically. [3] Then the effective uncompensated Mn density will be $Mn_{eff} = Mn_{Ga} - Mn_I$. For the fully annealed samples, Mn_I is zero on the assumption that the interstitial Mn atoms have been removed entirely, therefore $Mn_{eff} = Mn_{Ga}$. The error bar of Mn_{eff} is around 3%, including errors in the size of the sample, also the miss alignment of the crystal direction during the measurement. Assuming one effective Mn gives $4\mu_B$ moment,

the concentration of each type of Mn in the 25nm thick H-doped (Ga,Mn)As layer is the $Mn_{Ga} = 14.3 \times 10^{20} cm^{-3}$ and the $Mn_I = 4.1 \times 10^{20} cm^{-3}$. The actual total Mn density $Mn_{total} = Mn_{Ga} + Mn_I = 18.4 \times 10^{20} cm^{-3}$, assuming the MnAs or any other Mn impurities can be neglected. The complete data considering all the errors is presented in Table **3.1** (page 77).

The density of Mn can be written in the form of Mn percentage, by using

$$Mn\ density = \frac{4x}{l_a^3} \Rightarrow x = \frac{Mn\ density \times l_a^3}{4} \tag{3-1}$$

In the equation, x is the substitutional Mn percentage (x_s) or the interstitial Mn percentage (x_I). l_a is lattice constant of (Ga,Mn)As, and l_a^3 is the volume of the unit cell. From the calculated results in ref. 4 and also the experimental results from ref. 5, the lattice constant of (Ga,Mn)As (with 1% to 10% Mn) changes less than 1% from the GaAs lattice constant ($a_0 = 5.653 Å$). To simplify the calculation procedures, it is possible to use a_0 to replace the actual value of the (Ga,Mn)As lattice constant. ($l_a \approx a_0$) The calculated results are x_s =6.5% and x_I =1.9%. The actual total Mn percentage (x_s+ x_I) is 8.4%, about 68% of the nominal Mn percentage.

On the other hand, from the SQUID results for the control sample, the $Mn_{Ga} = 19.4 \times 10^{20} cm^{-3}$ and the x_s is about 8.7%, the $Mn_I = 7 \times 10^{20} cm^{-3}$ and the x_I is 3.1%, the actual total Mn density is $26.4 \times 10^{20} cm^{-3}$ and the percentage is 11.8%, which is close to the nominal Mn percentage 12%. More research work needs to be done to find out how the H-doping change the growth condition which blocks the Mn atoms getting into the GaAs layer.

3.3 Transport measurements to achieve carrier density

3.3.1 Carrier density from the Hall measurement

Obtaining accurate values for the hole density is essential for establishing a detailed theoretical description of the (Ga,Mn)As system. However, the standard methods of

obtaining carrier densities, including electrochemical C-V profiling and optical techniques, are not applicable to these ultrathin films and the only realistic method is to use Hall Effect measurements.

As mentioned in Chapter 1, the Hall Effect in (Ga,Mn)As can be described by the sum of ordinary and anomalous terms:

$$R_{xy} = R_0 B + R_A \mu_0 M \tag{3-2}$$

The coefficient of ordinary term

$$R_0 = \frac{1}{ped} \tag{3-3}$$

has a direct relation with the carrier density p and the film thickness d of the sample. The coefficient of anomalous term has a relation with R_{xx} in the form:

$$R_A \propto R_{xx}^n \tag{3-4}$$

with the scaling exponent n equal to 1 or 2 from the different theoretical models. (Skew-scattering [6], Side-jump [7] or the intrinsic mechanisms related to the Berry phase [8])

Even though, obtaining carrier densities in (Ga,Mn)As films from Hall Effect measurements has proved to be problematic, especially for lightly doped or heavily compensated materials due to the presence of the anomalous Hall Effect, which at low temperatures is much larger than the ordinary Hall effect from which one wishes to obtain the carrier densities. Next section will present some experimental work to obtain carrier densities of (Ga,Mn)As and H-doped (Ga,Mn)As by the Hall Effect measurement.

3.3.2 Low temperature Hall measurements for the fully annealed samples

The large anomalous Hall Effect dominates the slope of the Hall resistance even at high magnetic fields. The most common approach used to extract the small ordinary Hall term is to measure the total Hall resistance as a function of field and temperature in the regime of high magnetic fields and low temperatures in which the magnetization **M** should be saturated, thus enabling one to determine the relationship

between R_A and $R_{xx,}$ and to separate the contributions of R_0B and R_A to the Hall slope. This was first done systematically for a range of Mn concentrations by the Nottingham group. [9]

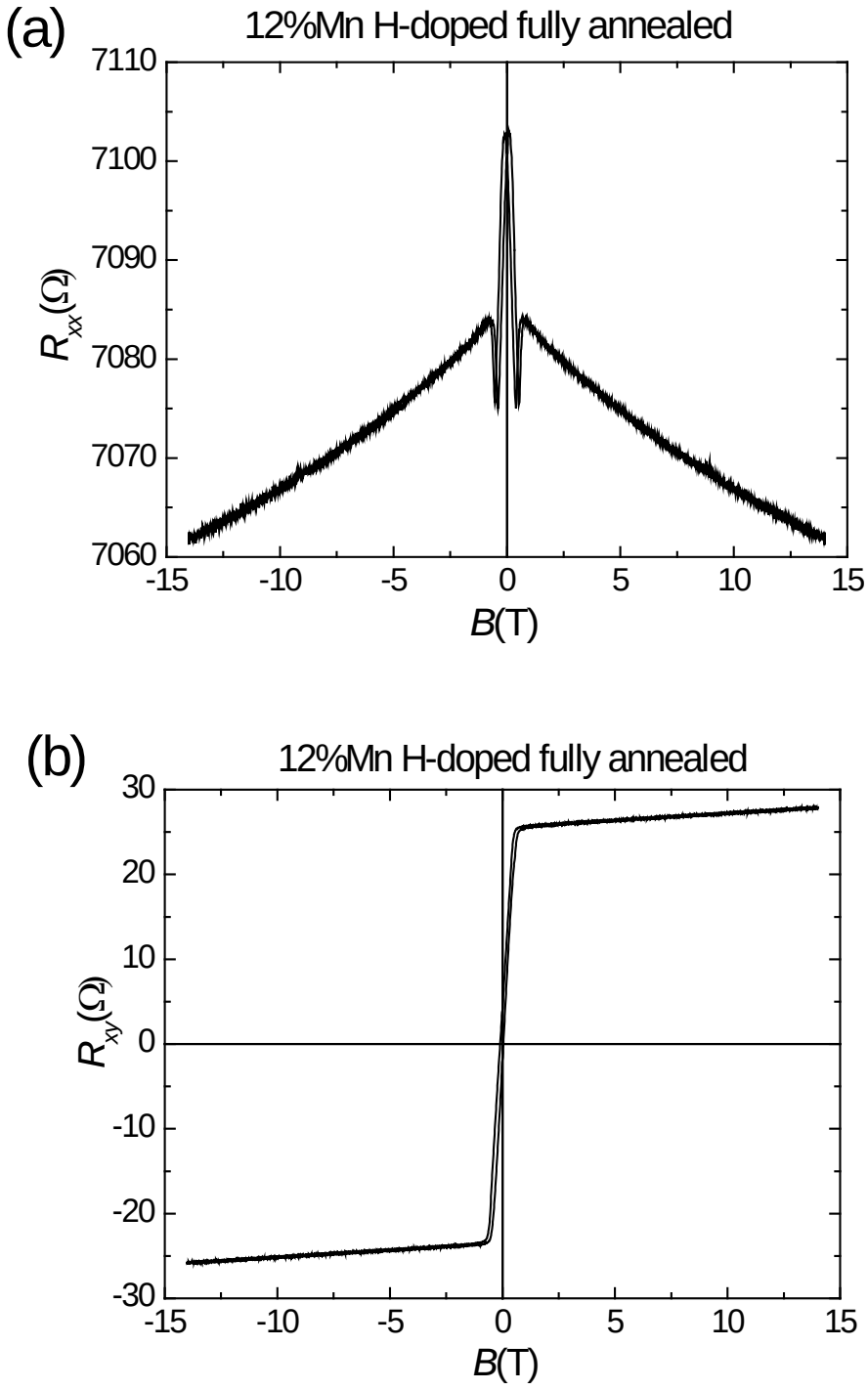

Figure 3.4 *(a) Longitudinal resistance (R_{xx}) and (b) Hall resistances (R_{xy}) vs. magnetic field* **B** *up to 14T at 2K for the H-doped fully annealed sample.*

Figure **3.5** shows the Hall resistance *vs.* magnetic field (from Figure **3.4**(b)) up to 14T at 2K for the fully annealed hydrogen sample, compared to the fitted curves obtained using equation

$$R_{xy} = R_0 B + C R_{xx}^n \ (n = 1 \, or \, 2) \tag{3-5}$$

, assuming that the magnetization is saturated above 3T. Due to the relatively small high field magnetoresistance, the obtained carrier density is only weakly dependent on the exponent *n* used to describe the relationship between R_A and R_{xx} (from Figure **3.4**(a)), and the ordinary Hall coefficient can be obtained with an accuracy of around 5%. The carrier density is around $(1.4 \pm 0.1) \times 10^{21} cm^{-3}$ for the H-doped fully annealed sample, and approximately $(1.8 \pm 0.1) \times 10^{21} cm^{-3}$ for the control sample.

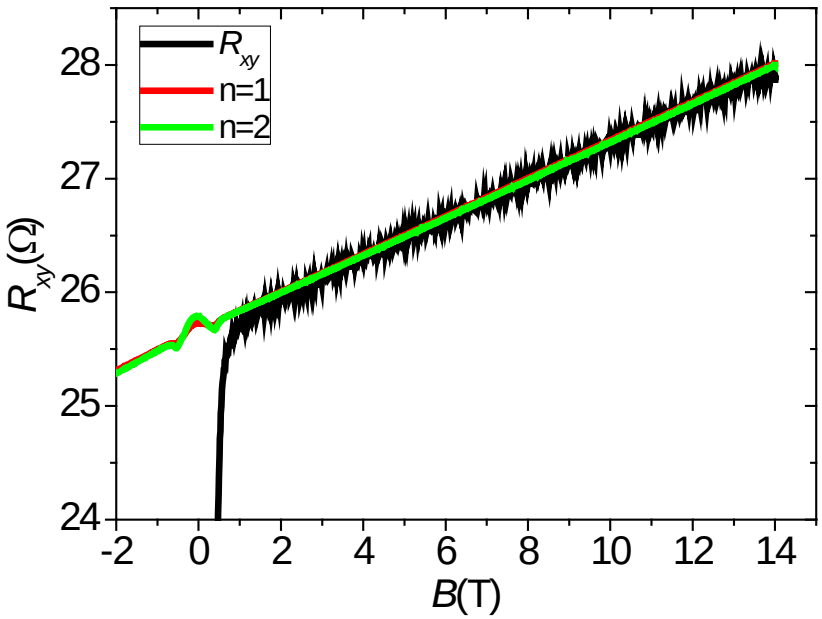

Figure 3.5 *Fitting of the Hall resistance of the fully annealed H-doped sample with the scaling exponent n=1 and 2.*

However, this method is only effective for relatively highly conducting samples in which the magnetoresistance is quite weak (typically, less than 20% change over the range 2-10T). For the highly compensated low carrier density layers like the as-grown hydrogen doped samples, the emergence of very large magnetoresistance has been found, and the scaling relation of the anomalous Hall Effect is complex. Some groups report the scaling exponent $n<1$, [10-12] which is not predicted by any existing models. This has previously precluded direct measurements of carrier densities. The next section will discuss some methods which may make it possible to get reasonable values of carrier density for this kind of samples.

3.3.3 High temperature Hall measurements for H-doped as-grown sample

Rearranging Eq. 3-2 and assuming the power-law relationship (Eq. 3-4) gives the following expression for the slope of R_{xy} at low fields and high temperatures:

$$\frac{R_{xy}}{B} = R_0 + R_A\chi \tag{3-6}$$

In this regime the paramagnetic susceptibility χ is expected to follow a Curie-Weiss dependence on temperature in the form:

$$\chi = \frac{C}{T - T_{cw}} \tag{3-7}$$

The Curie-Weiss temperature (T_{cw}) is slightly larger than the T_C which is a common thing in ferromagnetic materials. [13] The Eq. 3-5 changes to

$$\frac{R_{xy}}{B} = R_0 + C_1 R_{xx}^n \left(\frac{C_2}{T - T_{cw}}\right) \tag{3-8}$$

Therefore, this should asymptotically approach the ordinary Hall coefficient at the high temperature limit, as the anomalous term becomes smaller than the ordinary term.

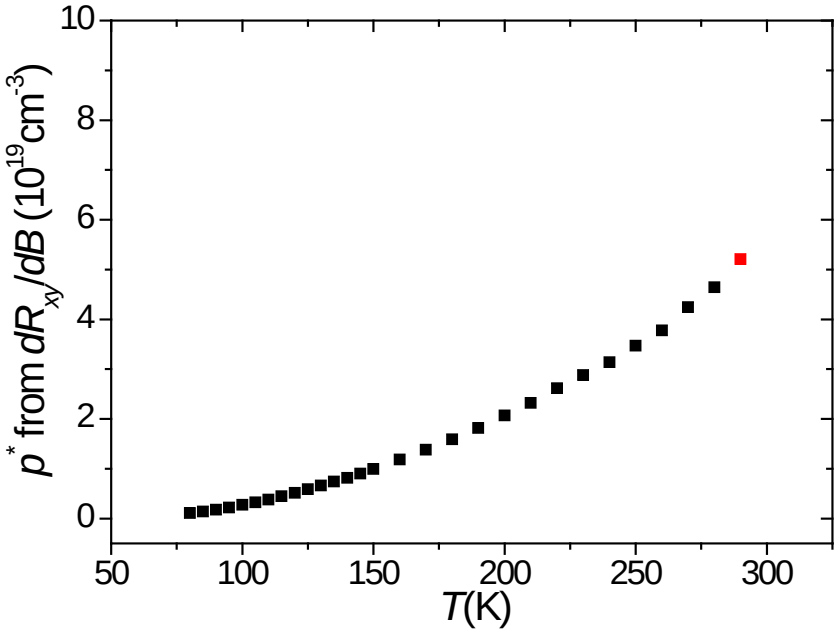

Figure 3.6 *Apparent hole density p* obtained from the linear Hall slope above T_C (55K) for the H-dope as-grown sample.*

Figure **3.6** presents the temperature dependence of p^* from the Hall slope without removing the anomalous part for the H-doped as-grown sample. (Eq. 3-8)

$$p^* = \frac{1}{R_0^* de} = \frac{1}{\frac{dR_{xy}}{dB} de} \tag{3-9}$$

The value of p^* increases remarkably as the temperature rises from 75K to 290K (room temperature). It is difficult to do more measurements above 290K, because the sample will start to be annealed.

From the figure, it is obvious that the value of p^* is not saturated at room temperature and could become much larger if the temperature keeps increasing. This suggests that when obtaining carrier densities from measurements of the room temperature Hall slope directly, assuming that the anomalous contribution would not be significant, you generally get values of carrier density which are significantly less than the true values. This is because even well above the ferromagnetic transition temperature, the paramagnetic susceptibility, which is close to linear, can give a substantial contribution to the linear Hall slope due to the large R_A. In that case, the real value of carrier density should be above $p^*(290K) \approx 5\times10^{19} cm^{-3}$ for the H-doped as-grown sample.

In order to obtain a reasonable value of the carrier density, the contribution of the magnetic susceptibility needs to be removed from the Hall slope. By investigating the temperature-dependence paramagnetic susceptibility from SQUID magnetometer measurements, the R_{xy}/B term might extrapolate to the ordinary Hall coefficient.

Figure **3.7** presents the paramagnetic susceptibility (from 60K to 150K) measured in the SQUID. Because of the limit of the size of the sample, the resolution of the SQUID measurement and the large diamagnetic background (10^{-4}emu/T) from GaAs substrate, it is difficult to get the small value of paramagnetic susceptibility from experiments when the temperature is much higher than T_C. The susceptibility at high temperature (Red line) was simulated by using the Curie-Weiss law (Eq. 3-7), with $C = 1.2\times10^{-4} K\cdot emu/T$ and T_{cw} =57K. The results from 75K to 150K follow the theory very well, and the curve predicts the

susceptibility at 300K is $5\times10^{-8} emu/T$ which is much smaller than the diamagnetic background and impossible to be obtained from the SQUID magnetometer.

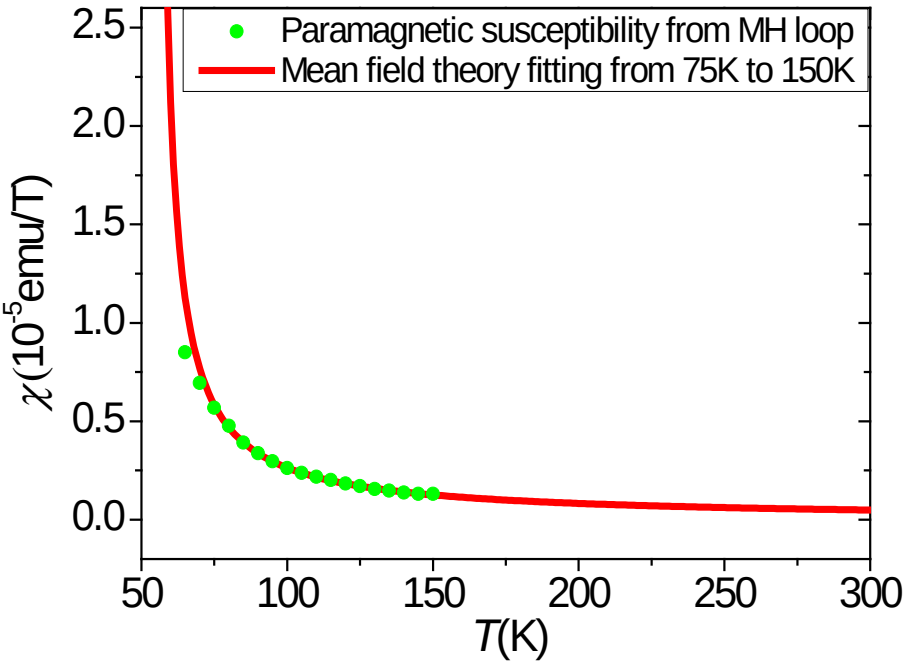

Figure 3.7 *Paramagnetic susceptibility χ for the H-dope as-grown sample obtained by SQUID measurement. (60K to 150K) Due to the resolution of SQUID measurement, the susceptibility above 150K is achieved by using Curie-Weiss law (Eq. 3-7) to do the fitting. (Red line in the figure and the fitting range is from 75K to 150K)*

Figure **3.8**(a) and (b) are the graphs of R_{xy}/B *vs.* $R_{xx}\chi$ and $R_{xx}^2\chi$ for the as-grown hydrogen doped samples, over the temperature range from just above T_C up to 290K. Although R_{xy}/B decreases strongly over the measured temperature range (by almost a factor of 50), it still shows a marked temperature-dependence of coefficient C_1 (from Eq. 3-8) even at the highest temperatures studied. This indicates again that the anomalous Hall Effect contributes strongly to R_{xy}/B even at room temperature where the paramagnetic susceptibility is very small. It is impossible to extrapolate to the limit where $R_{xy}/B = R_0$ without improved knowledge of the temperature-dependence of the $C_1 R_{xx}^n$ term.

To conclude: At room temperature, the anomalous Hall Effect may still be the main contribution to the measured Hall slope, and furthermore its complex temperature-dependence precludes an extraction of the ordinary Hall coefficient based on an analysis of the magnetic susceptibility. Therefore, accurate determination of the carrier density for weakly conducting H-doped as-grown (Ga,Mn)As films remains problematic.

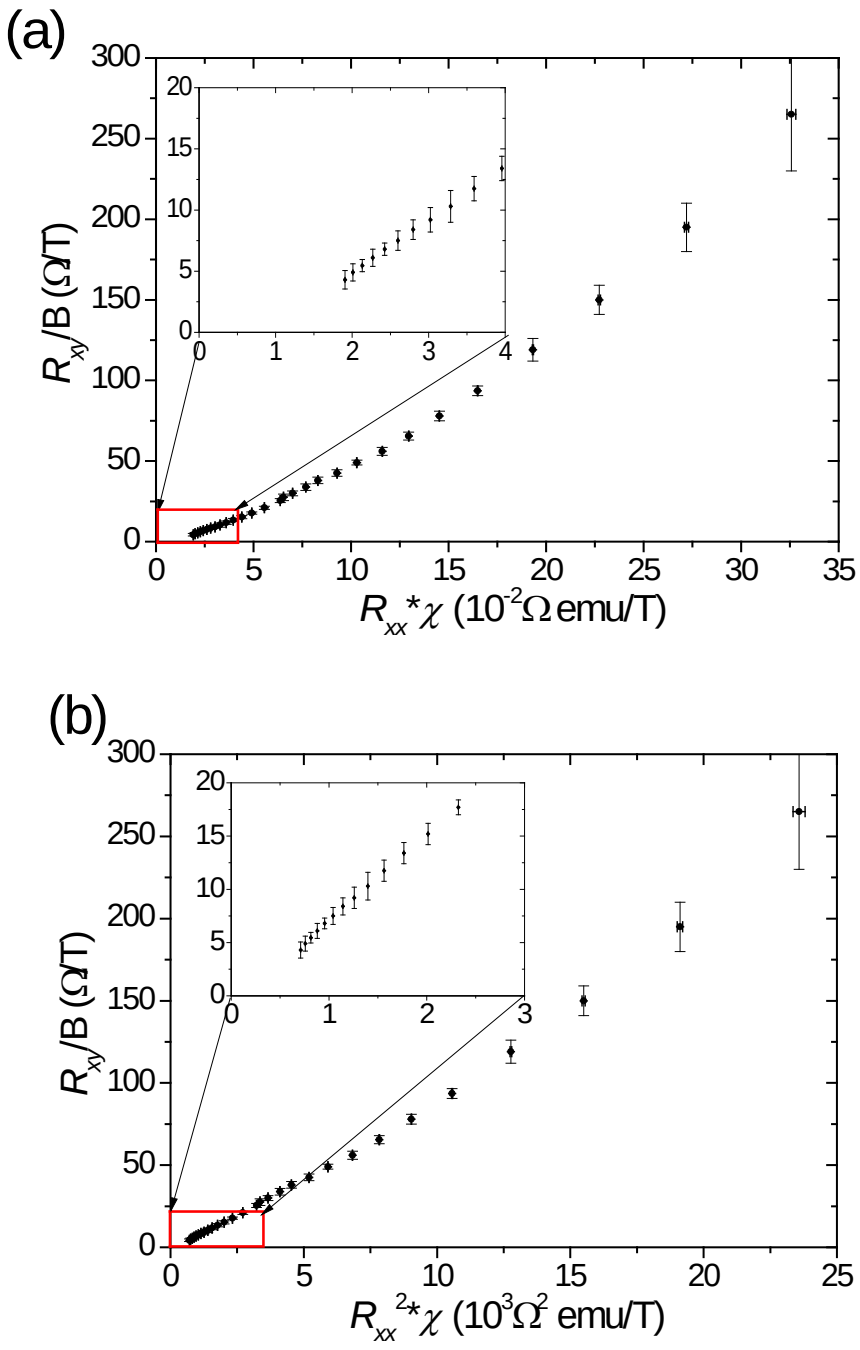

Figure 3.8 *The graphs of R_{xy}/B vs. $R_{xx}^n\chi$ for the H-doped sample where (a) n=1 and (b) n=2, to extrapolate to the ordinary Hall coefficient.*

3.3.4 Low temperature Hall measurements for the H-doped as-grown sample

It is difficult or even impossible to measure the carrier density of the H-doped as-grown sample directly. However, systematic fitting procedures, using a consistent set of parameters, on step-annealed samples with a wide range of conductivity, can yield reasonable values of carrier density.

First, the sample was annealed step by step at 120ºC for 145 hours. After that, the sample was annealed at 180ºC for another 45 hours, in order to remove all the interstitial Mn defects and achieve fully annealed state. Figure **3.9** and **3.10** are the temperature dependence curves of R_{xx} and dR_{xx}/dT after repeated annealing step. The low temperature Hall measurements were performed after each step with the external magnetic field up to 14T. Figure **3.11** shows the dependence of R_{xx} and R_{xy} on magnetic field at 2K after each step.

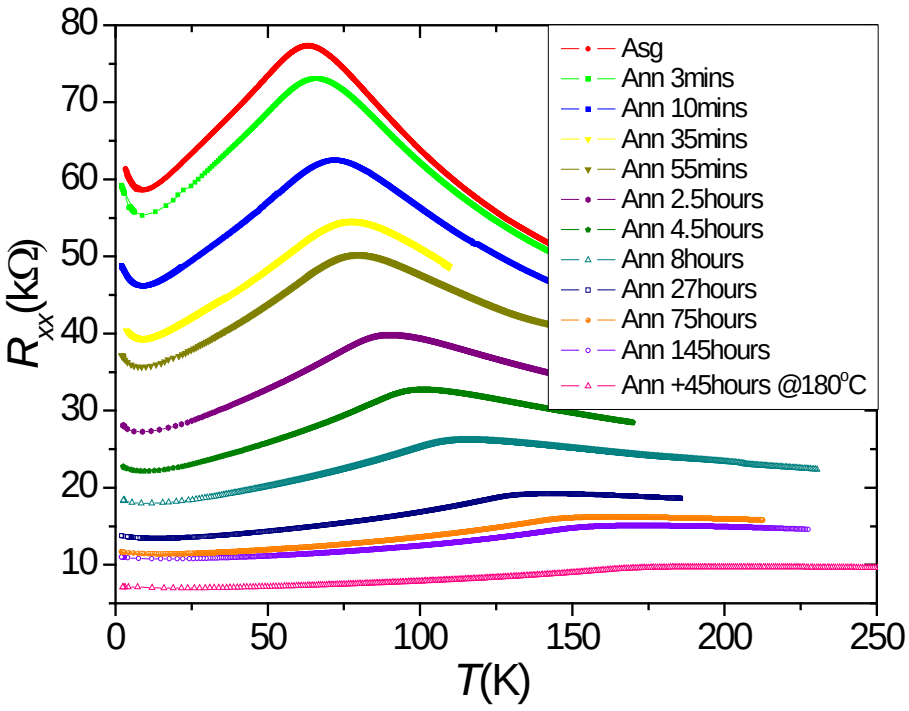

Figure 3.9 *R_{xx} vs. temperature for the H-doped (Ga,Mn)As after repeated annealing steps at 120ºC. The annealing temperature is 180ºC for from 100 hours to 145 hours, in order to reduce the fully annealing time.*

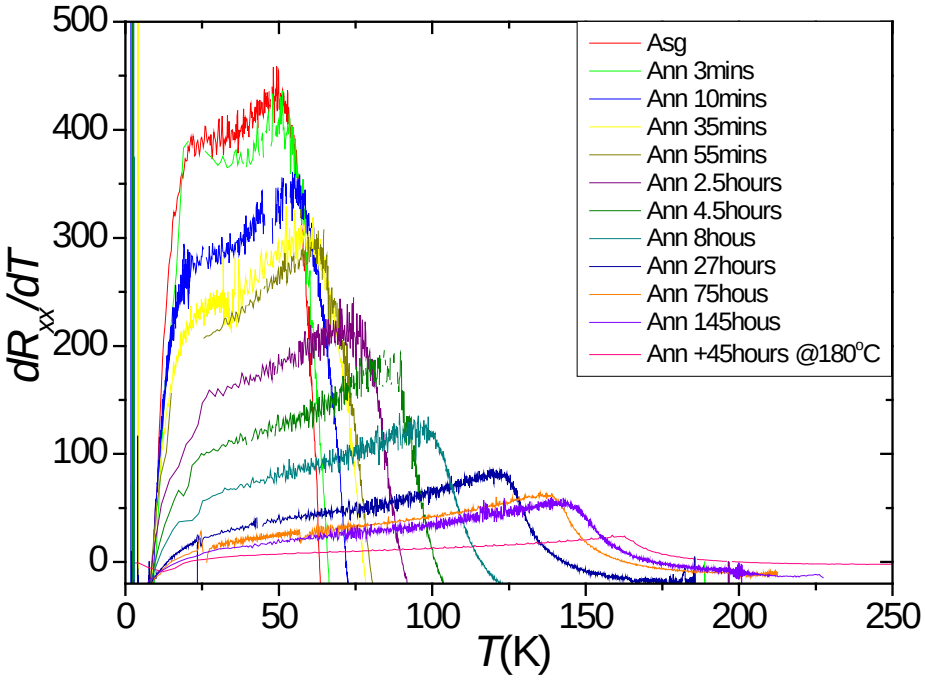

Figure 3.10 *The dR_{xx}/dT curves after each annealing step. The T_C is determined from the peak point of each curve.*

Eq. 3-5 with three parameters R_0, C and n ($1<n<2$) is used for the fitting in the high magnetic field region where the magnetization **M** should be saturated. The fitting starts from the fully annealed curve to partially annealed curves, because it is easier to do the fitting where the isotropic magnetoresistance is smallest Consistent values of p can be obtained across the series from the 145 hours fully annealed state to the 35mins slightly annealed state. (Figure **3.12**) The anomalous part becomes very large for the first few annealing steps (as-grown to 35mins annealing), where it is difficult to do the fitting. In another way to do the fitting, the parameter n is fixed to 1 or 2, which gives the upper and lower limit of p. From Figure **3.13** it can be observed that fitting with different n gives nearly 50% different for the slightly annealed data, but less than 5% for the fully annealed sample. Considering the results from three different fitting methods, the carrier density is $(1.0\pm0.5)\times10^{20}\,cm^{-3}$ for the 35mins slightly annealed sample. As the carrier density of (Ga,Mn)As can only become larger after annealing, the carrier density of as-grown state is between $0.5\times10^{20}\,cm^{-3}$ (the results from room temperature Hall measurement (Figure **3.6**)) and $1.5\times10^{20}\,cm^{-3}$. It is assumed that the carrier density is temperature independent. [2]

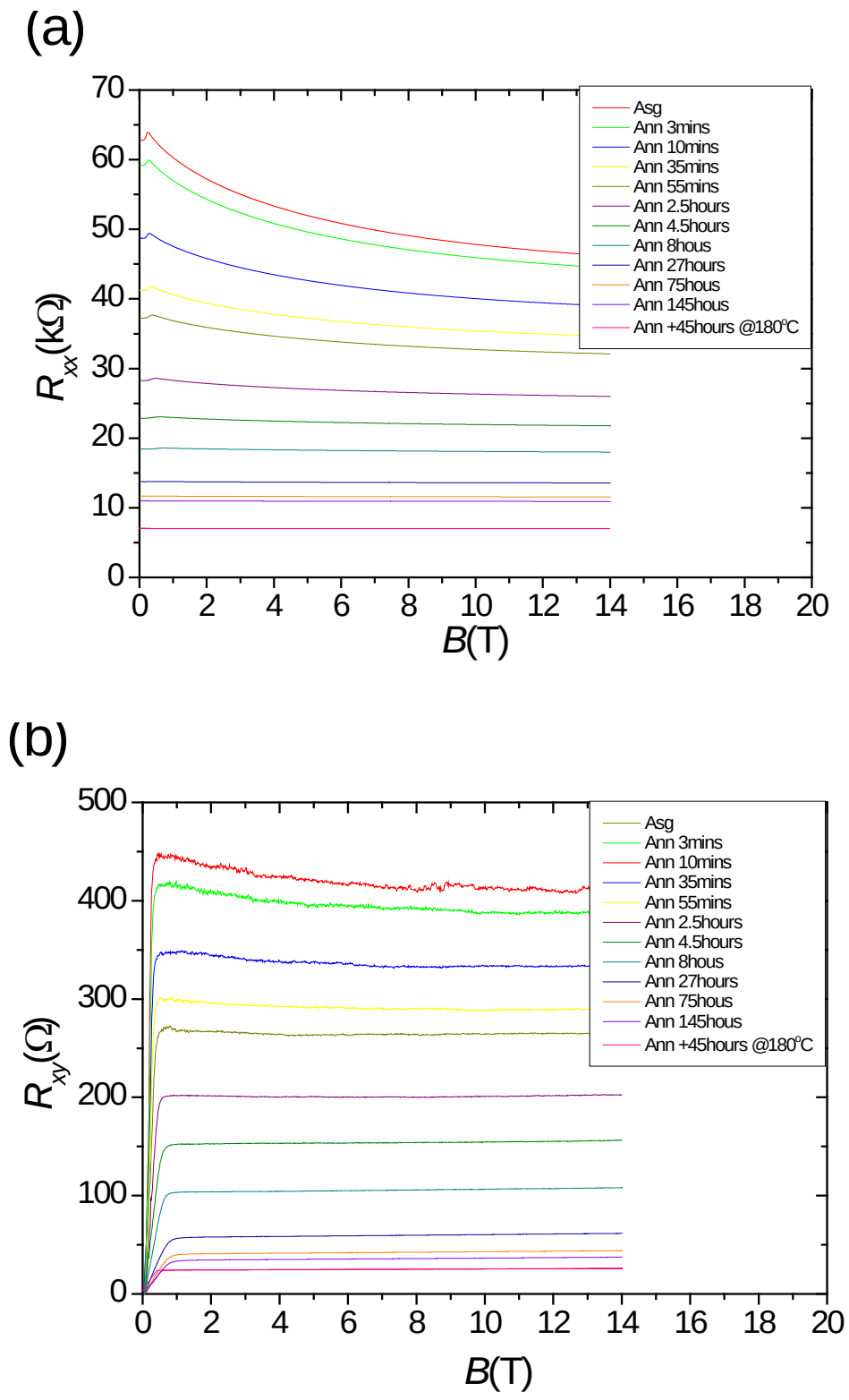

Figure 3.11 *(a) R_{xx} and (b) R_{xy} vs. magnetic field B up to 14T measured at 2K*

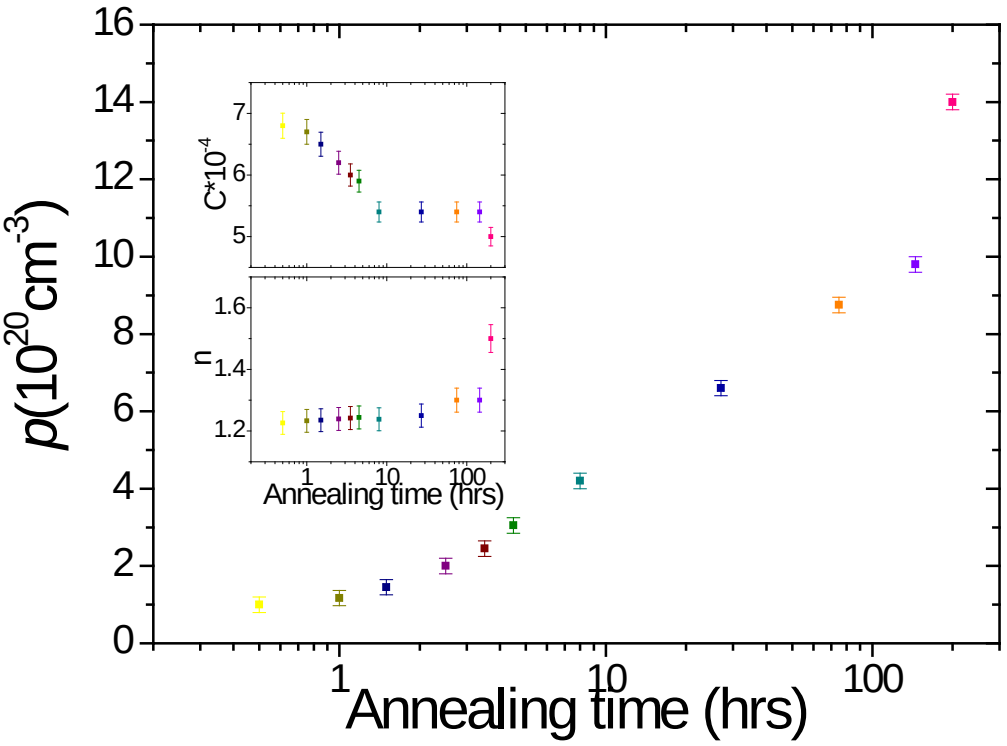

Figure 3.12 *Carrier densities vs. annealing time, by using Eq.3-5 with three parameters: R_0, C and n (1<n<2) for the fitting. The fitting starts from the fully annealed sample to the partially annealed sample. Inset: the fitting parameters C and n for each annealing step. The annealing temperature of the last step is 180ºC.The error bar of carrier densities comes from the fitting error. The colors of the points are consistent with the colors of the curves in Figure* **3.9**, **3.10** *and* **3.11**.

The annealing temperature 120ºC is relatively low for the diffusion of interstitial Mn, and the fully annealing time is about 11,000 hours by the diffusion model (Eq. 2-2). However, the step annealing results show that only a few hours annealing changed the sample's properties quite a lot. This is mainly due to the presence of hydrogen atoms which are easy to diffuse to the surface at low temperature. Another reason is because this highly compensated sample has high concentration of interstitial Mn. Even though the annealing temperature is low, a lot of interstitial Mn in the top few nanometers still can be removed easily. Figure **3.13** shows that the annealing became less effective after 75 hours and up to 10,000 hours is needed for the sample to achieve fully annealed state. It is better to increase the annealing temperature to reduce this time, so the last annealing step was performed at 180 ºC.

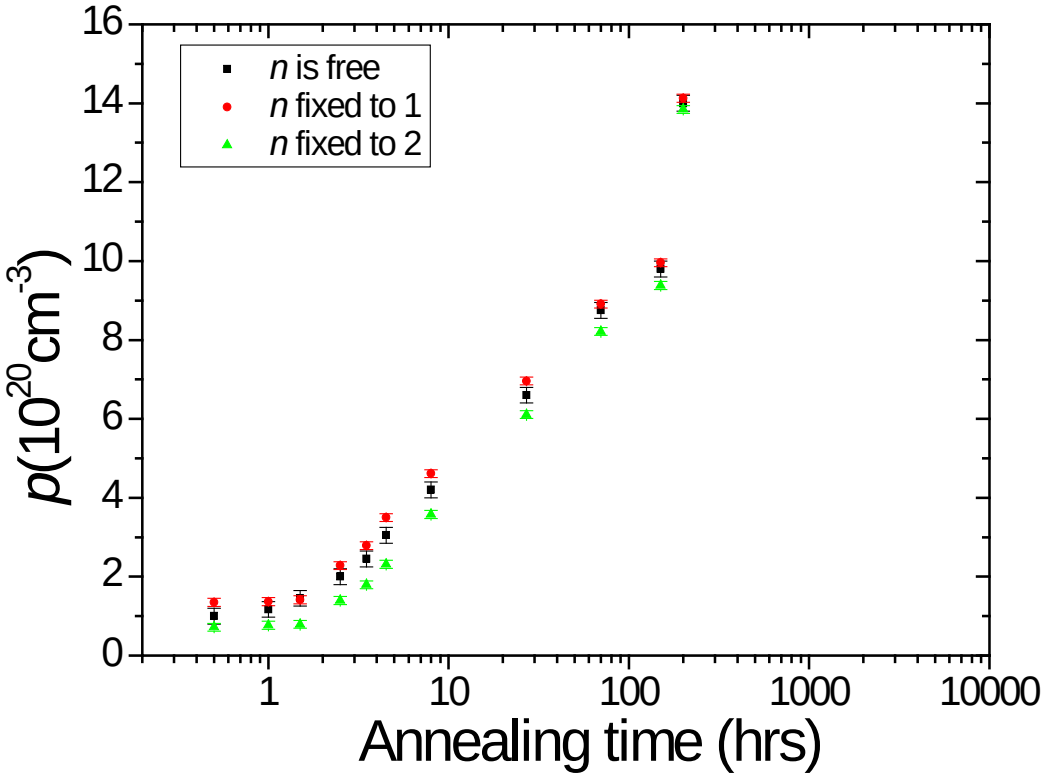

Figure 3.13 *Carrier densities vs. annealing time by using different fitting methods. (n is fixed to 1 or 2) The definition of error bar is the same as the previous figure.*

3.3.5 The relation between T_C and carrier density

The plot of T_{dRdT} (from the peak point of dR_{xx}/dT curve [14] from Figure **3.10**), T_{RT} (from the peak point of dR_{xx}/dT curve from Figure **3.9**) and T_C from temperature dependent remnant magnetization curve *vs.* carrier densities p has been shown in Figure **3.14**. It is clear that the T_{dRdT} rather than the T_{RT} is close to the T_C for both partially and fully annealed samples and T_{dRdT} will be use as the T_C in the rest of discussions in this chapter.

Figure **3.15** plots T_C *vs.* carrier densities for the H-doped sample (by step annealing method) and the 12% Mn control sample (as-grown: $(4\pm1)\times10^{20}\,cm^{-3}$ and fully annealed: $(1.8\pm0.1)\times10^{21}\,cm^{-3}$), together with the previous results of 1.7 to 6% nominal Mn samples. [2] It also presents some results of step annealing 6% nominal Mn sample measured by Dr. K. Edmonds a few years ago. (Unpublished)

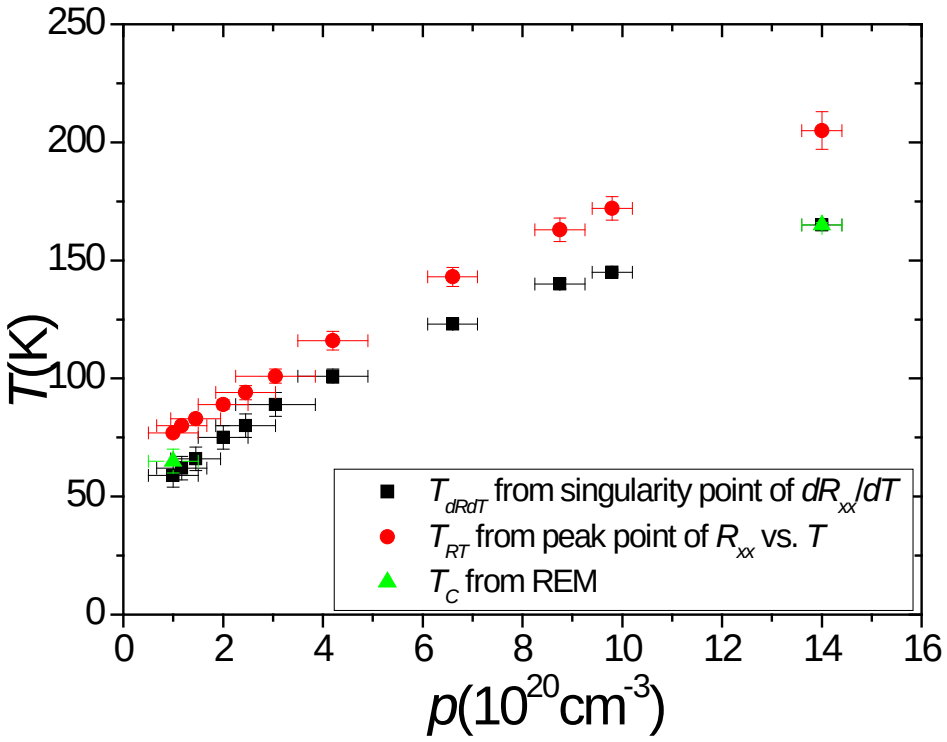

Figure 3.14 *T_{dRdT} (from the peak point of dR_{xx}/dT), T_{RT} (from the peak point of R_{xx} vs. T) and T_C (from remanence data) vs. carrier density p for the step annealed H-doped samples.*

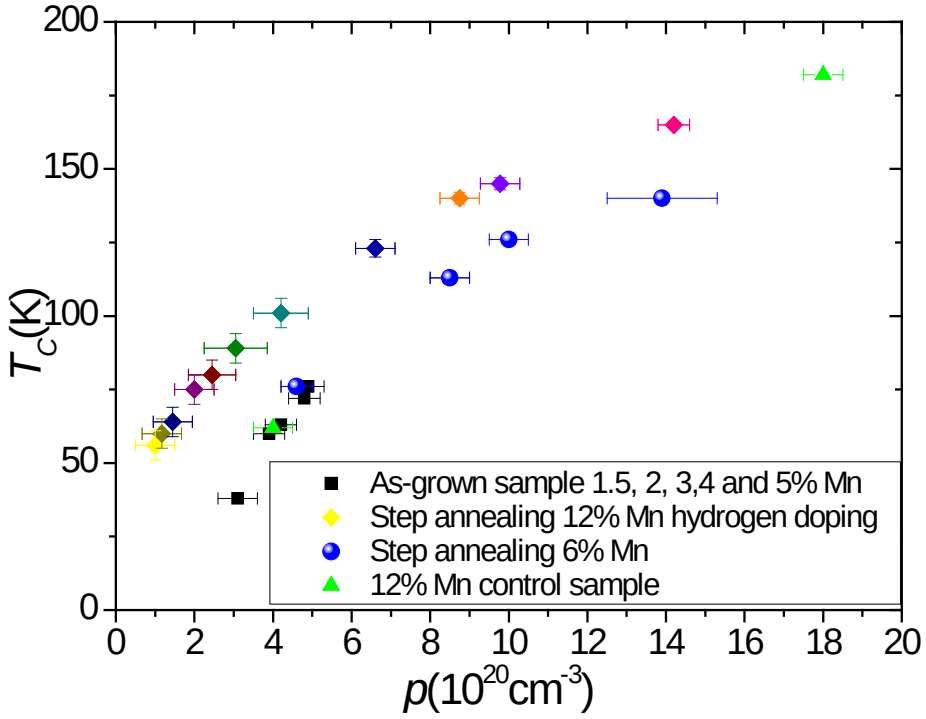

Figure 3.15 *T_C vs. carrier density for the H-doped samples (diamond points, the colors are consistent with the colors of the curves in Figure* **3.9**, **3.10**, **3.11***and points in Figure* **3.12***) compared to other (Ga,Mn)As samples with varying Mn concentration*

The key observation is that the as-grown and lightly annealed H-doped samples have relatively high Curie temperatures while the carrier density is quite low. According to Zener models of carrier-mediated ferromagnetism in (Ga,Mn)As, the relation between the Curie temperature, the carrier density and the saturation magnetization is in the form [2]:

$$T_C \propto M_s p^{1/3} \tag{3-10}$$

It is necessary to combine the results of the T_C and M_S from previous SQUID magnetometer measurement, before having a good understanding of this phenomenon.

3.4 The low carrier density sample achieved by H-doping

For the fully annealed hydrogen doped samples and also the control samples, the carrier density is consistent with the density of substitutional Mn (effective Mn) extracted from the magnetization, assuming 1 hole per substitutional Mn and negligible compensation, (red points in Figure **3.16**) continuing the trend that has previously been established in lower-doped samples. [2] For the as-grown sample, the hole per effective Mn ion is around 0.1, much lower than the control sample which has about 0.3 hole per 1 effective Mn ion.

All the results of magnetometry and transport measurement have been shown in the form of T_C per x_{eff} (effective Mn percentage) *vs.* hole per Mn_{eff}, which makes it easy to compare samples with varying Mn concentrations. (Figure **3.17**) It is clear that the red square points which represent the H-doped as-grown and lightly annealed sample exceed the prediction of the Zener mean field theory (the gray line in the figure). [2] Be contrast, the point of the 12% control as-grown sample is on the line, which suggests the control sample still follows the theory quite well. After being fully annealed, the properties of both of the samples are quite similar to the other fully annealed samples with varying nominal Mn concentrations. Assuming each effective Mn atom accepts 1 electron, while 1 hydrogen atom contributes 1 electron and 1 interstitial Mn atom contributes 2 electrons, it is possible to calculate that the hydrogen doping level is about $(5 \pm 2) \times 10^{20} cm^{-3}$ in the as-grown state.

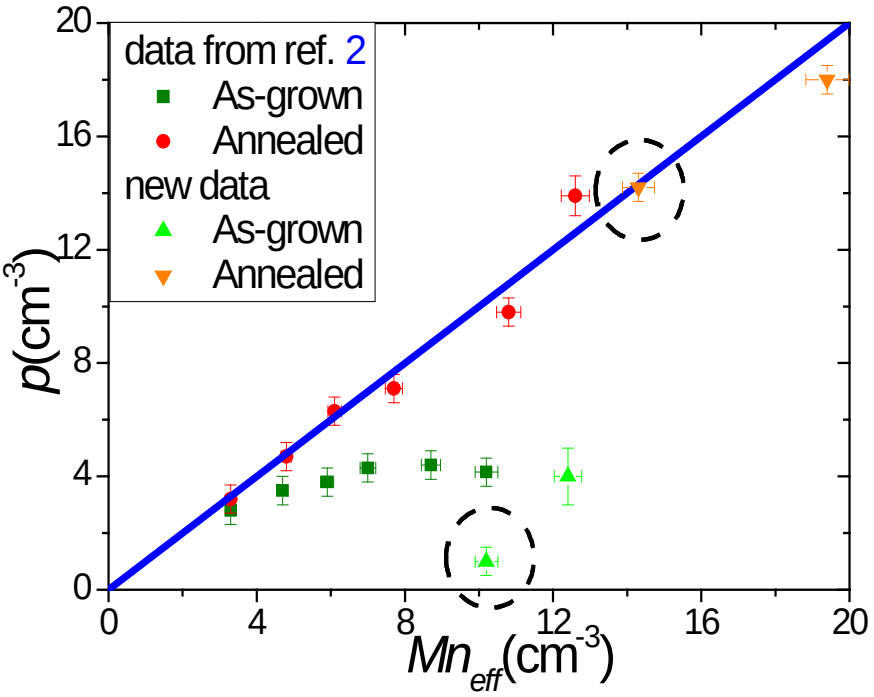

Figure 3.16 *Carrier densities vs. effective Mn concentrations of the as-grown and fully annealed (Ga,Mn)As samples with varying nominal Mn concentrations from 1.7% to 6.7% (from ref. 2) and 12% H-doped/control samples. The points in the black circles represent the H-doped sample. The blue line indicates the expected behavior assuming 1 hole per substitutional Mn and zero compensation.*

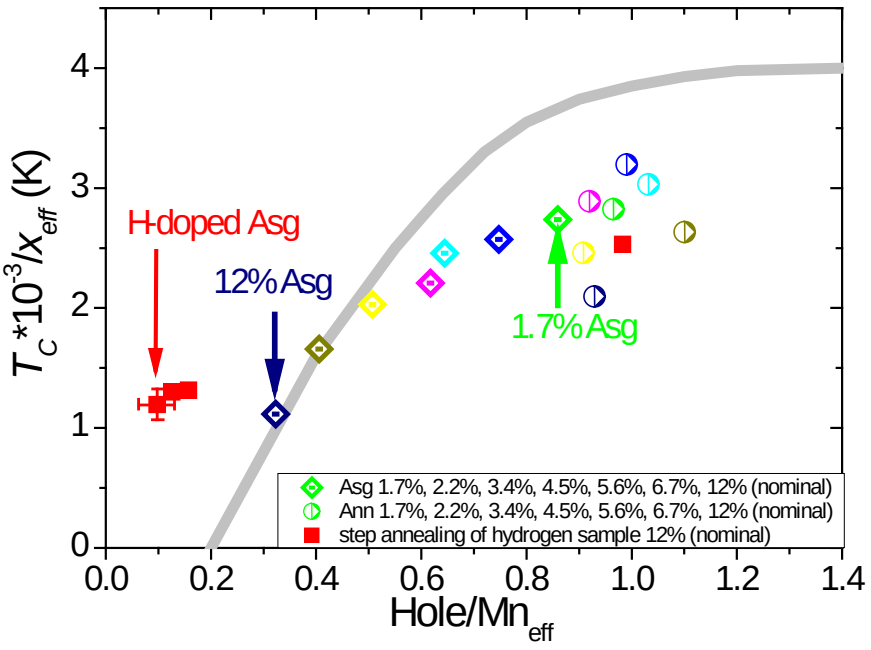

Figure 3.17 *T_C per x_{eff} vs. hole per Mn_{eff}. Red squares are for the step-annealed H-doped films, other points are for the as-grown and fully annealed $Ga_{1-x}Mn_xAs$ films with varying Mn concentration. Grey line is the theory prediction from ref. 2.*

3.5 The conductivity of H-doped and control samples

The electrical conductivity (σ_{xx}) has a relationship with hole density (p) and mobility (μ_p) in the form

$$\sigma_{xx} = ep\mu_p \tag{3-11}$$

The value of the elementary charge e is approximately 1.602×10^{-19} Coulombs.

Figure **3.18** is the graph of Curie temperature as a function of the conductivity measured at 2K and room temperature 300K for a series of Hall bars taken from the H-doped wafer and control wafer. The conductivity was measured by using a four terminal method and the Curie temperature was determined from the position of the peak point in dR_{xx}/dT [14]. Each sample was annealed over several time intervals at a given temperature and the Curie temperature and electrical conductivity were measured after each annealing step.

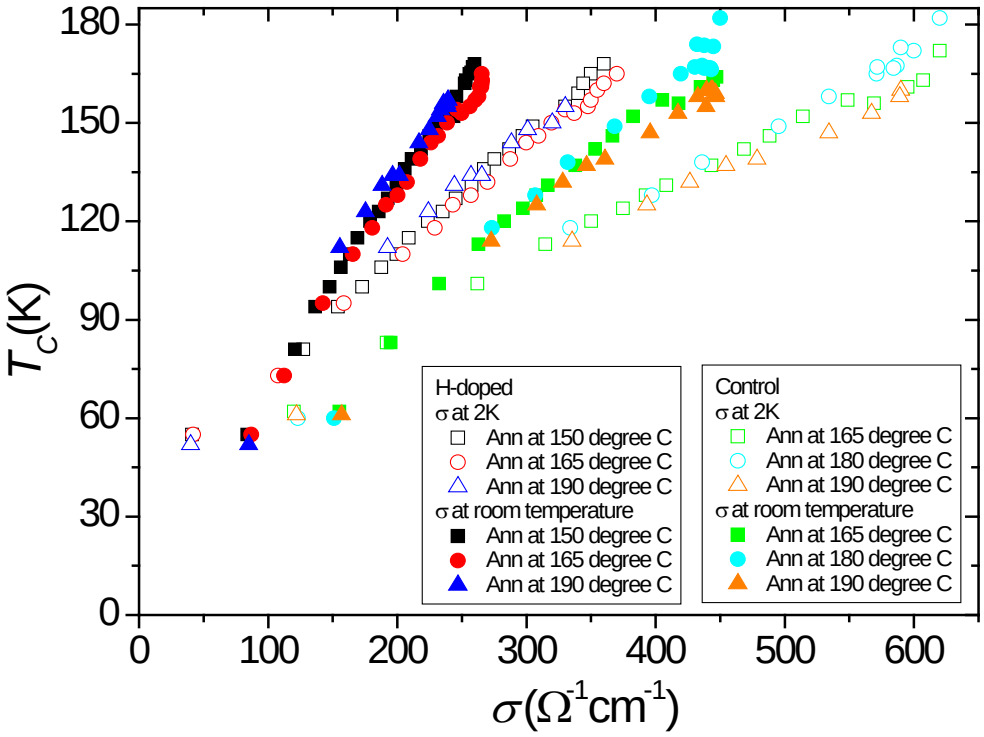

Figure 3.18 *T_C vs. conductivity at 2K and room temperature for H-doped and control samples. All the samples have been step annealed with different temperature.*

Several observations can be made about this data. For the as-grown sample, growing with hydrogen suppresses the room temperature conductivity by a factor of 1.9. On the other hand, the Curie temperature is suppressed by only 14% (55±5K compared to 62±5K for the control sample). After fully annealing, the conductivity of the hydrogen doped samples is still suppressed by approximately a factor of 1.8 compared to the control samples, and the Curie temperature is still suppressed by approximately 10%. (Highest T_C: 165K for the H-doped sample and 182K for the control sample) Assuming the carrier densities are temperature independent [15], the hole mobilities for the fully annealed H-doped sample and control sample have been calculated by using the Eq. 3-11 and shown in Table **3.1**. The conductivity at room temperature is larger than it is at 2K by a factor of 2 for the H-doped as-grown sample, while the factor is only about 1.3 for the control sample. After being fully annealed, this factor reduced to 0.7 for both of the two samples. This suggests that at low temperature the localization of carriers for the H-doped sample is stronger than the control sample.

3.6 Conclusion and future work

To conclude, all the magnetic and transport results of the new H-doped and control samples have been shown in Table **3.1**. As a comparison, Table **3.2** presents the previous data of the samples with varying Mn concentration (from 1.7% to 6.7%) measured by Dr. K. Y. Wang and Dr. K. Edmonds from the Nottingham group. [1,2,9]

By investigating the magnetic and transport properties of H-doped (Ga,Mn)As samples, we observe relatively high values of T_C at low conductivity and hole density for the as grown and lightly annealed hydrogen doped samples. Indeed extrapolation suggests that T_C would be finite for zero conductivity. In other studies [16] it has been found that one can have ferromagnetism in insulating (Ga,Mn)As samples. The explanation for this is that the holes have too small a localisation length to give a finite conductivity but that this length is still larger than or comparable to the separation of the Mn atoms and so they can still mediate the ferromagnetic order. Similarly the probable explanation of the relatively high T_C values for very low carrier densities is that the localisation length is relatively small so that the measured

carrier density is that of delocalised holes while the number of holes mediating ferromagnetism is larger. Such layers may be good candidates for showing strong gate control of ferromagnetism. At the same time, more work on investigating the best growth conditions for H-doped (Ga,Mn)As needs to be done, as the hydrogen has been found to reduce the incorporation of Mn and also T_C.

	H-doped		control	
Nominal total Mn % (x_{total})	12%		12%	
	As-grown	Annealed	As-grown	Annealed
Saturation magnetization(M_s) (emu/cm^{-3})	38±1	53±2	46±1	72±2
Effective Mn density (Mn_{eff}) (10^{20}cm^{-3})	10.2±0.3	14.3±0.4	12.4±0.4	19.4±0.6
Substitutional Mn density (Mn_{Ga}) (10^{20}cm^{-3})	14.3±0.4	14.3±0.4	19.4±0.6	19.4±0.6
Interstitial Mn density (Mn_I) (10^{20}cm^{-3})	4.1±0.7	0	7±1	0
Actual Total Mn density (10^{20}cm^{-3})	18.4±1	14.3±0.4	26.4±2	19.4±0.6
Effective Mn % (x_{eff})	4.6±0.1%	6.5±0.2%	5.6±0.2%	8.7±0.3%
Substitutional Mn % (x_s)	6.5±0.2%	6.5±0.2%	8.7±0.3%	8.7±0.3%
Interstitial Mn % (x_I)	1.9±0.3%	0%	3.1±0.5%	0%
Actual total Mn%	8.4±0.5%	6.5±0.2%	11.8±0.8%	8.7±0.3%
Hole density (p) (10^{20}cm^{-3})	1.0±0.5	14±0.2	4±1	18±0.5
μ_p at 2K ($cm^2/V\cdot s$)	2.8±1	1.6±0.2	1.9±0.5	2.2±0.1
μ_p at 300K ($cm^2/V\cdot s$)	5.3±3	1.2±0.1	2.4±0.6	1.6±0.1
p/Mn_{eff}	~0.1	~1	~0.3	~0.9
T_C(K)	55±5	165±1	62±5	182±1
The change of hole density before after annealing (δp) (10^{20}cm^{-3})	13±1		14±2	
Hydrogen density(10^{20}cm^{-3})	5±2	~0	~0	~0

Table 3.1 *The magnetic and transport results of H-doped and control samples.*

Nominal Mn%	1.7	2.2	3.4	4.5	5.6	6.72
	As-grown					
Saturation magnetization (emu/cm^{-3})	12.1	17.4	21.9	25.9	32.3	38.0
Mn_{eff} %	1.46%	2.1%	2.65%	3.1%	3.9%	4.6%
Mn_{eff} (10^{20}cm^{-3})	3.3	4.7	5.9	7.0	8.7	10.2
p(10^{20}cm^{-3})	2.8	3.5	3.8	4.3	4.4	4.15
p/Mn_{eff}	0.86	0.75	0.64	0.62	0.51	0.41
Tc(K)	40	54	65	69	79	76
	Annealed					
Saturation magnetization (emu/cm^{-3})	12.3	17.6	22.7	28.7	40.1	46.9
Mn_{eff} %	1.49%	2.13%	2.74%	3.47%	4.85%	5.67%
Mn_{eff} (10^{20}cm^{-3})	3.3	4.8	6.1	7.7	10.8	12.6
p(10^{20}cm^{-3})	3.2	4.7	6.3	7.1	9.8	13.9
p/Mn_{eff}	0.96	0.99	1.03	0.92	0.91	1.1
Tc(K)	42	68	83	100	119	149
Total Mn%	1.52%	2.16%	2.84%	3.81%	5.8%	6.75%
Interstitial Mn%	0.03%	0.03%	0.09%	0.34%	0.95%	1.08%

Table 3.2 *The magnetic and transport results for the samples with varying Mn concentration (shown in the Figure* **3.16**, **3.17***and* **3.18***) measured by Dr. K.Y. Wang* [2] *and Dr. K. Edmonds from Nottingham group.*

References

[1] K. W. Edmonds, P. Bogusławski, K. Y. Wang, R. P. Campion, S. N. Novikov, N. R. S. Farley, B. L. Gallagher, C. T. Foxon, M. Sawicki, T. Dietl, M. Buongiorno Nardelli, and J. Bernholc, Phys. Rev. Lett. **92**, 037201 (2004).

[2] T. Jungwirth, K. Y. Wang, J. Mašek, K. W. Edmonds, J. König, J. Sinova, M. Polini, N. A. Goncharuk, A. H. MacDonald, M. Sawicki, A. W. Rushforth, R. P. Campion, L. X. Zhao, C. T. Foxon, and B. L. Gallagher, Phys. Rev. B **72**, 165204 (2005).

[3] J. Mašek and F. Máca, Phys. Rev. B **69**, 165212 (2003).

[4] J. Mašek, J. Kudrnovský, and F. Máca, Phys. Rev. B **67**, 153203 (2003)

[5] L. X. Zhao, C. R. Staddon, K. Y. Wang, K. W. Edmonds, R. P. Campion, B. L. Gallagher, and C. T. Foxon, Appl. Phys. Lett. **86**, 071902 (2005)

[6] J. Smit, Physica (Amsterdam) **21**, 877 (1955).

[7] L. Berger, Phys. Rev. B **2**, 4559 (1970).

[8] T. Jungwirth, Q. Niu, and A. H. MacDonald, Phys. Rev. Lett. **88**, 207208 (2002).

[9] K. W. Edmonds, R. P. Campion, K. Y. Wang, A. C. Neumann, B. L. Gallagher, C. T. Foxon, and P. C. Main, J. Appl. Phys. **93**, 6787 (2003).

[10] S. Shen, X. Liu, Z. Ge, J. K. Furdyna, M. Dobrowolska, and J. Jaroszynski, J. Appl. Phys. **103**, 07D134 (2008).

[11] M. Glunk, J. Daeubler, W. Schoch, R. Sauer, and W. Limmer, Phys. Rev. B **80**, 125204 S(2009).

[12] T. Fukumura, H. Toyosaki, K. Ueno, M. Nakano, T. Yamasaki, and M. Kawasaki, Jpn. J. Appl. Phys. **46**, pp. L642-L644 (2007).

[13] D. H. Martin, “Magnetism in Solids”, p.20, The MIT Press, Cambridge, Massachusetts, (1967).

[14] V. Novák, K. Olejník, J. Wunderlich, M. Cukr, K. Vyborny, A. W. Rushforth, K. W. Edmonds, R. P. Campion, B. L. Gallagher, J. Sinova, and T. Jungwirth, Phys. Rev. Lett. **101**, 077201 (2008).

[15] D. Ruzmetov, J. Scherschligt, D. V. Baxter, T. Wojtowicz, X. Liu, Y. Sasaki, J. K. Furdyna, K. M. Yu, and W. Walukiewicz, Phys. Rev. B **69**, 155207 (2004).

[16] H. Ohno, J. Magn. Magn. Mater **200**, 110 (1999).

Chapter 4

Suppression of interstitial Mn ion diffusion in (Al,Ga,Mn)As based heterostructures

This chapter demonstrates a method to suppress the diffusion of interstitial Mn ions during low temperature annealing from specific layers in (Al,Ga,Mn)As based heterostructures, which is achieved by growing a region with a deficiency of As. It is proposed that the effect is due to the formation of an electrostatic barrier which opposes the diffusion of interstitial Mn ions. These studies are useful for creating (Al,Ga,Mn)As based heterostructures in which individual layers have tailored magnetic properties.

4.1 The introduction

The dilute magnetic semiconductor (Ga,Mn)As has been the subject of intense research in the field of spintronics [1]. Many of the attractive properties of (Ga,Mn)As arise from the high sensitivity of the magnetic anisotropy and T_C to variations in the alloy concentration [1-9], or to the application of electric fields [10,11] or mechanical strain [12-15]. The sensitivity of the magnetic properties to the alloy composition opens up the possibility to grow heterostructures by MBE where different layers can have a different magnetic anisotropy and/or T_C. Such structures are useful for investigating phenomena such as tunnelling magnetoresistance (TMR) [16], tunnelling anisotropic magnetoresistance (TAMR) [17,18], and spin transfer torque (STT) [19].

The post-growth annealing at temperatures below the growth temperature can enhance T_C of (Ga,Mn)As [20,21], (Al,Ga,Mn)As [3] and (Ga,Mn)(As,P) [4,5] significantly. The application of this technique to heterostructures requires that the interstitial Mn migrate from the buried layers, through any subsequent layers in order to reach the surface of the structure. It was previously shown that both GaAs capping layers [22] and GaAs spacers in trilayer structures [23] inhibit the removal of interstitial Mn, while their passivation is enhanced in thin (Ga,Mn)As layers capped with As [24]. The ability to independently remove the interstitial Mn from specific layers in a heterostructure would increase the range of possible layer combinations with desired magnetic properties that could be grown.

The next section will show that it is possible to suppress the diffusion of interstitial Mn from specific layers in a heterostructure during the low temperature annealing process. This is achieved by growing a thin arsenic deficient layer at the interface between two layers of different composition.

4.2 The MBE growth process for bilayer samples

The structures investigated consist of 7nm to 10nm $(Ga_{0.914}Mn_{0.086})As$ grown on 20nm $(Al_{0.3}Ga_{0.64}Mn_{0.06})As$. These layers were grown on semi-insulating GaAs(001)

substrates with a low temperature GaAs buffer layer. (Figure **4.1**) The transition from the $(Al_{0.3}Ga_{0.64}Mn_{0.06})As$ layer to the $(Ga_{0.914}Mn_{0.086})As$ layer was made by shutting off the Al flux while keeping the Ga and Mn fluxes constant. Hence, the nominal Mn percentage increases to 8.6%. To maintain the correct III-V stoichiometry the As pressure must also be reduced. The As pressure responds slowly over a period of several seconds to a reduction in the setting of the As valve, it was necessary to reduce the As valve shortly before shutting off the Al flux to ensure the correct stoichiometry when the Al flux was shut off. By reducing the As sooner than was necessary, it was possible to grow a region of the $(Al_{0.3}Ga_{0.64}Mn_{0.06})As$ layer, of order a few nm thickness, that was deficient in As. The parameter δ is defined as the distance below the interface at which the As valve was reduced and the value can be calculated by multiplying the growth rate by the length of time from when the As flux started to reduce till the Al flux was shut off. A range of structures for which δ was varied from 3nm to -3nm have been investigated (the negative value indicates that the As valve was reduced after the Al flux was shut off, resulting in an excess As flux during initial growth of (Ga,Mn)As layer).

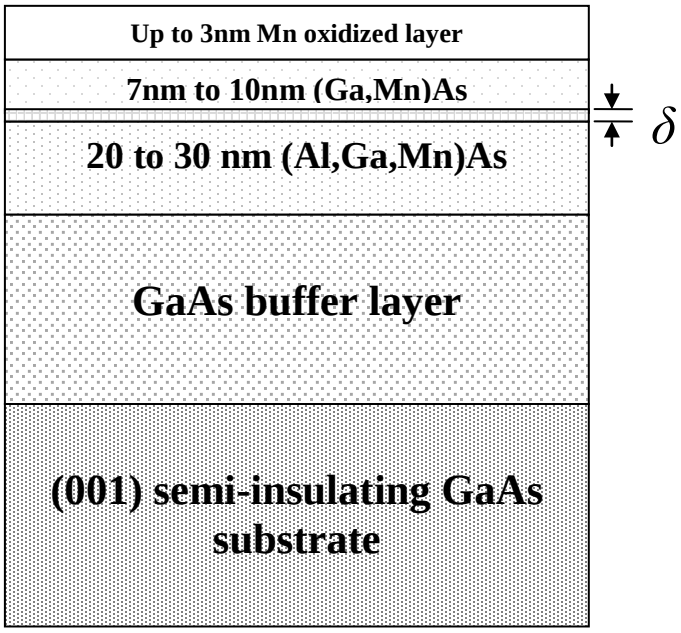

Figure 4.1 *The layer structure of (Ga,Mn)As/(Al.Ga,Mn)As bilayer. The top of the sample can be oxidized after being taken out from MBE system.*

4.3 Magnetometry study of the bilayer samples

The samples were characterized by measuring the magnetic properties along high symmetry crystal directions using the SQUID magnetometer.

4.3.1 Single layer of (Ga,Mn)As and (Al,Ga,Mn)As

Figures **4.2** and Figure **4.3** show the projection of the temperature dependent remnant moment, measured after cooling in a saturating field of 1000 Oe, for two control samples consisting of 25nm $(Al_{0.3}Ga_{0.64}Mn_{0.06})As$ and 7nm $(Ga_{0.94}Mn_{0.06})As$, respectively, grown on GaAs(001) substrates with (Al,Ga)As buffer layers. Qualitatively similar magnetic properties, like magnetic anisotropy, can be observed for (Ga,Mn)As layers with nominal Mn percentages from 2.2% to 9%. [25,26] The top film of bilayer samples should have similar properties to the nominal 6% (Ga,Mn)As control sample. The samples were measured as-grown and after annealing in air at 180°C for 48 hours. For both samples the low temperature annealing results in an increase of T_C and a modification of the magnetic anisotropy. For the $(Al_{0.3}Ga_{0.64}Mn_{0.06})As$ sample, the easy axis points out of the plane for the as-grown sample, possibly due to a strong localization of carriers due to the addition of Al. [3] After annealing the easy axis points in the plane, predominantly along the [1-10] direction over most of the temperature range. For the $(Ga_{0.94}Mn_{0.06})As$ sample, the magnetic anisotropy consists of a cubic component favoring easy axes along the [100] and [010] directions and a uniaxial component favoring the [1-10] direction. In common with most studied (Ga,Mn)As layers [25] , a spin reorientation transition is observed in the as-grown layer, with the cubic anisotropy dominating at low temperatures and the uniaxial anisotropy dominating at higher temperatures. After annealing the uniaxial anisotropy tends to dominate over the whole temperature range.

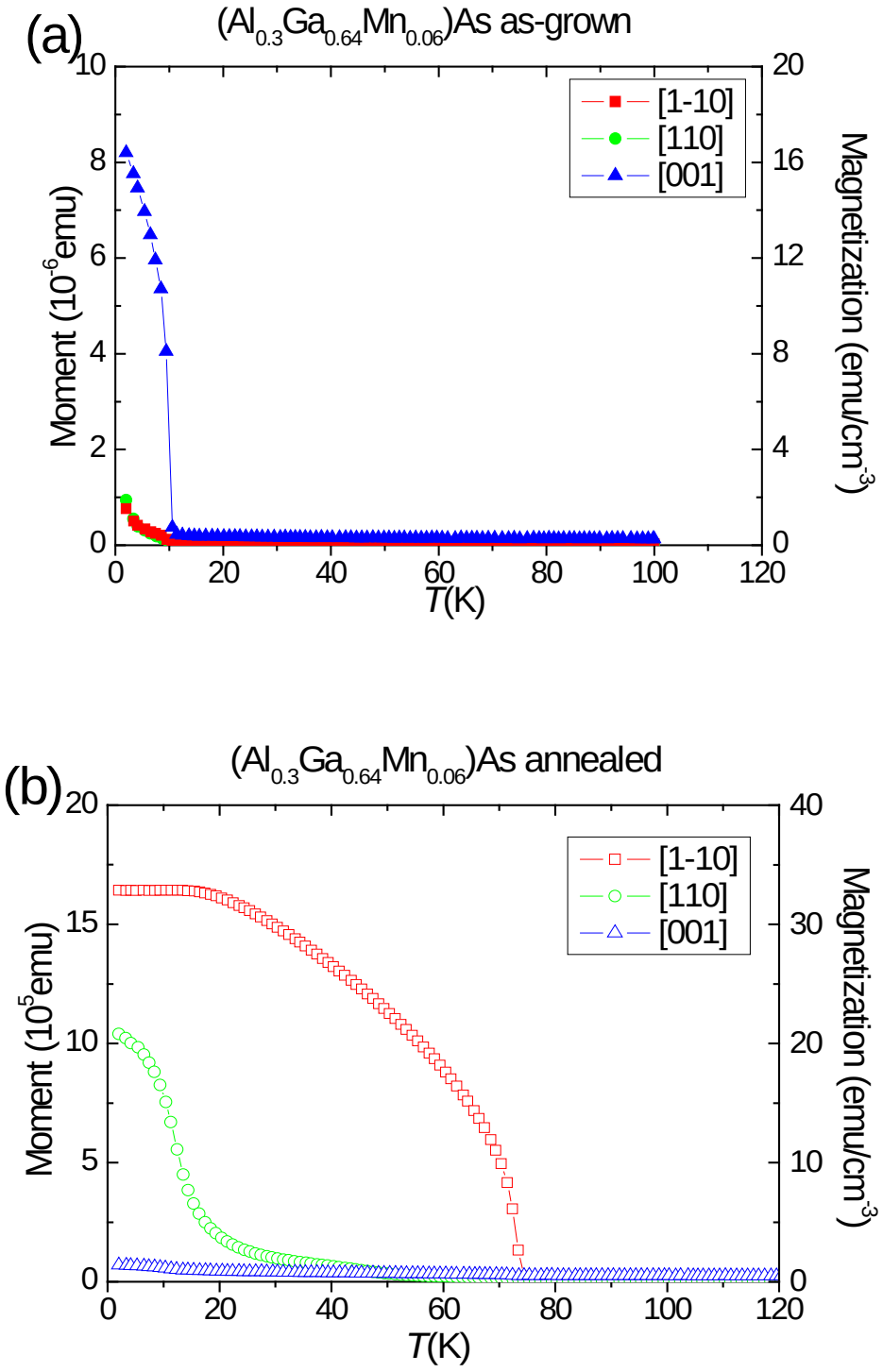

Figure 4.2 *Projection of the temperature dependent remnant moment and magnetization after 1000 Oe field cool for a 25nm ($Al_{0.3}Ga_{0.64}Mn_{0.06}$)As control sample in (a) as grown and (b) annealed states.*

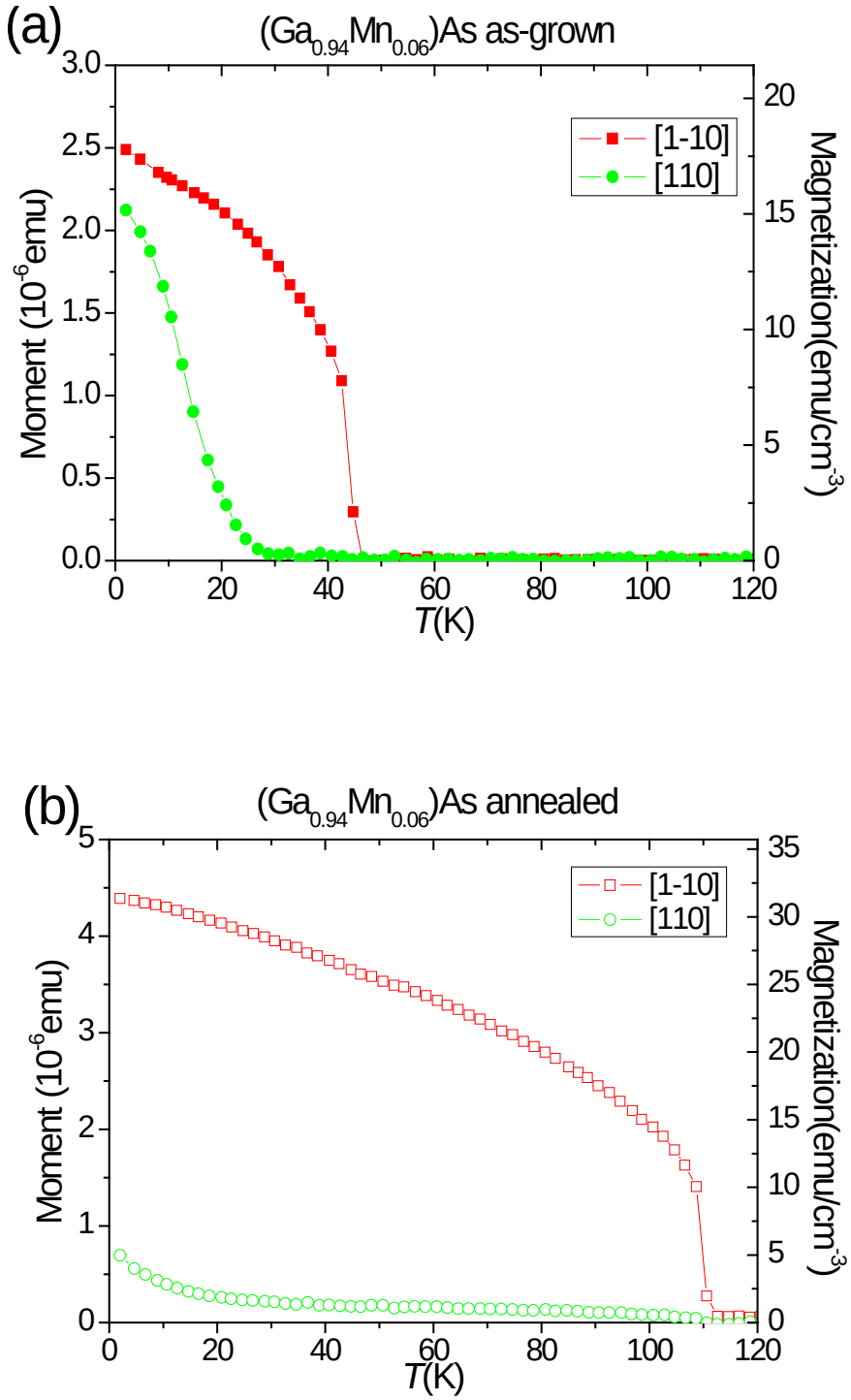

Figure 4.3 *Projection of the temperature dependent remnant moment and magnetization after 1000 Oe field cool for a 7nm ($Ga_{0.94}Mn_{0.06}$)As control sample in (a) as grown and (b) annealed states.*

4.3.2 Bilayer with suppression of interstitial Mn diffusion

Figure **4.4** shows the projection of the temperature dependent remnant moment measured for a bilayer sample S1 with δ =3nm. In the as-grown state there is a significant moment in the out of plane [001] direction at the lowest temperature. This component disappears above 5K. There is also a component of the magnetization along the [110] direction that persists up to 49K. After annealing the component of the magnetization along the [001] direction remains, gets stronger in magnitude and persists up to 17K. The component of the magnetization along the [110] persists up to 96K. The low temperature magnetization component along the [001] direction is attributed to the bottom $(Al_{0.3}Ga_{0.64}Mn_{0.06})As$ layer and the in-plane magnetization component is attributed to the top $(Ga_{0.914}Mn_{0.086})As$ layer. The effects of annealing are significantly suppressed for the bottom $(Al_{0.3}Ga_{0.64}Mn_{0.06})As$ layer, when compared to the control sample (Figure **4.2**). This interpretation is confirmed by the etching study described below. The fact that the uniaxial easy axis of the $(Ga_{0.914}Mn_{0.086})As$ layer lies along the [110] direction is in contrast to the behavior of the control sample as well as of most $(Ga_{1-x}Mn_x)As$ films with x >0.02, for which the easy direction is typically [1-10] [2]. Although the origin of the uniaxial component of the anisotropy is uncertain, it has been suggested that it arises due to the direction of As bonds at the growth surface [27]. If this is the case, then it may be that growing with a significant deficiency of As at the interface affects the surface reconstruction in such a way that the [110] becomes the preferred easy axis direction. This behavior is also observed in $Co_{50}Fe_{50}$ grown on the n type GaAs. [28]

S1

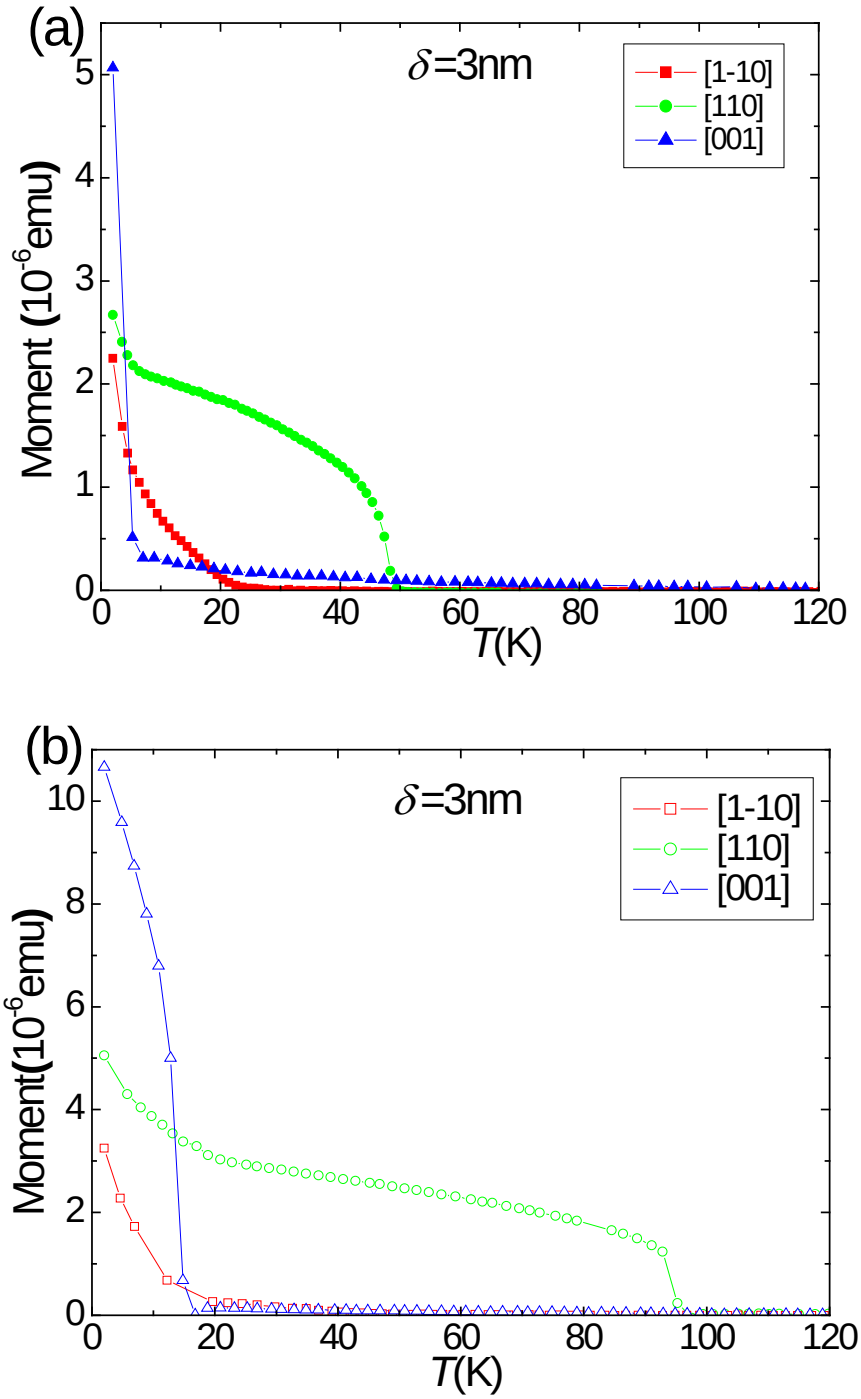

Figure 4.4 *Projection of the temperature dependent remnant moment after 1000 Oe field cool for bilayer sample S1 (δ =3nm) in the (a) as grown state and (b) after annealing.*

4.3.3 Etching off the top layer

To further investigate the effects of annealing on each layer, magnetometry measurements have been performed after etching the top surface and annealing the sample again. The etchant is 30% HCl, which is known to remove the top ≈1nm of oxidized material after 30s etching. [29] The sample was annealed at 180ºC for 10 to 15 hours each time after etching. Figures **4.5** shows that the effect of successive etching and annealing steps is to reduce the moment and T_C associated with the component of the magnetization along the [110] direction. This confirms that this component is from the top $(Ga_{0.914}Mn_{0.086})As$ layer and also indicates an inhomogeneous concentration of magnetic moments through the thickness of that layer. It is striking that the component of the magnetization along the [001] direction remains unaltered by the successive etching and annealing treatments. This remains the case until 6 etching and annealing steps have been performed and the magnetization along the [110] direction has almost vanished. (Figure **4.6**(e)) Upon subsequent annealing treatments the magnetization component along the [001] direction reduces and a component along the [1-10] direction emerges with an increased T_C (Figure **4.5**(f)). This final trend is similar to that observed upon annealing the $(Al_{0.3}Ga_{0.64}Mn_{0.06})As$ control sample. From these observations it can be concluded that the diffusion of interstitial Mn from the bottom $(Al_{0.3}Ga_{0.64}Mn_{0.06})As$ layer is strongly suppressed until the top $(Ga_{0.914}Mn_{0.086})As$ layer is completely removed and the $(Al_{0.3}Ga_{0.64}Mn_{0.06})As$ layer . The top $(Ga_{0.914}Mn_{0.086})As$ layer and the As deficient region in the top few nm of the $(Al_{0.3}Ga_{0.64}Mn_{0.06})As$ layer are the likely causes of this effect. The next section will discuss which one is the real cause of this effect.

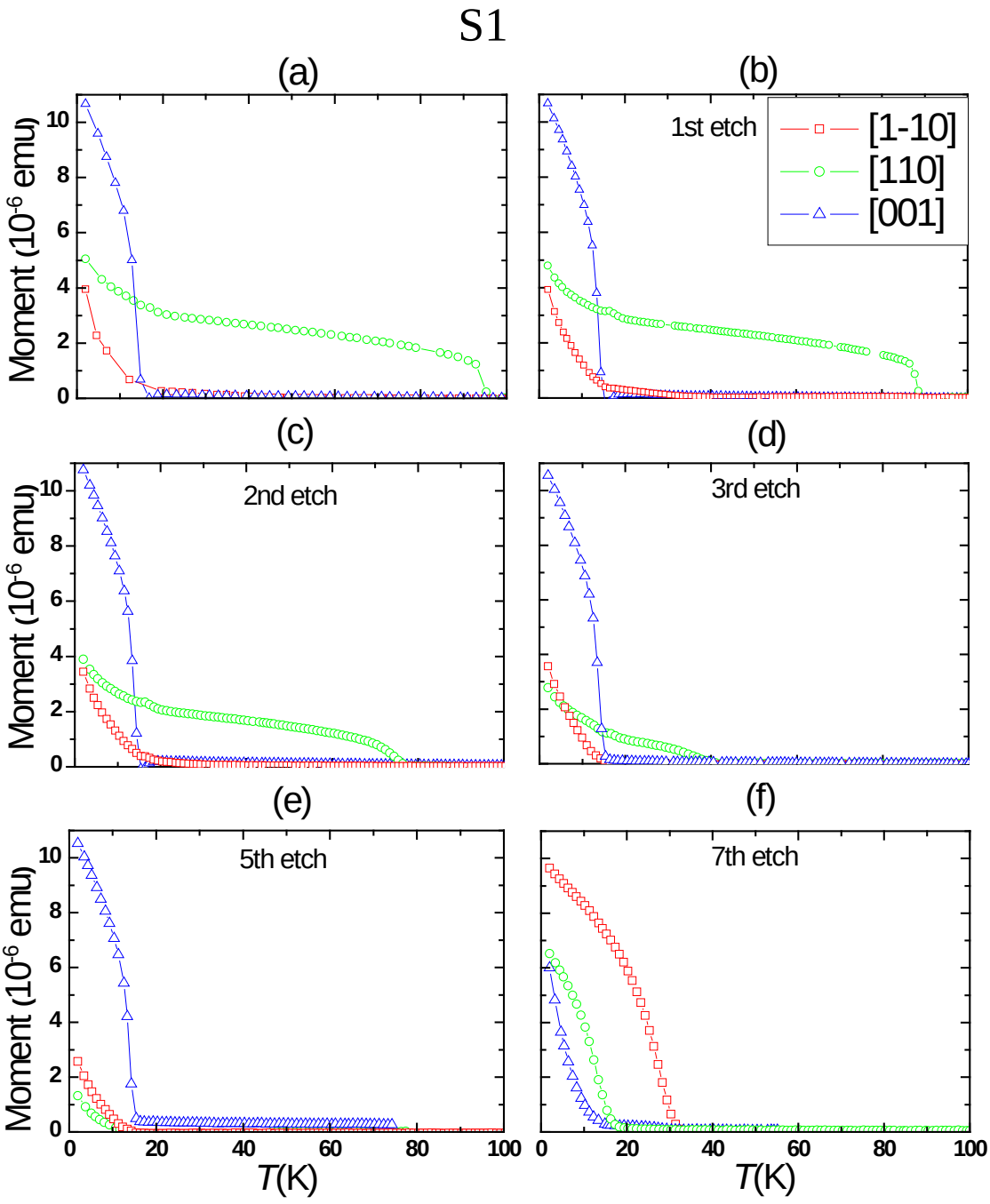

Figure 4.5 *Projection of the temperature dependent remnant moment after 1000 Oe field cool for bilayer sample S1 (δ =3nm) after 1st, 2nd, 3rd, 5th, 7th etch and anneal steps.*

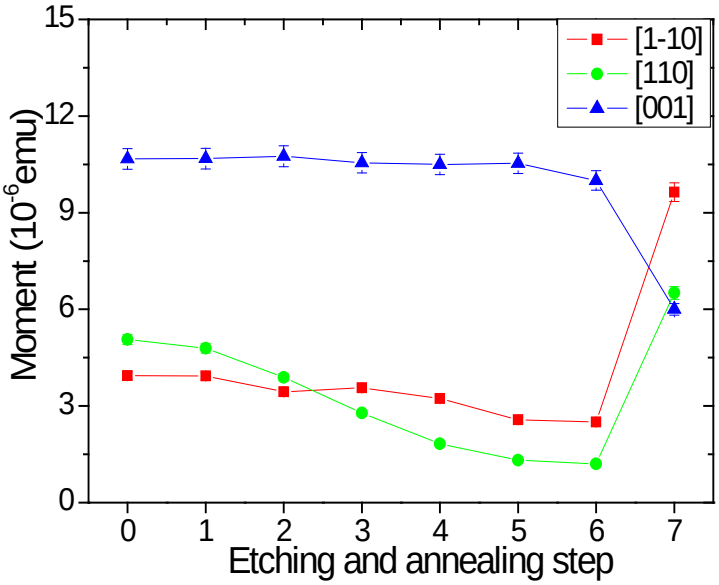

Figure 4.6 *Projection of the remnant moment at 2K along three different crystal directions vs. each etching and annealing step for sample S1.*

4.3.4 Bilayer without suppression of interstitial Mn diffusion

Compared to the previous results of sample S1 with δ =3nm, Figure **4.7** shows the projection of remnant moment measured before and after annealing for a bilayer sample S2 with δ =1nm. Before annealing the curve was very similar to that observed for sample 1 (δ =3nm), For the bottom $(Al_{0.3}Ga_{0.64}Mn_{0.06})As$ layer T_C=4K and there is a perpendicular magnetic easy axis. For the top $(Ga_{0.914}Mn_{0.086})As$ layer T_C=36K but the easy axis for the top layer is along the [1-10] direction (Figure **4.7** (a)). However, after annealing there are clear differences between the two samples. For sample S2 the component of the magnetization along the [001] direction diminishes upon annealing and the component along the [1-10] direction shows two clear transitions as a function of temperature. (Figure **4.7**(b)) The first transition occurs at 37K and the second at 93K. This behavior can be explained on the basis that the interstitial Mn ions are removed from both of the layers in the heterostructure during the annealing. The first transition corresponds to T_C of the bottom $(Al_{0.3}Ga_{0.64}Mn_{0.06})As$ layer and the second transition corresponds to T_C of the top $(Ga_{0.94}Mn_{0.06})As$ layer. Both of the layers now have the in-plane magnetic easy axis. The top one has a uniaxial easy axis along [1-10] and the bottom layer has the biaxial anisotropy with [100]/[010] easy axes, which are similar to the samples of (Ga,Mn)As and (Al,Ga,Mn)As single layers.

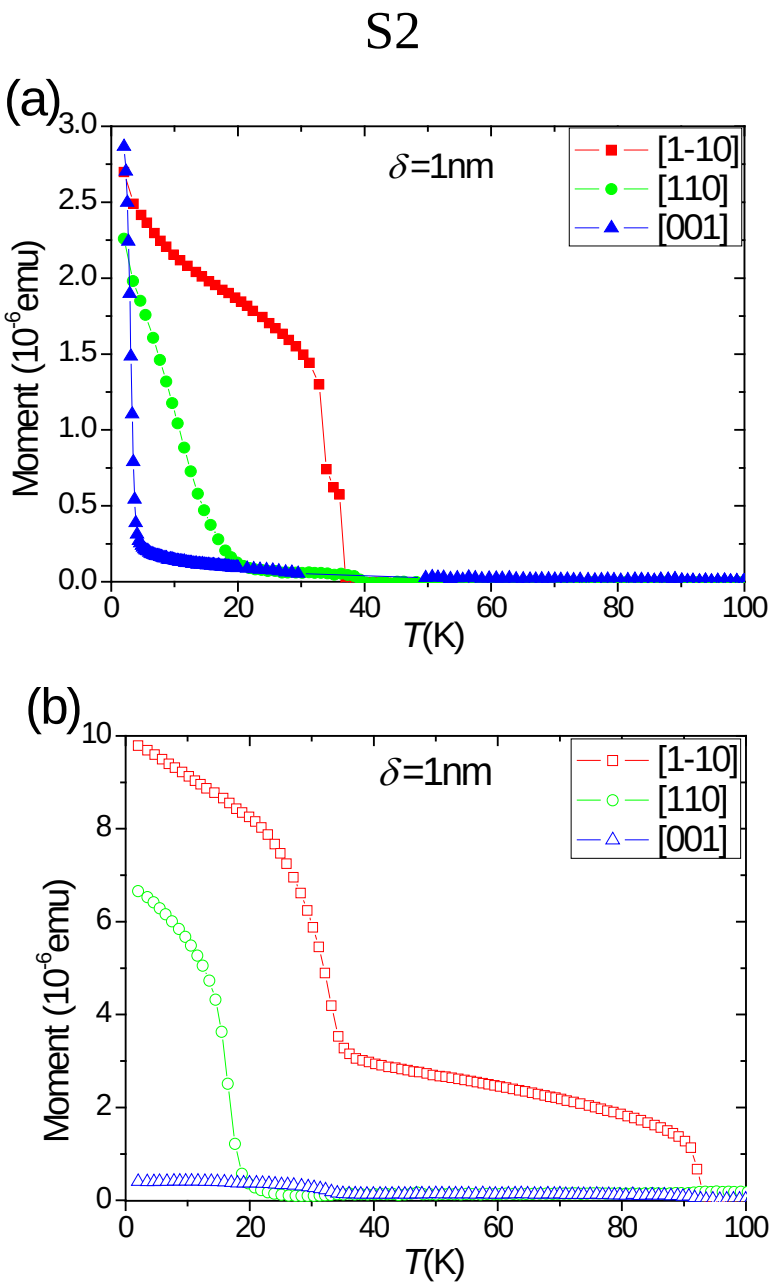

Figure 4.7 *Projection of the temperature dependent remnant moment after 1000 Oe field cool for bilayer sample S2 (δ =1nm) (a) as-grown and (b) after annealing at 180°C for 48 hours.*

The magnetometry results of sample S1 and S2 indicate the top (Ga,Mn)As layer cannot be the cause of suppression of diffusion of interstitial Mn. By controlling the growth conditions of the interface between two layers, two different types of bilayer samples for which the bottom layers have different annealing behavior can be achieved. The discussion in the next section will prove the two different growth schedules are repeatable, and two different magnetic switching behaviors can be observed by utilizing the magnetic hysteresis loop measurements.

4.3.5 Study of second pair bilayer samples

In order to prove the bilayer samples with different annealing behaviors are reproducible, another pair of bilayer samples (sample S3 and S4) with 10nm $(Ga_{0.914}Mn_{0.086})As$ layers on 20nm $(Al_{0.3}Ga_{0.64}Mn_{0.06})As$ layers have been grown by MBE. For these samples the arsenic valve was reduced before or after the Al flux was shut off during the growth. Defined in the section 4.2, the parameter δ is 3nm and -3nm for the sample S3 and S4, respectively.

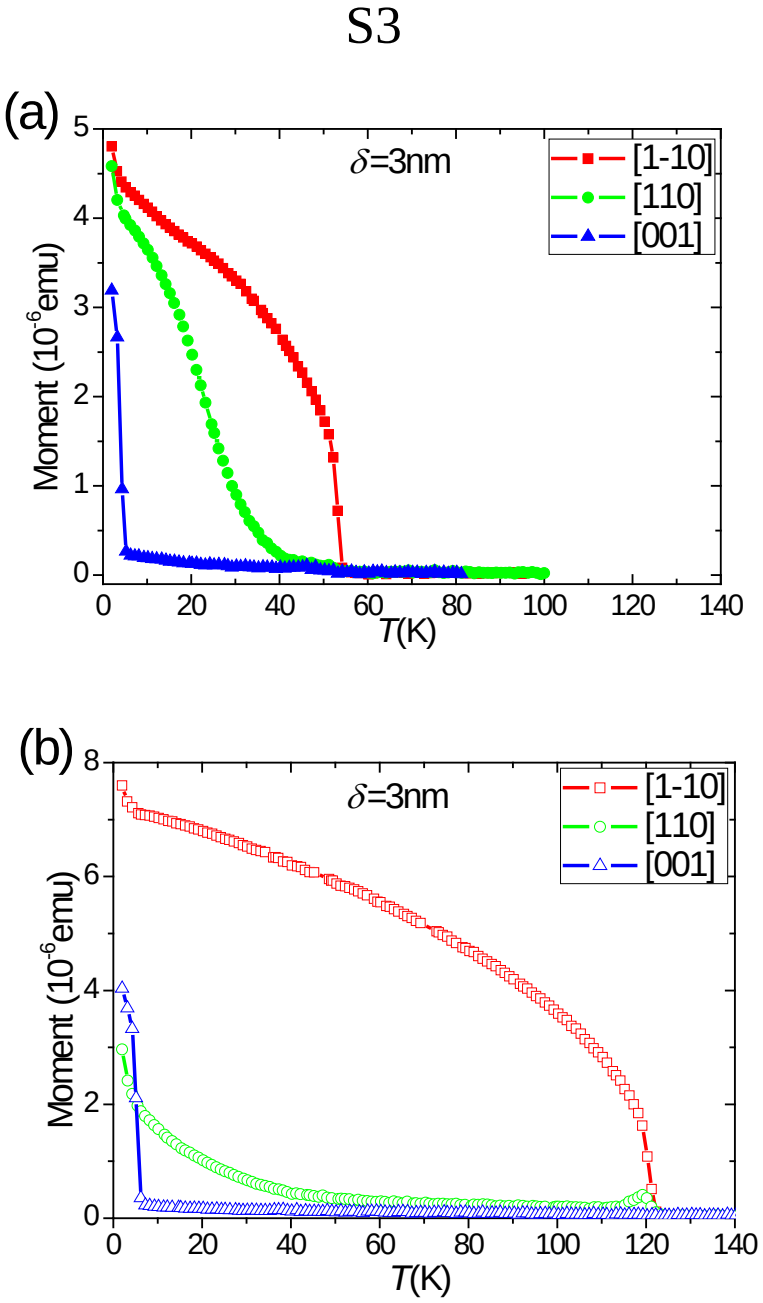

Figure 4.8 *Projection of the temperature dependent remnant moment after 1000 Oe field cool for bilayer sample S3 (δ =3nm) in the (a) as grown state and (b) after annealing.*

Figure **4.8**(a) and **4.9**(a) show the projection remnant moment of the as-grown state of the two samples after 1000 Oe field cooling process. The bottom layer of sample S3 has T_C around 5K with perpendicular magnetic easy axis, and T_C of the top layer is around 54K with in-plane easy axis. The magnetic easy axis of the top $(Ga_{0.914}Mn_{0.086})As$ layer is [1-10] direction, which is different compared to the sample 1 but is the same as the control sample 7nm $(Ga_{0.94}Mn_{0.06})As$ single layer. The magnetic properties of sample S4 are quite similar to sample S3; the only difference is T_C is slightly lower, about 3K for the bottom layer and 45K for the top.

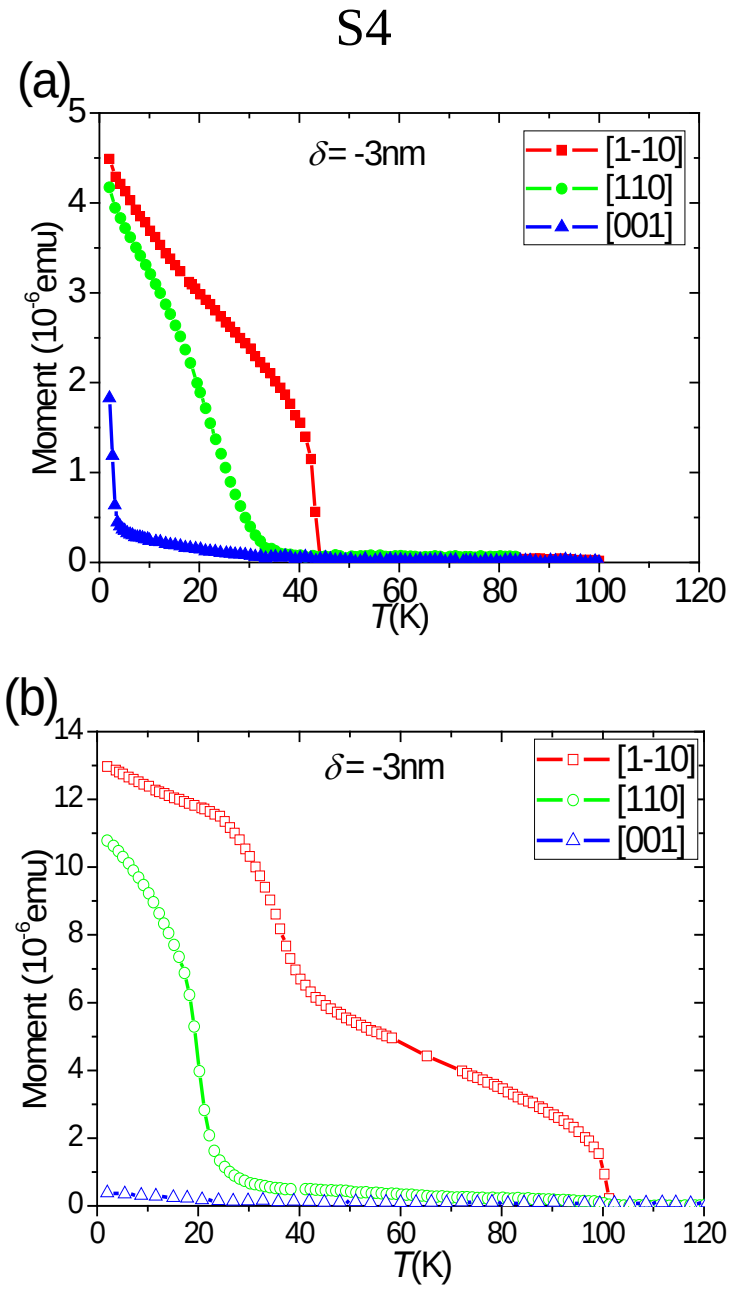

Figure 4.9 *Projection of the temperature dependent remnant moment after 1000 Oe field cool for bilayer sample S4 (δ= -3nm) in the (a) as grown state and (b) after annealing.*

After 48 hours standard annealing at 180^{o}C, the remarkable difference can be observed between two samples, which confirms that the results from the previous two samples are reproducible. Figure **4.8**(b) shows the data of sample S3, for which the diffusion of interstitial Mn ions has been suppressed. T_C of the bottom layer only changes by 1K while the perpendicular magnetic easy axis is retained. The top layer's T_C increases to 120K with the [1-10] direction as the magnetic easy axis. The magnetic hysteresis loops have been measured along three crystal directions [1-10], [110] and [001] at 2K, 20K and 40K with the external magnetic field up to 1T. (Figure **4.10**) It is clear that there are two independent layers with different magnetic easy axes at 2K and this behavior disappears at 20K and 40K when the $(Al_{0.3}Ga_{0.64}Mn_{0.06})As$ layer changes from ferromagnetic to paramagnetic. Figure **4.10**(a) is the magnetic hysteresis loop measured with external magnetic field along [1-10] direction (the magnetic easy axis for (Ga,Mn)As layer). Only 100 Oe could switch the magnetization direction of (Ga,Mn)As, while it needs more than 5000 Oe to saturate the magnetization of (Al,Ga,Mn)As from out of plane to in-plane. Figure **4.10**(b) plots the data of measurement with field applied perpendicularly. ([001] direction - the magnetic easy axis for (Al,Ga,Mn)As layer) It shows 350 Oe field is high enough to switch magnetization of (Al,Ga,Mn)As from negative to positive, while up to 5000 Oe is needed to saturate the magnetization of (Ga,Mn)As from in-plane to out of plane. Figure **4.10**(c) shows [110] direction is the hard axis for both layers, and relatively lower magnetic field is needed for the top layer than for the bottom layer to rotate the magnetization from easy axis to this direction. The results indicate the magnetizations of two layers point to different directions at zero field and change independently without coupling when sweeping external magnetic field.

For sample S4 (Figure **4.9**(b)), T_C of the bottom layer improved from 3K to 40K upon annealing and the easy axis rotates from out of plane to in-plane. T_C for the top layer is around 101K which is still a bit lower compare to sample S3. The reason could be that the excess arsenic flux during the growth of the $(Ga_{0.914}Mn_{0.086})As$ layer reduces T_C. [30] The hysteresis loops (Figure **4.11**) along [1-10] direction at 2K, 17.5K, 30K and 50K shows clearly that the magnetic easy axes for two layers are both in-plane but not parallel with each other which corresponds to the remnant moment data. Without switching independently, the magnetizations of two layers seem to behave as though they are parallel coupled.

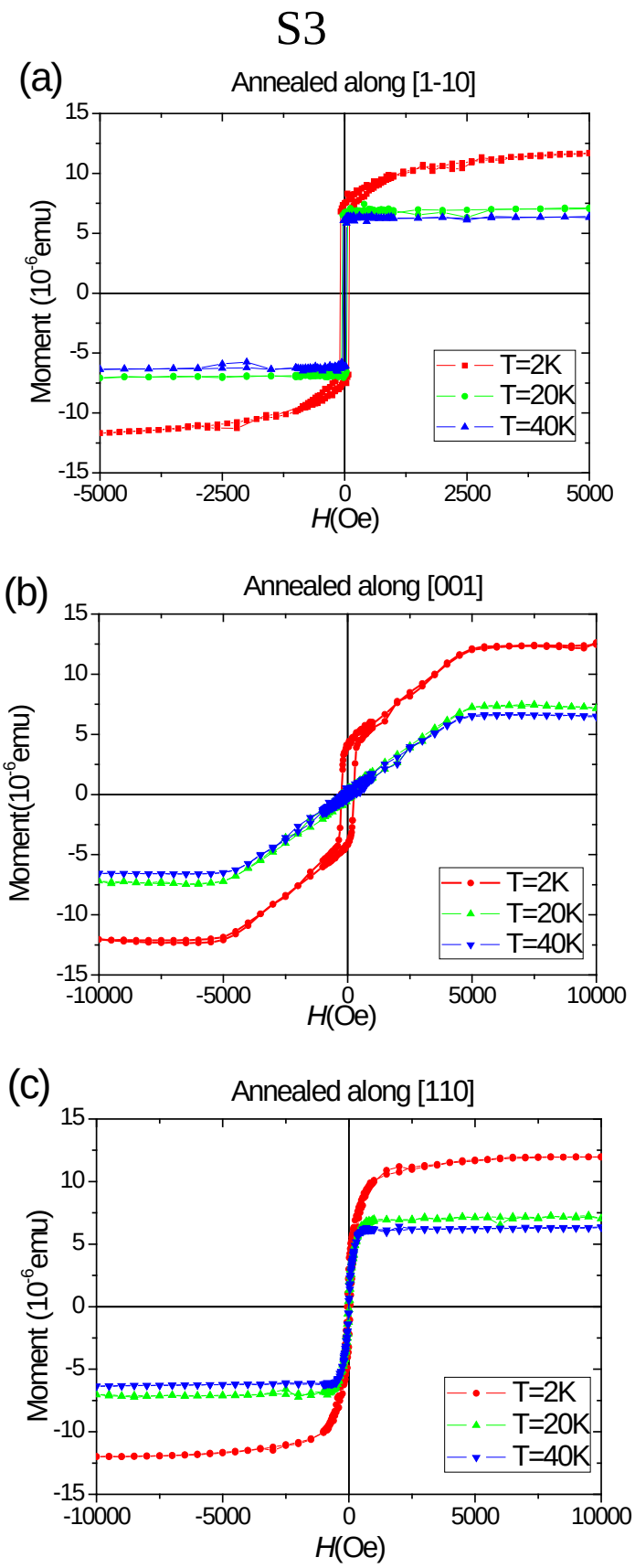

Figure 4.10 *The magnetic hysteresis loop for bilayer sample S3 (δ =3nm) measured at 2K, 20K and 40K, along (a) in-plane [1-10], (b) perpendicular [001] and (c) in-plane [110] directions respectively.*

S4

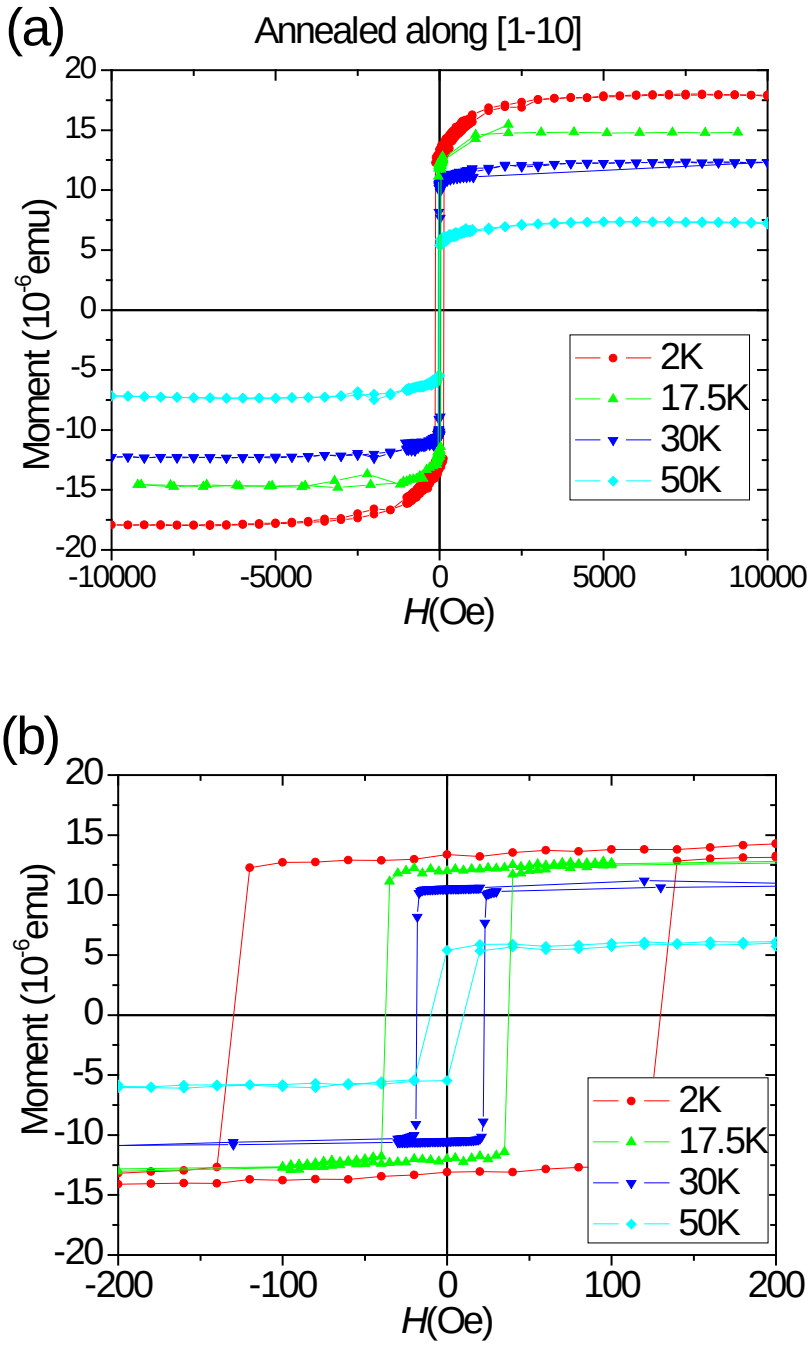

Figure 4.11 *The magnetic hysteresis loop for bilayer sample S4 (δ =-3nm) measured along [1-10] direction at 2K, 17.5K, 30K and 50K respectively.*

4.3.6 Summary of magnetometry studies

Table **4.1** summarizes T_C of the separate layers of each sample before and after annealing. Although the magnetic properties of all the as-grown samples are similar, the magnetic properties after annealing show that they can be separated into two different groups. For three samples with δ > ~2nm, the slight changes of T_C and magnetic easy axis for (Al,Ga,Mn)As indicate there is a tiny annealing effect on bottom layer. Like the as-grown samples, the top and bottom layers of these annealed samples still have different magnetic easy axes perpendicular to each other. It can be observed that the magnetizations of two ferromagnetic layers rotate independently without coupling when applying external magnetic field in-plane and out of plane. Different from other magnetic semiconductor and metal heterostructures [16-19], there is no nonmagnetic barrier between two ferromagnetic layers and a vertical magnetic domain wall close to the interface is expected. On the other hand, three samples with δ < ~2nm have very different magnetic behaviors. After annealing, the T_C of bottom layers increase to around 40K with magnetic easy axes turn to in-plane. The results of magnetic hysteresis loops show that there is a parallel magnetic coupling between the two layers.

Sample No.			S4	S2	S6	S5	S1	S3
δ(nm) from the growth time			-3	1	1-2	2	3	3
(Ga,Mn)As	As-grown	T_C(K)	44	37	42	51	49	54
		anisotropy	[100]	[100]	[100]	[100]	[100]	[100]
			Turns to[1-10] as T increases				Turns to [110]	
	Annealed	T_C(K)	101	93	110	92	96	122
		anisotropy	[1-10]	[1-10]	[1-10]	[1-10]	[110]	[110]
(Al,Ga,Mn) As	As-grown	T_C(K)	3	4	3	3	5	5
		anisotropy	[001]	[001]	[001]	[001]	[001]	[001]
	Annealed	T_C(K)	40	36	44	10	17	6
		anisotropy	biaxial	biaxial	biaxial	[001]	[001]	[001]

Table 4.1 *The table shows T_C and magnetic anisotropy at 2K of the individual layers determined for 6 samples before and after annealing.*

Figure **4.12** shows T_C of the bottom $(Al_{0.3}Ga_{0.64}Mn_{0.06})As$ layer as a function of δ. It indicates that a value of δ > ~2nm results in a lower T_C of the bottom layer. In order to characterize the influence of δ on the structure of the buried interface, x-ray reflectivity measurements have been performed.

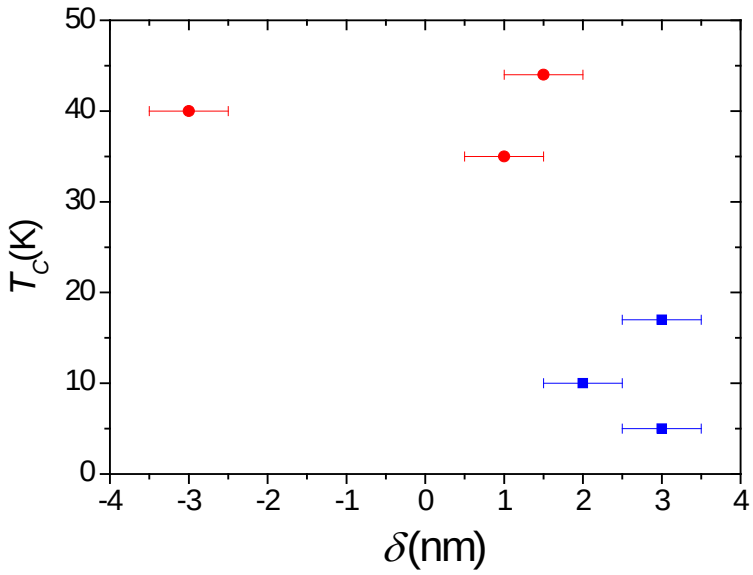

Figure 4.12 *T_C of the bottom $(Al_{0.3}Ga_{0.64}Mn_{0.06})As$ layer for 6 annealed samples shown as a function of δ. T_C was determined as the temperature at which the moment along the [001] direction falls to zero (blue squares) or the temperature of the first transition in the [1-10] direction (red circles).*

4.4 X-ray reflectivity (XRR) measurement

4.4.1 Introduction to XRR

XRR is a non-destructive and non-contact technique for thickness determination between 1-200 nm with a precision of about 1-3Å. In addition, this technique is employed for the determination of the density and roughness of films and multi-layers with a high precision.

The XRR method involves monitoring the intensity of x-ray beam reflected by a sample at incident angles. A monochromatic x-ray beam of wavelength λ =1.54Å irradiates a sample at an incident angle ω and the reflected intensity at an angle 2θ is recorded by a detector in the Bragg-Brentano geometry. (Figure **4.13**) Because 2θ

always equals to 2ω in reflectivity measurement, θ is used to replace ω in the rest of this chapter. The reflection at the surface and interfaces is due to the different electron densities in the different layers, which corresponds to different reflective indices in the classical optics. Total external reflection occurs for incident angles θ below the critical angle θ_C. When θ above θ_C, the reflection from the different interfaces interferes and gives rise to interference fringes. The density of the material at the top surface can be obtained from θ_C. The thickness of each layer determines the period of the interference fringes. The surface and interface-roughness gives rise to diffuse scattering, resulting in a more rapidly reduced intensity in the specularly reflected beam with increasing 2θ.

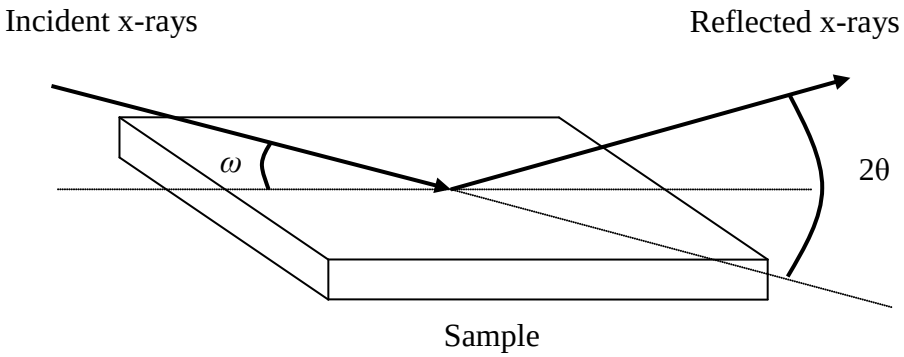

Figure 4.13 *Geometry used in XRR measurements*

4.4.2 The analysis of XRR results

The XRR measurements were carried out in X'Pert Materials Research Diffractometer (MRD) system. The technical details of the equipment will be presented in the Appendix B. Six samples have been measured before and after annealing, with the range of incident angle θ between 0.25° and 3°. Figure **4.14** shows the XRR specular scan data of samples S1 and S2 as examples.

The data is simulated by using X'Pert Reflectivity (Version 1.1) from PANalytical. It is assumed that the sample contains five layers: the bottom layer is GaAs substrate + buffer layer, the top is a few nanometer oxidized surface, between them are the (Al,Ga,Mn)As layer, As deficient (Al,Ga,Mn)As layer and (Ga,Mn)As layer. (See Figure **4.1** of layer structure) Each layer has different parameters of material density, layer thickness and surface or interface-roughness, which means there are 15

parameters for the simulation. It is preferable to reduce the number of parameters for this multi-parameter simulation. Because the substrate (buffer layer) is high quality GaAs single crystal, all the parameters of this layer can be fixed to constant values. Due to the high quality epitaxy growth, it should have a smooth interface between the As normal and As deficient (Al,Ga,Mn)As layer, which means the roughness of this interface should be close to zero. This has been proved by the simulation results which show the values of roughness are less than 0.1nm (within the precision of XRR measurement) for all the samples.

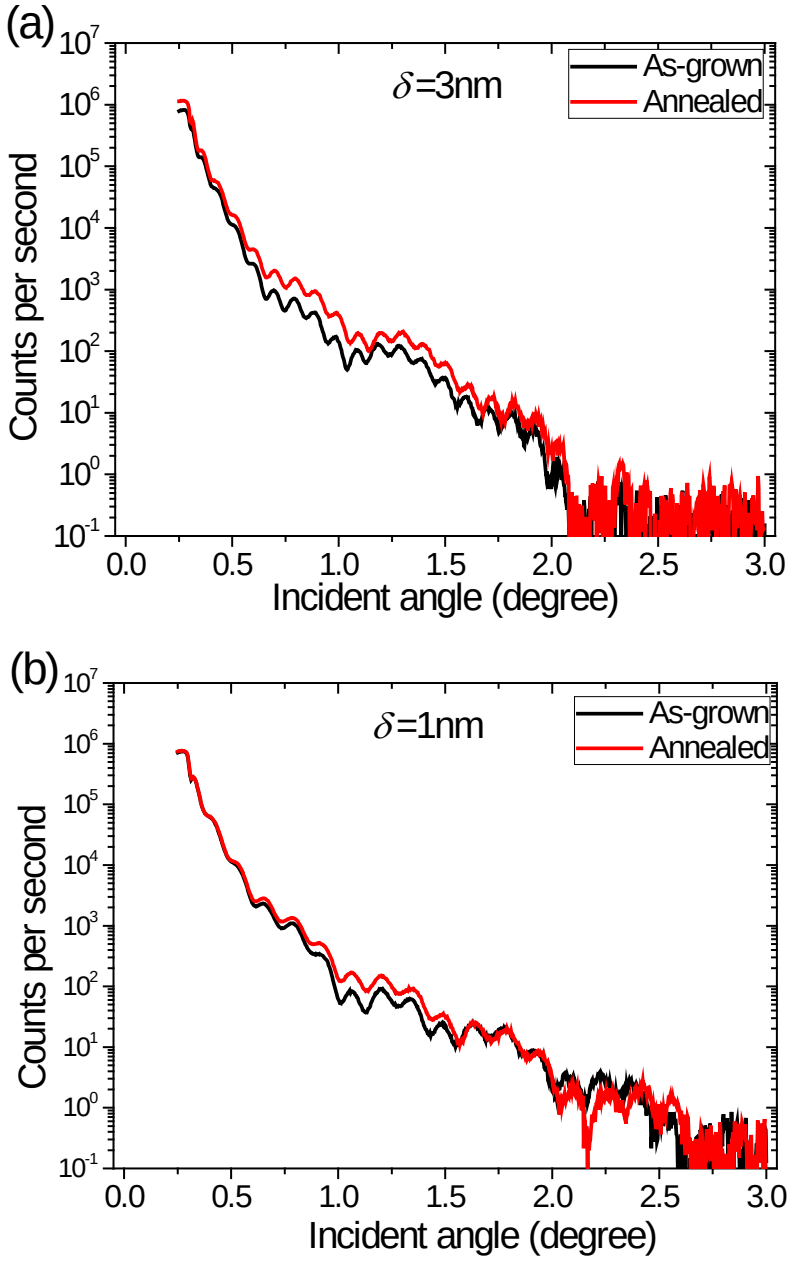

Figure 4.14 *XRR specular scan data of the sample (a) S1 with δ =3nm and (b) S2 with δ =1nm*

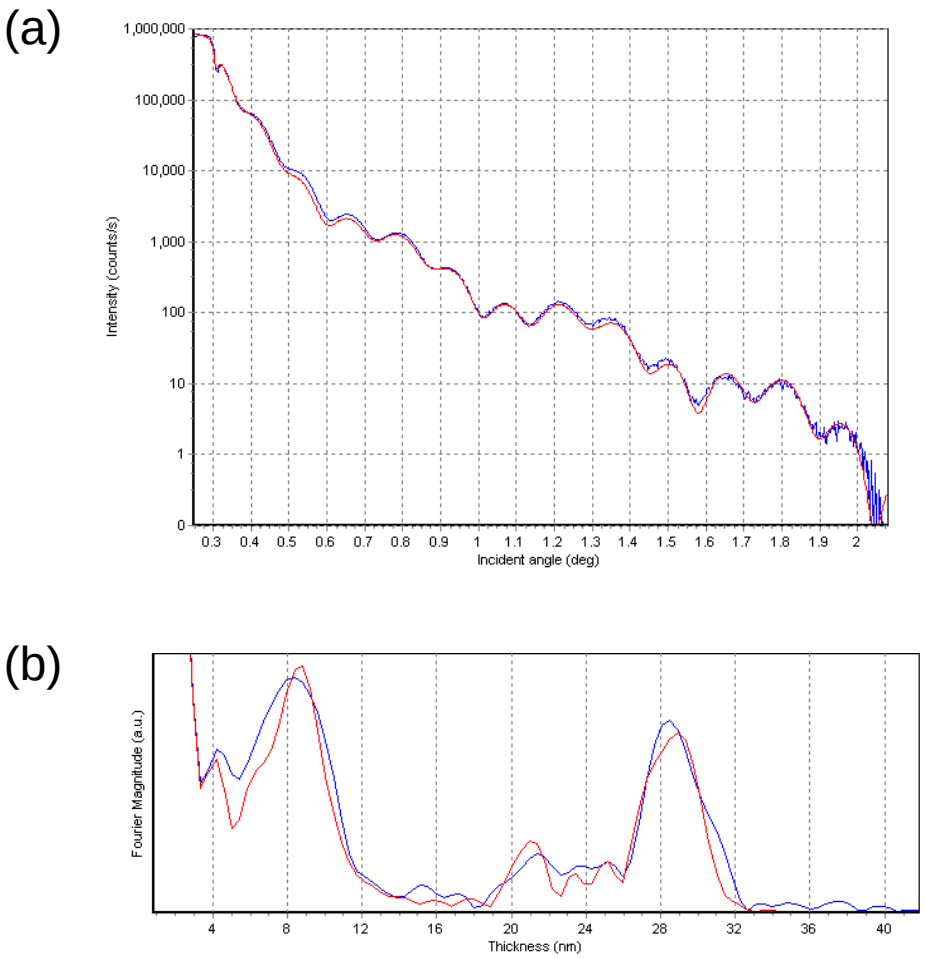

Figure 4.15 *(a) the simulation result of XRR specular scan (red curve) with the experimental curve (blue line) (b) the thickness analysis of the sample S2 (annealed), 8nm peak represents the thickness of the top layer and 28nm is the sum of top layer 8nm and 20nm which is the thickness of bottom layer.*

Figure **4.15** presents the simulated curve with the experimental result including the thickness analysis (use the Fourier transform to get the layer thickness) for annealed sample S2. All the simulation show similarly good fitting for most of samples except sample S4 with δ =-3nm. The reason could be that it contains As excess (Ga,Mn)As layer which has a more complicated structure than other samples. However, some important results still can be observed for the remaining 5 samples. (Table **4.2**) Compared with the magnetometry data shown in Table **4.1**, there is a clear trend between interface-roughness (the roughness of interface between (Ga,Mn)As and (Al,Ga,Mn)As layers) and T_C of bottom layer for the annealed samples, (Figure **4.16**(a)) which suggests interface-roughness has a relation with the suppression of interstitial Mn diffusion from bottom layer.

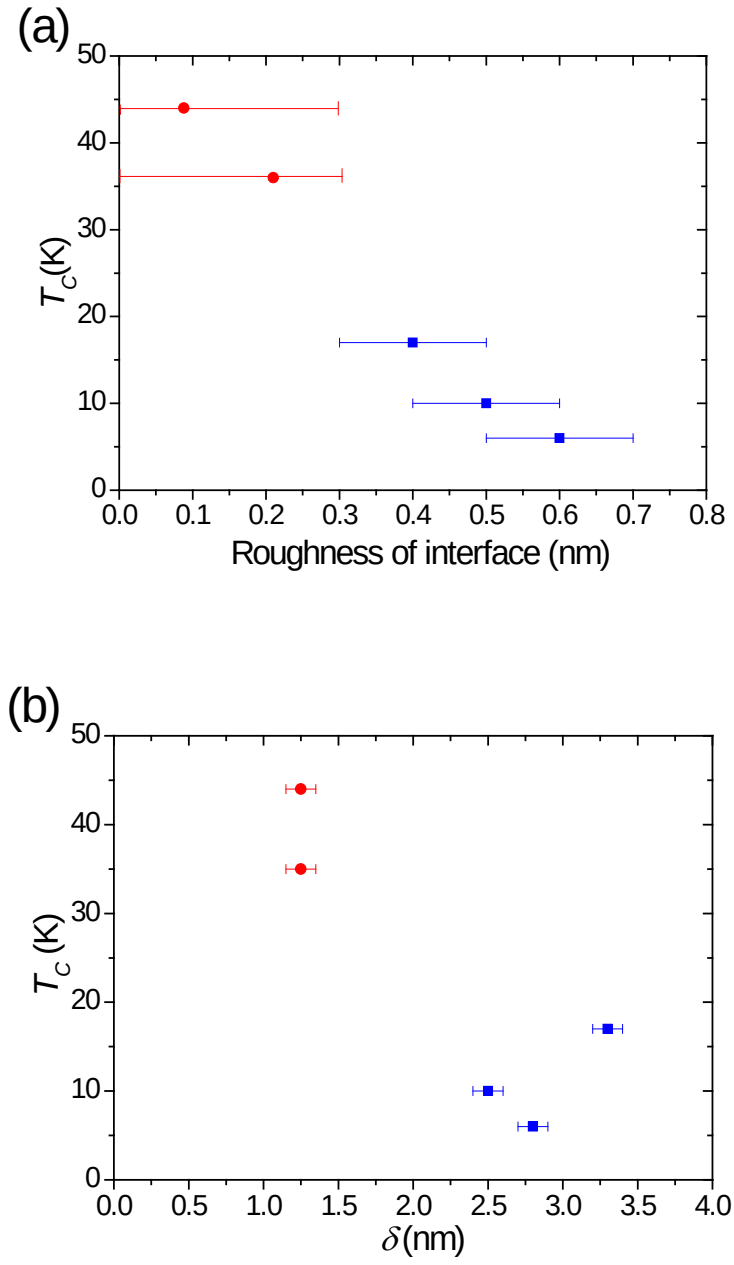

Figure 4.16 *T_C of the bottom ($Al_{0.3}Ga_{0.64}Mn_{0.06}$)As layer for 5 annealed samples shown as a function of (a) interface-roughness between (Ga,Mn)As and As deficient (Al,Ga,Mn)As layers, (b) δ (the thickness of As deficient region) from XRR measurements. T_C was determined in the same way as said in Figure* **4.12**

Sample No.		δ(nm) from the growth time	δ(nm) from XRR measurement	Interface-roughness between (Ga,Mn)As layer and (Al,Ga,Mn)As layer	Interface-roughness between (Ga,Mn)As layer and top oxidized layer
S4	As-grown	-3	/	/	/
	Annealed		/	/	/
S2	As-grown	1	1.10±0.05	~0.1 (<0.3)	0.3±0.1
	Annealed		1.25±0.1	~0.2 (<0.3)	~0.2 (<0.3)
S6	As-grown	1-2	1.25±0.05	~0.15 (<0.2)	0.15±0.05
	Annealed		1.25±0.1	~0.1 (<0.3)	~0.1 (<0.25)
S5	As-grown	2	2.05±0.1	0.5±0.1	0.70±0.05
	Annealed		2.5±0.1	0.5±0.1	0.3±0.1
S1	As-grown	3	2.9±0.2	0.45±0.1	0.45±0.1
	Annealed		3.3±0.1	0.4±0.1	0.2±0.1
S3	As-grown	3	2.9±0.1	0.5±0.1	0.9±0.1
	Annealed		2.8±0.1	0.6±0.1	1.1±0.4

Table 4.2 *The simulation results of each sample. The min and max values of parameters are calculated by the error analysis function in the X'Pert Reflectivity software. (With error percentage =5%. It means the Parameter values which gave a fit value of 105% times the original fit value are tabulated as the "Min" and "Max" values.) More information about the simulation can be found in software user's manual.*

4.5 Conclusions of (Al,Ga,Mn)As based heterostructures

Different samples from 6 separate wafers with δ in the range -3nm to 3nm have been studied. After annealing, the characteristics of the measured remnant moment fall into two categories. Either a large moment remains along the [001] direction and a single transition is observed in the in-plane direction, indicating a suppression of the interstitial Mn diffusion from the bottom layer, as for sample S1, S3 and S5, or the moment along the [001] direction diminishes and two distinct transitions are observed in the magnetization in the plane, indicating diffusion of the interstitial Mn from the bottom layer, as for sample S2, S4 and S6.

The suppression of the diffusion of interstitial Mn from the bottom layer occurs for 3 samples for which $\delta \geq 3$nm and (Ga,Mn)As/(Al,Ga,Mn)As interface-roughness ≥ 0.3nm, and for 2 of these samples the easy axis of the top $(Ga_{0.914}Mn_{0.086})As$ layer is along the [110] direction. For all other samples the easy axis of the top

$(Ga_{0.914}Mn_{0.086})As$ layer is along the [1-10] direction. It can be speculated that the suppression of interstitial Mn diffusion occurs as a result of the formation of deep-level defects (*e.g.* Ga_{As} anti-sites, Ga interstitials or As vacancies) in the region under the interface between (Ga,Mn)As and (Al,Ga,Mn)As layers. Such defects are encouraged to form by growing with a deficiency of As. In the highly p-type (Ga,Mn)As and (Al,Ga,Mn)As layers, such defects act as electron donors, as do interstitial Mn. Therefore, the positively charged defects will form an electrostatic barrier close to the interface, opposing the diffusion of interstitial Mn and reducing T_C. On the other hand, the defects increase the interface-roughness which can be detected by the XRR measurements. That can explain why the T_C of (Al,Ga,Mn)As layer (after annealing) appear to be strongly correlated with the (Ga,Mn)As/(Al,Ga,Mn)As interface-roughness.

It has been shown that by growing heterostructures based upon (Al,Ga,Mn)As layers it is possible to suppress the diffusion of interstitial Mn by growing a region close to the interface between the layers with a deficiency of As. Two types of samples for which the bottom (Al,Ga,Mn)As layers have different annealing effects, magnetic anisotropy, and magnetization switching behaviors (coupled and uncoupled with the top layer) can be achieved by controlling the growth conditions. This technique will be useful for growing heterostructures with desired magnetic properties for studies of phenomena such as TMR, TAMR and STT. However, the high interface-roughness of samples S1 S3 and S5 could cause problems for device quality. For this reason in addition to the (Al,Ga,Mn)As based heterostructures, we have also investigated (Ga,Mn)(As,P) based bilayer structures as discussed in next section.

4.6 (Ga,Mn)(As,P) based heterostructure

Ref. 4 and 5 reported that the magnetic easy axis of $(Ga_{0.94}Mn_{0.06})(As_{1-y},P_y)$ with y >10% turns from in-plane to out of plane after annealing. It is expected that a fully annealed (Ga,Mn)As/(Ga,Mn)(As,P) bilayer sample will have two different magnetic easy axes perpendicular to each other, which may be useful for magnetotransport studies as with the (Al,Ga,Mn)As based heterostructures.

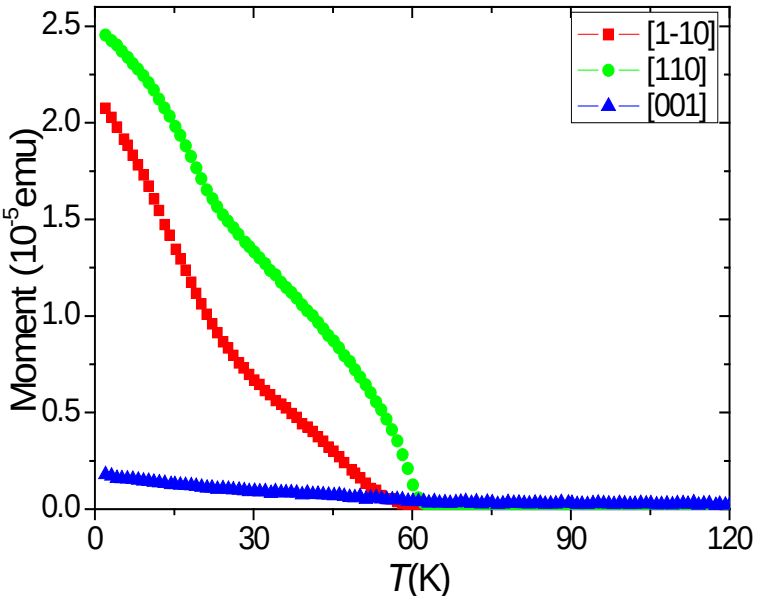

Figure 4.17 *Projection of the temperature dependent remnant moment measured after 1000 Oe field cool for the as-grown (Ga,Mn)As/(Ga,Mn)(As,P) bilayer sample*

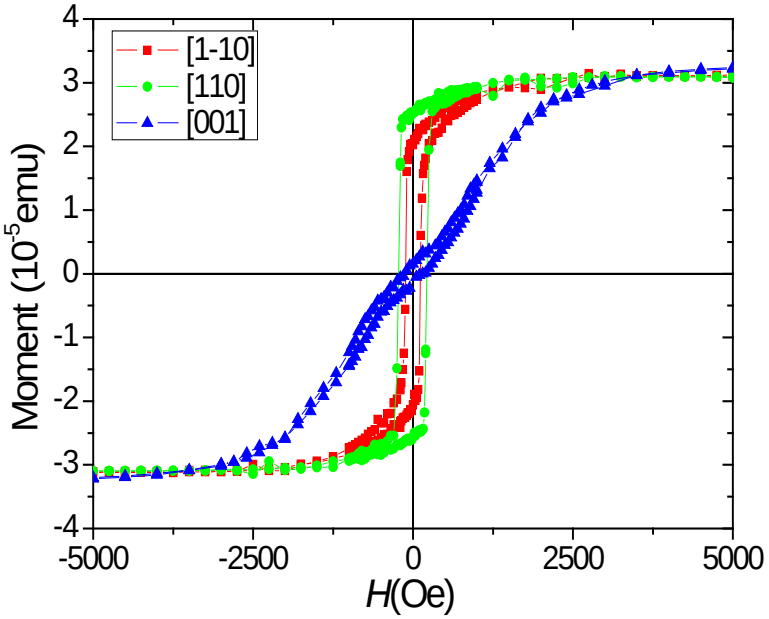

Figure 4.18 *The magnetic hysteresis loop of as-grown sample measured at 2K along [1-10], [110] and [001] directions*

A (Ga,Mn)As/(Ga,Mn)(As,P) bilayer wafer with 40nm $(Ga_{0.94}Mn_{0.06})As$ as top and 20nm $(Ga_{0.94}Mn_{0.06})(As_{0.85}P_{0.15})$ as bottom has been grown by MBE technique. Measured in SQUID, the projection of remnant moment curves along both [1-10] and [110] directions suggest there is a paramagnetic-to-ferromagnetic phase transition around 60K, (Figure **4.17**) and obviously the kinks for both curves indicate there is another transition around 25K. Because the incorporation of P reduces T_C of (Ga,Mn)As system, [4] it is concluded that T_C is about 25K for (Ga,Mn)(As,P) and 60K for (Ga,Mn)As layer. Both layers show the in-plane magnetic easy axis from the figures of remnant moment and hysteresis loop (Figure **4.18**). After 5 days annealing at 180°C, T_C increases to 68K for (Ga,Mn)(As,P) and 123K for (Ga,Mn)As layer, which suggests there is no suppression of diffusion of interstitial Mn in the bottom layer. (Figure **4.19**) The magnetic easy axis of (Ga,Mn)(As,P) layer turns to out of plane while (Ga,Mn)As layer still has in-plane anisotropy. (Figure **4.20**)

The future work of the (Ga,Mn)As/(Ga,Mn)(As,P) heterostructure is the fabrication of a mesa structure (Figure **4.21**) for current-perpendicular-to plane magnetotransport measurements. It is expected a large magnetoresistance can be observed.

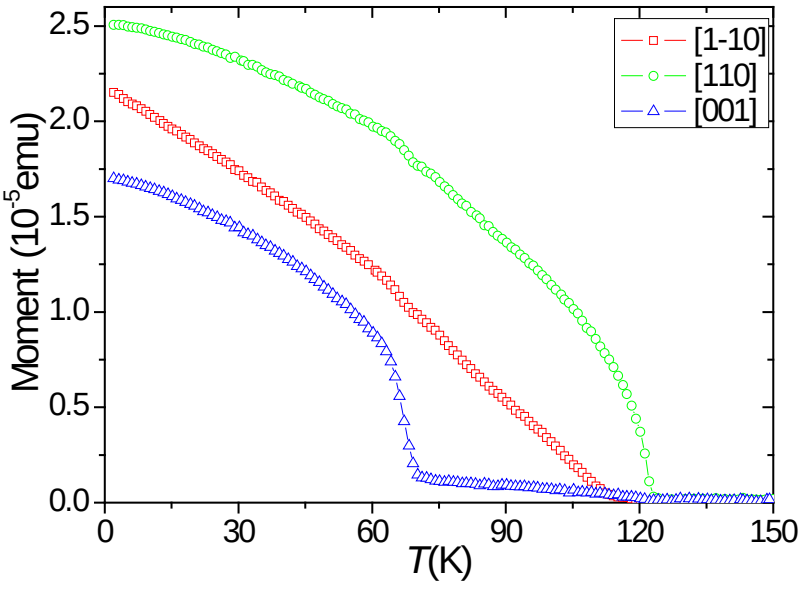

Figure 4.19 *Projection of the temperature dependent remnant moment measured after 1000 Oe field cool for the fully annealed (Ga,Mn)As/(Ga,Mn)(As,P) bilayer sample .*

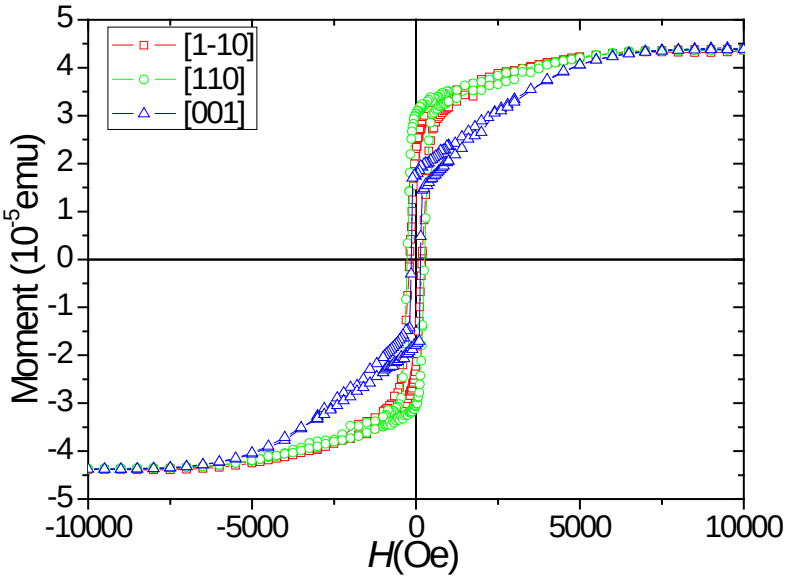

Figure 4.20 *The magnetic hysteresis loop of fully annealed sample measured at 2K along [1-10], [110] and [001] directions*

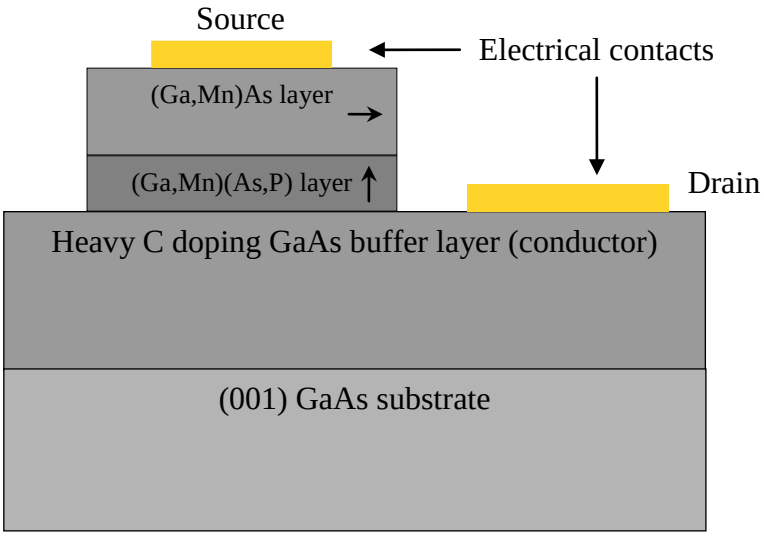

Figure 4.21 *The mesa structure of fully annealed (Ga,Mn)As/(Ga,Mn)(As,P) bilayer sample for magnetoresistance research*

References

[1] T. Jungwirth, Jairo Sinova, J. Masek, J. Kucera, and A. H. MacDonald, Rev. Mod. Phys. **78**, 809 (2006).

[2] M. Sawicki, K. Y. Wang, K. W. Edmonds, R. P. Campion, C. R. Staddon, N. R. S Farley, C. T. Foxon, E. Papis, E. Kaminska, A. Piotrowska, T. Dietl, and B. L. Gallagher, Phys. Rev. B **71**, 121302(R) (2005).

[3] A. W. Rushforth, N. R. S. Farley, R. P. Campion, K. W. Edmonds, C. R. Staddon, C. T. Foxon, B. L. Gallagher, and K. M. Yu, Phys. Rev. B. **78**, 085209 (2008).

[4] A. W. Rushforth, M. Wang, N. R. S. Farley, R. P. Campion, K. W. Edmonds, C. R. Staddon, C. T. Foxon, and B. L. Gallagher, J. Appl. Phys. **104**, 073908 (2008).

[5] A. Casiraghi, A. W. Rushforth, M. Wang, N. R. S. Farley, P. Wadley, J. L. Hall, C. R. Staddon, K. W. Edmonds, R. P. Campion, C. T. Foxon, and B. L. Gallagher, Appl. Phys. Lett. **97**, 122504 (2010).

[6] A. Lemaître, A. Miard, L. Travers, O. Mauguin, L. Largeau, C. Gourdon, V. Jeudy, M. Tran, and J.-M. George, Appl. Phys. Lett. **93**, 021123 (2008).

[7] M. Cubukcu, H. J. von Bardeleben, Kh. Khazen, J. L. Cantin, O. Mauguin, L. Largeau, and A. Lemaître, Phys. Rev. B **81**, 041202 (2010).

[8] P. R. Stone, J. W. Beeman, K. M. Yu, and O. D. Dubon, Physica B **401–402**, 454 (2007).

[9] P. R. Stone, K. Alberi, S. K. Z. Tardif, J. W. Beeman, K. M. Yu, W. Walukiewicz, and O. D. Dubon, Phys. Rev. Lett. **101**, 087203 (2008).

[10] M. Sawicki, D. Chiba, A. Korbecka, Y. Nishitani, J. A. Majewski, F. Matsukura, T. Dietl, and H. Ohno, Nat. Phys. **6**, 22 (2009).

[11] I. Stolichnov, S. W. E. Riester, H. J. Trodahl, N. Setter, A. W. Rushforth, K. W. Edmonds, R. P. Campion, C. T. Foxon, B. L. Gallagher, and T. Jungwirth, Nat. Mat. **7**, 464 (2008).

[12] A. W. Rushforth, E. De Ranieri, J. Zemen, J. Wunderlich, K. W. Edmonds, C. S. King, E. Ahmad, R. P. Campion, C. T. Foxon, B. L. Gallagher, K. Vyborny, J. Kucera, and T. Jungwirth, Phys. Rev. B **78**, 085314 (2008).

[13] E. De Ranieri, A. W. Rushforth, K. Vyborny, U. Rana, E. Ahmed, R. P. Campion, C. T. Foxon, B. L. Gallagher, A. C. Irvine, J. Wunderlich, T. Jungwirth, N. J. Phys. **10**, 065003 (2008);

[14] M. Overby, A. Chernyshov, L. P. Rokhinson, X. Liu, and J. K. Furdyna, Appl. Phys. Lett. **92**, 192501 (2008).

[15] S. T. B. Goennenwein, M. Althammer, C. Bihler, A. Brandlmaier, S. Geprags, M Opel, W. Schoch, W. Limmer, R. Gross, and M. S. Brandt, Phys. Status. Solidi (RRL) **2**, 96 (2008).

[16] R. Mattana, M. Elsen, J. -M. George, H. Jaffrès, F. Nguyen Van Dau, and A. Fert, M. F. Wyczisk, J. Olivier, and P. Galtier, B. Lépine, A. Guivarc'h, and G. Jézéquel, Phys. Rev. B **71**, 075206 (2005).

[17] C. Gould, C. Rüster, T. Jungwirth, E. Girgis, G. M. Schott, R. Giraud, K. Brunner, G. Schmidt, and L. W. Molenkamp, Phys. Rev. Lett. **93**, 117203 (2004).

[18] C. Rüster, C. Gould, T. Jungwirth, J. Sinova, G. M. Schott, R. Giraud, K. Brunner, G. Schmidt, and L. W. Molenkamp, Phys. Rev. Lett. **94**, 027203 (2005).

[19] M. Elsen, O. Boulle, J. -M. George, H. Jaffrès, R. Mattana, V. Cros, A. Fert, A. Lemaitre, R. Giraud, and G. Faini, Phys. Rev. B **73**, 035303 (2006).

[20] K. W. Edmonds, P. Boguslawski, K. Y. Wang, R. P. Campion, S. V. Novikov, N. R. S. Farley, B. L. Gallagher, C. T. Foxon, M. Sawicki, T. Dietl, M. B. Nardelli, and J. Bernholc, Phys. Rev. Lett. **92**, 037201 (2004).

[21] K. W. Edmonds, P. Boguslawski, K. Y. Wang, R. P. Campion, S. V. Novikov, N. R. S. Farley, B. L. Gallagher, C. T. Foxon, M. Sawicki, T. Dietl, M. B. Nardelli, and J. Bernholc, Phys. Rev. Lett. **94**, 139702 (2005).

[22] M. B. Stone, K. C. Ku, S. J. Potashnik, B. L. Sheu, N. Samarth, and P. Schiffer, Appl. Phys. Lett. **83**, 4568 (2003).

[23] D. Chiba, K. Takamura, F. Matsukura, and H. Ohno, Appl. Phys. Lett. **82**, 3020 (2003).

[24] M. Adell, L. Ilver, J. Kanski, V. Stanciu, P. Svedlindh, J. Sadowski, J.Z. Domagala, F. Terki, C. Hernandez, and S. Charar, Appl. Phys. Lett. **86**, 112501 (2005).

[25] K. Y. Wang, M. Sawicki, K.W. Edmonds, R. P. Campion, S. Maat, C. T. Foxon, B. L. Gallagher, and T. Dietl, Phys. Rev. Lett. **95**, 217204 (2005).

[26] T. Jungwirth, K. Y. Wang, J. Mašek, K. W. Edmonds, J. König, J. Sinova, M. Polini, N. A. Goncharuk, A. H. MacDonald, M. Sawicki, A. W. Rushforth, R. P. Campion, L. X. Zhao, C. T. Foxon, and B. L. Gallagher, Phys. Rev. B **72**, 165204 (2005).

[27] U. Welp, V. K. Vlasko-Vlasov, A. Menzel, H. D. You, X. Liu, J. K. Furdyna, and T. Wojtowicz, Appl. Phys. Lett. **85**, 260 (2004).

[28] T. Uemura, M. Harada, T. Akiho, K. Matsuda, and M. Yamamoto, Appl. Phys. Lett. **98**, 102503 (2011).

[29] K. Olejník, M. H. S. Owen, V. Novák, J. Mašek, A. C. Irvine, J. Wunderlich, and T. Jungwirth, Phys. Rev. B **78**, 054403 (2008).

[30] C. Myers, B. L. Sheu, A. W. Jackson, A. C. Gossard, P. Schiffer, N. Samarth, and D. D. Awschalom, Phys. Rev. B **74**, 155203 (2006).

Chapter 5

Conclusion and future work

5.1 Conclusion

This thesis discusses research work on III-V ferromagnetic semiconductors (Ga,Mn)As, (Ga,Mn)As with hydrogen doping, and (Al,Ga,Mn)As and single layers or heterostructures. Appendix A will discuss the detailed magnetometry studies of (Ga,Mn)(As,P) samples with different phosphorus percentage. All the III-V ferromagnetic semiconductors have interesting behaviours which are useful for science research in the spintronics area.

Investigations of the magnetic and transport properties of (Ga,Mn)As indicate T_C is extremely sensitive to the growth temperature and As:(Ga+Mn) ratio, the annealing, and the etching process. The precise control of MBE growth and post-growth annealing is important for achieving high T_C. Studies of H-doped (Ga,Mn)As, including carrier densities, the magnetizations and T_C show that the as-grown and lightly annealed samples have relatively high Curie temperatures down to low hole densities which make them good candidates for showing strong gate control of ferromagnetism. The probable explanation is localisation length is relatively small so that the measured hole density is that of delocalised holes while the number of holes

mediating ferromagnetism is larger. In addition, the magnetometry and magnetotransport measurements of control samples indicate the nominal 12% (Ga,Mn)As sample still follow the Zener mean field model. Studies of (Al,Ga,Mn)As heterostructures demonstrate a method to suppress the diffusion of interstitial Mn ions from bottom layer during low temperature annealing. This effect is due to an electrostatic barrier formed by positively charged defects (*e.g.* Ga_{As} anti-sites, Ga interstitials or As vacancies which can increase the increase the interface roughness), and can be controlled by growing different thickness of As deficient layer before starting the growth of top layer. The (Al,Ga,Mn)As and (Ga,Mn)(As,P) based heterostructures in which individual layers have tailored magnetic properties are useful for studies of magnetoresistance and spin torque phenomena.

5.2 Future work

There is still some unfinished work for each chapter. (Ga,Mn)As is an important test-bed material for spintronics, and there are many interesting properties which can be investigated. It is obvious that the production of (Ga,Mn)As with high percentage of substitutional Mn becomes more and more difficult. The record T_C is below 200K, far from the room temperature. However, the ultimate limit of T_C is still unknown. It is possible to improve the growth and post-growth process in order to achieve higher T_C. The conclusion part of Chapter 3 suggests a model of H-doped (Ga,Mn)As which needs more theoretical work to prove. The future work of (Al,Ga,Mn)As and (Ga,Mn)(As,P) based heterostructures is the design and fabrication of device for magnetotransport measurements. Additionally, a lot of interesting work of III-V ferromagnetic semiconductors involves new techniques and new materials which will be discussed in the next sections.

5.2.1 Electrostatic gating of (Ga,Mn)As

A lot of studies of gate effect on (Ga,Mn)As have been done by Chiba *et al.* [1,2]and Sawicki *et al.* [3] The results indicate the magnetic properties of (Ga,Mn)As can be manipulated by using electric fields to change the carrier concentration. (Figure **5.1** and Figure **5.2**) There are some materials in this thesis that could be good candidates

to show gate effect, including the H-doped (Ga,Mn)As samples with low hole densities, the (Ga,Mn)As with high As:(Ga+Mn) growth ratio (It has more As anti-site defects, but still shows ferromagnetic behaviour with low hole densities.), also the (Al,Ga,Mn)As based heterostructure and the (Ga,Mn)Sb material which will be discussed in the next section.

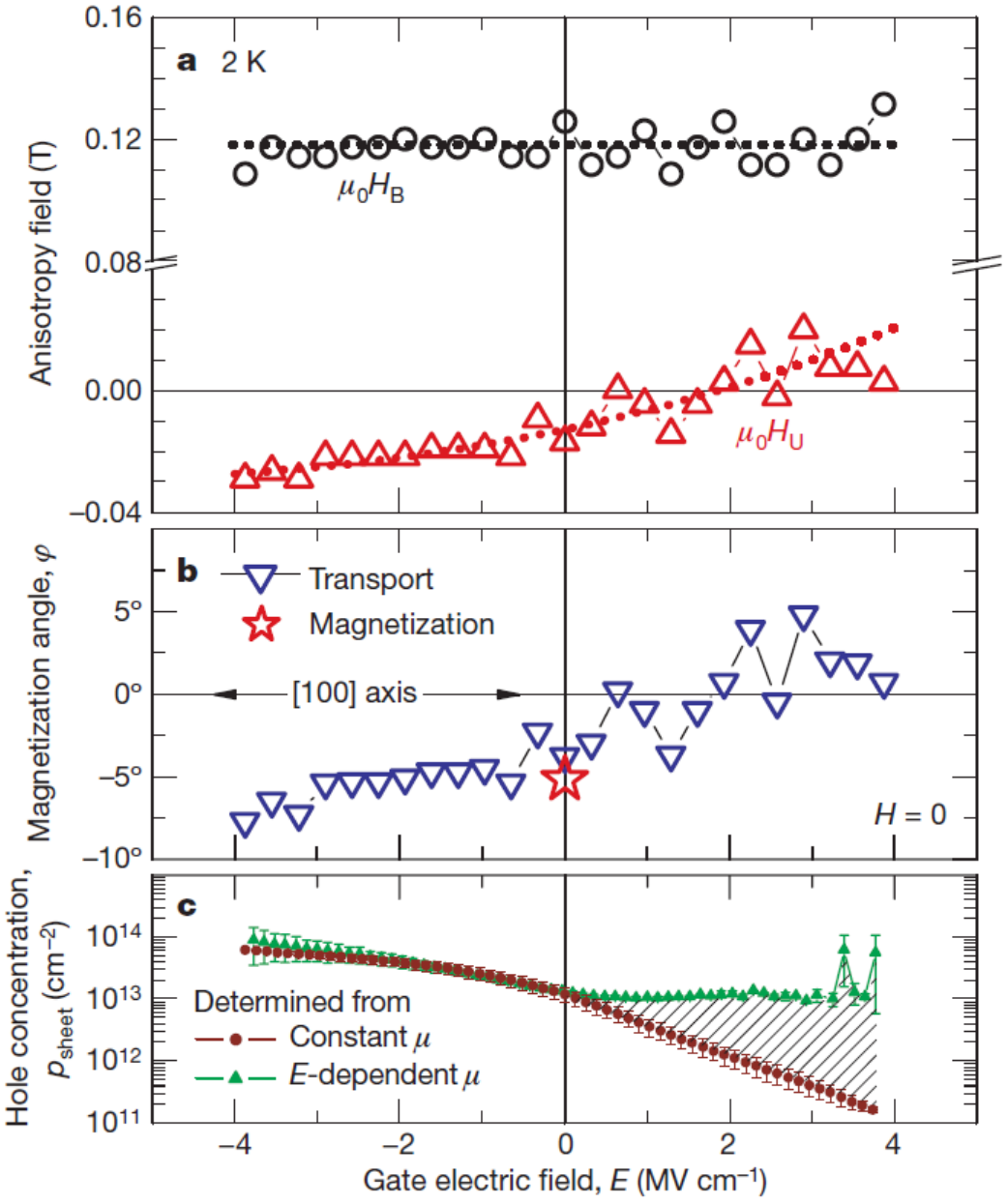

Figure 5.1 *Anisotropy fields, magnetization angle and sheet hole concentration as functions of electric field. Taken from ref.* 2

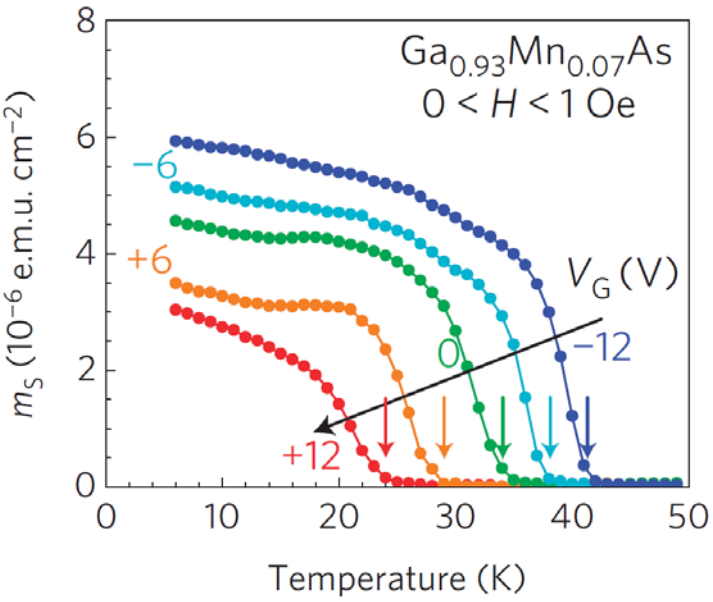

Figure 5.2 *Temperature dependence of the spontaneous moment for different values of gate voltage V_G. Taken from ref.* 3

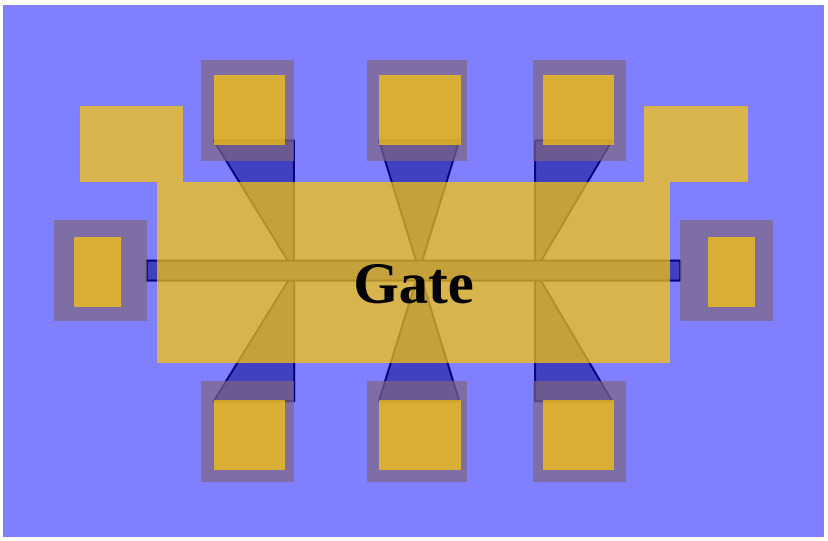

Figure 5.3 *The gate structure on Hall bar for magnetotransport measurements. The whole structure of Hall bar is covered by dielectric layer (blue colored area) Golden parts are the electrical contacts.*

One part of the future work is making gate structure for applying large gate voltage without any gate current leaking. (Figure **5.3**) It is important to find a growth technique (*e.g.* plasma enhanced chemical vapor deposition (PECVD), atomic layer deposition (ALD)) to grow a high quality dielectric layer (*e.g.* SiO_2, Si_4N_3, Al_2O_3) between the gate contact and the ferromagnetic semiconductor layer.

5.2.2 (Ga,Mn)Sb ferromagnetic semiconductor

The III-V semiconductor GaSb has a narrow band gap of 0.726eV (at 300K), which means much shallower acceptor level of Mn in GaSb than that in GaAs. [4] Doping of GaSb by Mn offers yet another opportunity to investigate the chemical trends of the interaction between transition metal ions and carriers without the use of additional doping. [5] Previous studies have shown that (Ga,Mn)Sb grown on ZnTe, GaSb [6] and $(Al_{0.8}Ga_{0.2})Sb$ [7] have ferromagnetic order with T_C =12K, 15K and 25K respectively. The (Ga,Mn)Sb has perpendicular anisotropy easy axis when under tensile strain with ZnTe and $(Al_{0.8}Ga_{0.2})Sb$ buffer layer, and has in-plane anisotropy when under compressive strain with GaSb buffer layer. Transport studies showed that (Ga,Mn)Sb is more metallic than (Ga,Mn)As, probably due to the difference of Mn acceptor level. (16meV in GaSb [4], 110meV in GaAs [8]) Ref. 7 also reports that T_C and magnetic anisotropy field can be controlled by applying electric field.

Recently, a 25nm $(Ga_{0.94}Mn_{0.06})Sb$ layer on InAs substrate has been grown and some magnetic characterizations have been performed in the Nottingham group. The $(Ga_{0.94}Mn_{0.06})Sb$ layer shows ferromagnetism below about 30K with in-plane uniaxial anisotropy easy axis along [1-10] direction. (Figure **5.4**) Different from GaAs based ferromagnetic semiconductors, a 48 hour post-growth annealing at 180^{o}C in air has little effect on the magnetic properties of the sample. (Figure **5.5**)

Further studies of the crystal structure, magnetic and transport properties will be done in the future. As said before, (Ga,Mn)Sb is a good candidate for showing an electrical gate effect on the ferromagnetism. However, due to the high conductivity of InAs, it is necessary to grow an insulating buffer between (Ga,Mn)Sb layer and InAs substrate before performing transport measurements.

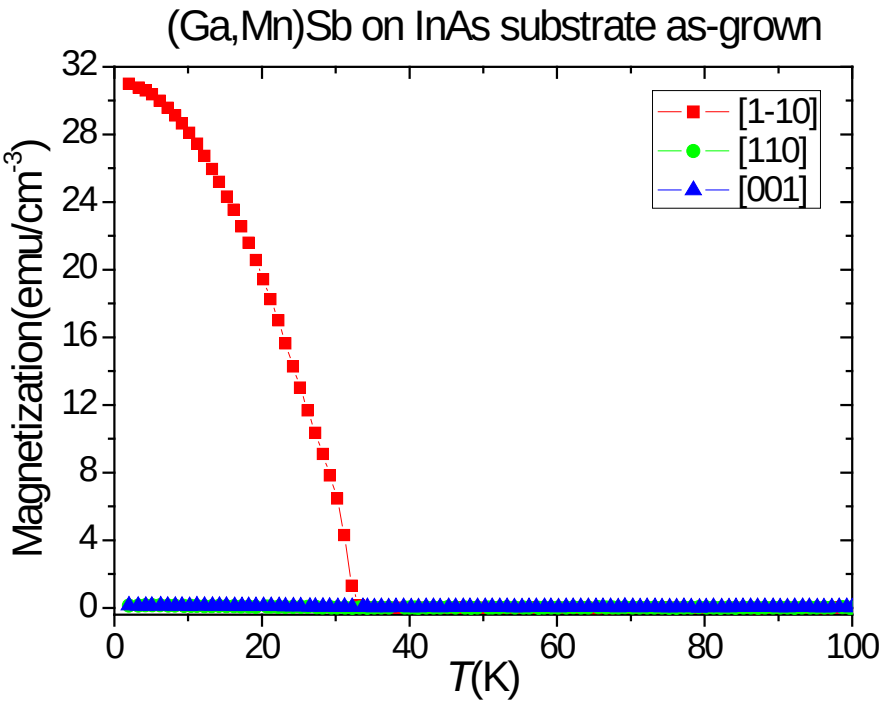

Figure 5.4 *Temperature dependence of the remnant magnetization for as-grown (Ga,Mn)Sb on InAs substrate.*

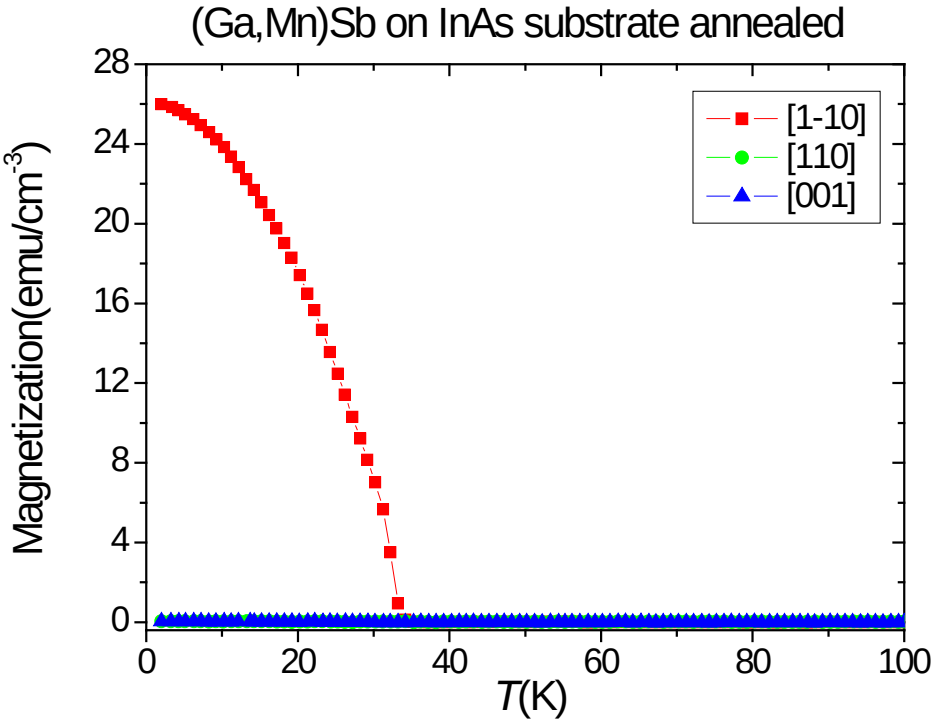

Figure 5.5 *Temperature dependence of the remnant magnetization for 48 hours annealing at 180ºC (Ga,Mn)Sb on InAs substrate.*

References

[1] D. Chiba, F. Matsukura, and H. Ohno, Appl. Phys. Lett. **89**, 162505 (2006).

[2] D. Chiba, M. Sawicki, Y. Nishitani, Y. Nakatani, F. Matsukura and H. Ohno, Nature **455**, 515 (2008).

[3] M. Sawicki, D. Chiba, A. Korbecka, Y. Nishitani, J. A. Majewski, F. Matsukura, T. Dietl and H. Ohno, Nature Physics **6**, 22 (2010).

[4] V. Šestáková, P. Hubík, B. Štěpánek and J. Krištofik, J. Crystal Growth **132**, 345 (1993).

[5] E. Abe, F. Matsukura, H. Yasuda, Y. Ohno and H. Ohno, Physica E **7**, 981 (2000).

[6] W.L. Lim, T. Wojtowicz, X. Liu, M. Dobrowolska, J.K. Furdyna, Physica E **20**, 346 (2004).

[7] Y. Nishitani, M. Endo, F. Matsukura and H. Ohno, Physica E **42**, 2681 (2010).

[8] R. A. Chapman and W. G. Hutchinson, Phys. Rev. Lett. **18**, 443 (1967).

Appendix A

Magnetic properties of ferromagnetic semiconductor (Ga,Mn)(As,P)

This appendix presents an experimental investigation of the magnetic properties of $(Ga_{0.94}Mn_{0.06})(As_{1-y}P_y)$ single layers on GaAs substrates for $y \leq 0.3$ with perpendicular anisotropy easy axis after annealing.

A.1 Motivation of investigate (Ga,Mn)(As,P)

While making great efforts to increase T_C in (Ga,Mn)As, it is also interesting to look through the other III-V hosts. A theoretical study of the structural and magnetic properties of the (Ga,Mn)(As,P) system, predicted sizeable enhancements of T_C for a range of P doping levels.[1] GaP has a smaller lattice constant than GaAs, favouring a stronger exchange interaction when doped with Mn, but has a wider band gap resulting in stronger localisation of the holes. Initial experimental investigations on GaP doped with Mn by ion implantation suggest that the Fermi level resides in an impurity band with a relatively low T_C=60K [2]. This appendix presents some experimental results of the (Ga,Mn)(As,P) system for P doping levels in the range 10-30%.

A.2 MBE growth of the sample

Three wafers with different P doping levels were grown based on the method of producing 6% (Ga,Mn)As wafers. The difference is that a 50nm low temperature $Ga(As_{1-y},P_y)$ buffer layer was grown before the 25nm $(Ga_{0.94}Mn_{0.06})(As_{1-y},P_y)$ layer with nominal doping y= 0.1, 0.2 and 0.3. The P concentration was varied by increasing the P pressure and decreasing the As pressure to compensate. All the samples were studied before and after annealing in air at 180^0C for 48 hours-a standard technique for removing interstitial Mn, as mentioned before.

A.3 Magnetic properties study

The magnetic anisotropy of (Ga,Mn)As films depends upon the carrier density and the lattice strain [3]. For Mn concentrations ≥2% the magnetic anisotropy of (Ga,Mn)As tends to show easy axes in the plane when the (Ga,Mn)As layer is under compressive strain on a GaAs substrate. The easy axis points out of the plane when the (Ga,Mn)As layer is under tensile strain, such as when grown on a relaxed (In,Ga)As buffer [4]. As shown in Figure **A.1**, the annealed (Ga,Mn)(As,P) samples show easy axes out of the plane with the magnetic anisotropy increasing as the P concentration increases. This is consistent with the increasing tensile strain for increasing P concentration. The as grown samples all have the magnetic easy axis in the plane. This may be a result of the low carrier density in these heavily compensated films [3]. The magnetic properties were measured using the SQUID magnetometer. For the as-grown samples the Curie temperatures were 66K, 29K, 12K and 11K for y=0, 0.1, 0.2 and 0.3 respectively. The samples were electrically insulating at low temperatures indicating a high degree of carrier compensation. We shall concentrate mainly on the results for annealed samples. Upon annealing the Curie temperatures increase dramatically to 136K, 109K, 79K and 76K for y=0, 0.1, 0.2 and 0.3 respectively.(Figure **A.2**)

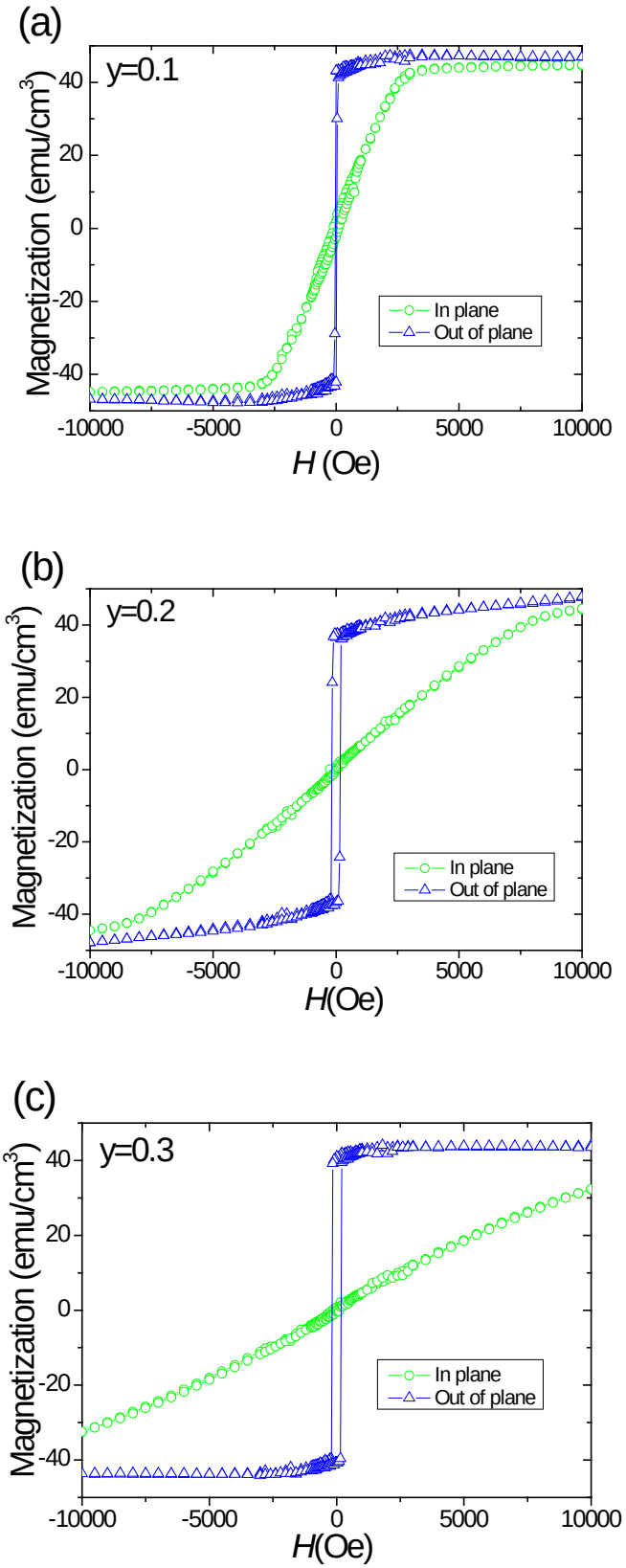

Figure A.1 *Magnetic hysteresis loops measured at 2K for external magnetic field applied in the plane (green curves) and perpendicular to plane (blue curves) for annealed* $(Ga_{0.94}Mn_{0.06})(As_{1-y}P_y)$ *layers with (a) y=0.1, (b)y=0.2 and (c) y=0.3.*

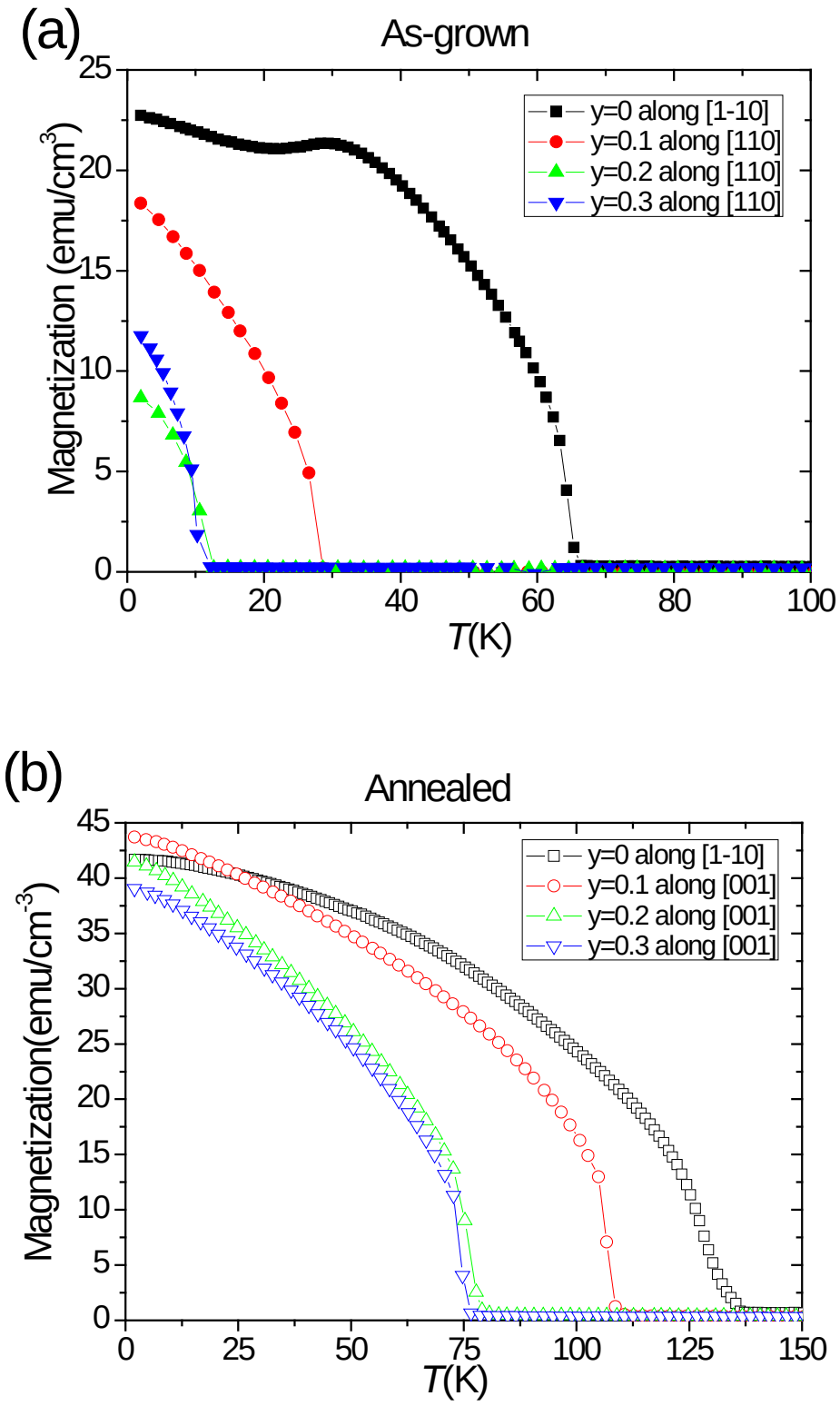

Figure A.2 *Projection of remnant magnetization vs. temperature for the (a) as-grown and (b) fully annealed* $(Ga_{0.94}Mn_{0.06})(As_{1-y}P_y)$ *layers with y=0, 0.1, 0.2 and 0.3 respectively.*

A.4 Conclusion

The investigations have shown that annealed $(Ga_{0.94}Mn_{0.06})(As_{1-y}P_y)$ layers with y $\leq$0.3 are metallic and are under tensile strain, resulting in a strong perpendicular to plane magnetic anisotropy which increases as y increases. Samples with metallic resistivity and tunable out of plane magnetic anisotropy and coercive field may find application in studies of micromagnetic phenomena. For y $\leq$0.1 T_C is comparable to the $(Ga_{0.94}Mn_{0.06})As$ control sample. The evolution of the magnetic anisotropy between an easy axis in the plane for the as-grown samples, to an easy axis perpendicular to the plane for fully annealed samples arises from the increase of the carrier density, as a result of annealing and more details can be found in ref. 5. Besides the magnetic properties, more results of crystal structure and magnetotransport properties of the (Ga,Mn)(As,P) have been reported in ref. 6.

References

[1] J. Măsek, J. Kudrnovsky, F. Maca, J. Sinova, A. H. MacDonald, R. P. Campion, B. L. Gallagher, and T. Jungwirth, Phys. Rev. B **75**, 045202 (2007).

[2] M. A. Scarpulla, B. L. Cardozo, R. Farshchi, W. M. H. Oo, M. D. McCluskey, K. M. Yu, and O. D. Dubon, Phys. Rev. Lett. **95**, 207204 (2005).

[3] T. Dietl, H. Ohno, and F. Matsukura, Phys. Rev. B **63**, 195205 (2001).

[4] A. Shen, H. Ohno, F. Matsukura, Y. Sugawara, N. Akiba, T. Kuroiwa, A. Oiwa, A. Endo, S. Katsumoto, Y. Iye, J. Cryst. Growth **175-176**, 1069 (1997).

[5] A. Casiraghi, A. W. Rushforth, M. Wang, N. R. S. Farley, P. Wadley, J. L. Hall, C. R. Staddon, K. W. Edmonds, R. P. Campion, C. T. Foxon, and B. L. Gallagher, Appl. Phys. Lett. **97**, 122504 (2010).

[6] A. W. Rushforth, M. Wang, N. R. S. Farley, R. P. Campion, K. W. Edmonds, C. R. Staddon, C. T. Foxon, and B. L. Gallagher, J. Appl. Phys. **104**, 073908 (2008).

Appendix B

Introduction to equipments

B.1 The Quantum Design Magnetic Property Measurement System (MPMS)

The Superconducting Quantum Interference Device (SQUID) is a very sensitive magnetometer used to measure extremely weak magnetic fields, based on superconducting loops containing Josephson junctions. The Josephson junction is a voltage-to-frequency converter usefully sensitive to voltage, current and magnetic fields that is made of a superconducting wire interrupted by an insulating weak-link. Ref. 1 and 2 are the background knowledge of the Josephson junction and the Josephson effect (the phenomenon of supercurrent across two superconductors coupled by the weak link), and the details of how to use the Josephson effect to detect weak magnetic fields in the SQUID system can be found in ref. 3 and 4.

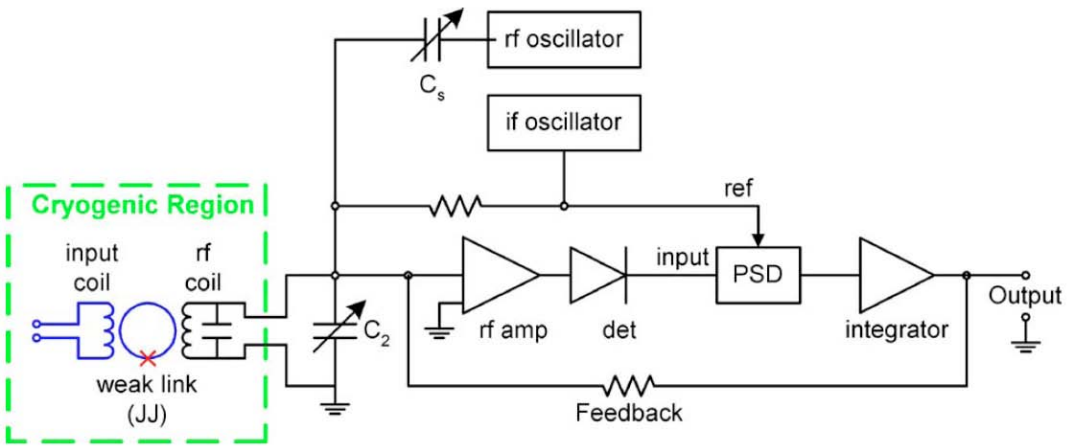

Figure B.1 *Block diagram of a typical RF SQUID [4]*

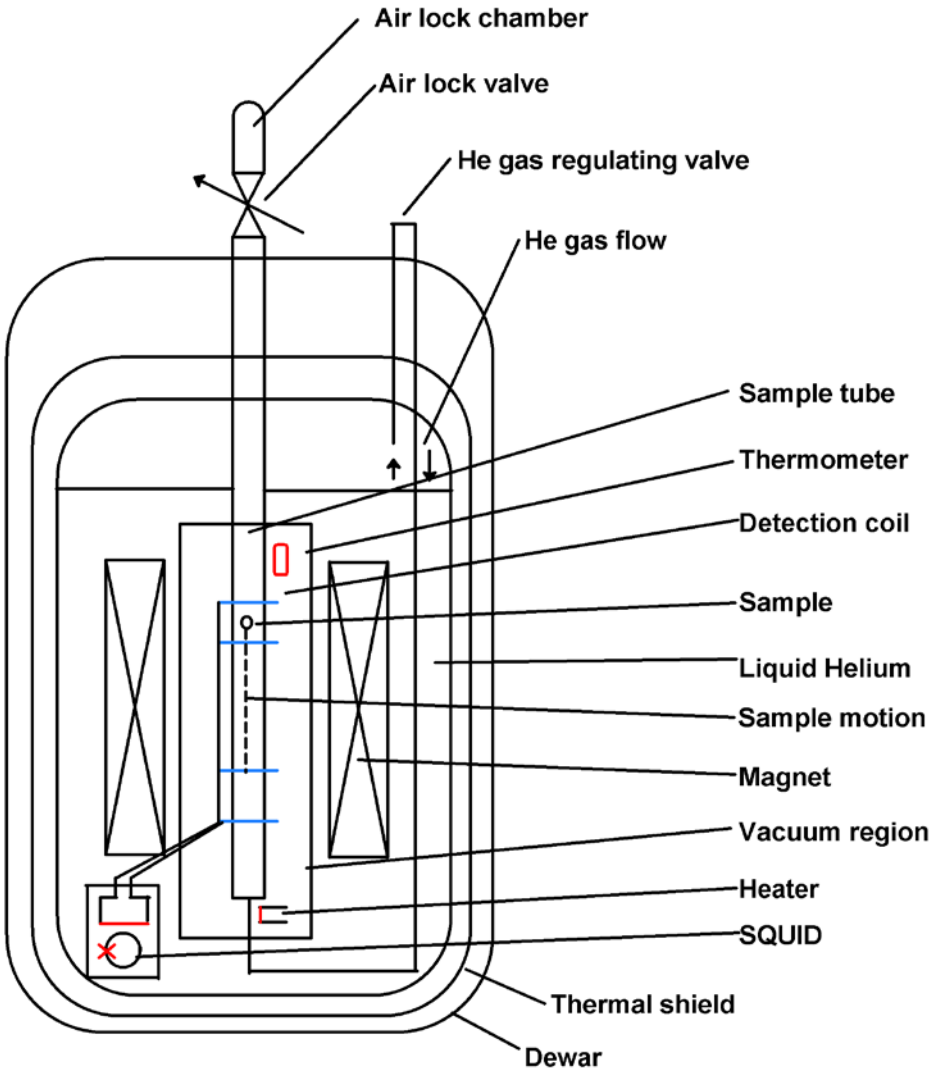

Figure B.2 *The schematic diagram of the MPMS [4]*

Utilizing the SQUID technology, combined with patented enhancements, the Quantum Design MPMS (Figure **B.2**) provides solutions for a unique class of sensitive magnetic measurements. The temperature range for the measurement is from 1.9K to 400K with the sweep rate range 0.001 to 10K/min. The stability is ±0.5% for the temperature between 1.9K and 4.2K. The high homogeneity superconducting magnet configurations provide up to 1 Tesla magnetic field with uniformity 0.01% over 4 cm. The maximum sample size can be measured is 9 mm. With the Reciprocating Sample Option (RSO), the absolute sensitivity value for DC magnetization measurement is 1×10^{-8} emu from 0 to 0.25T. For the AC susceptibility measurement from 0.1 Hz to 1 KHz, the sensitivity is $2\times l0^{-8}$ emu at 0T. The maximum magnetic moment can be measured is 5emu.

B.2 The Oxford Instruments "Variox" ^{4}He cryostat system with external magnet

The "Variox" provides a controlled low temperature sample environment, in which the sample is cooled through a static exchange gas. This system (Figure **B.3**) offers good temperature control and fast cools down times, and was used to perform magneto-transport measurements with external magnetic field.

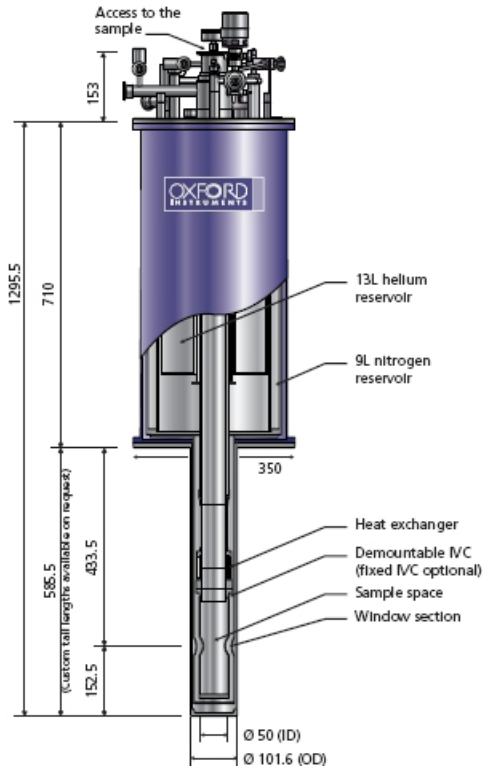

Figure B.3 *The layout and dimensions of "Variox" cryostat system (from the Oxford Instruments)*

The temperature of the sample space can be changed from 330K to 1.6K with typical cooling rate 0.1K/s. From room temperature (~300K) to 4.2 K, helium is continuous pumped through the sample space from the needle valve, being warmed to the required temperature by the heater block. The temperatures below 4.2K can be obtained by decreasing the ^{4}He pressure in the sample space with the rotary pump. The temperature of the heater block, which is measured with the $Au_{0.93}Fe_{0.07}$/Cr thermocouple calibrated at 77K and 4.2K, is controlled by an Oxford Instruments ITC503 temperature proportional integral derivative (PID) controller. The temperature of the sample is measured with a Cernox resistor on the sample probe which has been calibrated to better than 0.1 K accuracy.

A horizontal magnetic field is generated by a standard water-cooling electromagnet with the Kikusui PWR800L DC power supply which can provide a wide range of voltages (0-80V) and currents (0-50A) within the output power rating. The typical ramping rate from zero field to 0.6T (6000G) is about 5G/s. The magnet can be rotated horizontally 200 degrees, and the angle has been calibrated by the caliper within 0.5 degree accuracy. It is possible to apply the field along any arbitrary angle with respect to the sample by using a special probe which can rotate the sample in the vertical plane.

B.3 The Cryogenic liquid helium cryostat system with superconducting magnet

The Cryogenic cryostat system (Figure **B.4**) with the superconducting magnet can perform high field magnetotransport measurement, which is useful for measuring carrier densities of semiconductor materials. The Lakeshore 340 PID temperature controller with the Cernox sensor in the sample chamber gives a well control of temperature. (0.1K accuracy between 1.9K and 150K) The range of temperature change rate can be between 0.1K/min and 10K/min.

The magnetic field is generated by the Nb_3Sn superconducting magnet with an additional λ-plate which allows superconducting magnet operation below 4.2K. Typically, the field strength of a superconducting magnet can be increased by more than 10% if the operating temperature is reduced from 4.2K to 2.2K. The λ-plate will maintain the magnet temperature at reduced temperatures for extended periods of time and is a cost effective way to obtain higher magnetic fields. The type of the power source for the superconducting magnet is Cryogenic SMS 120. The output current setting range is 0 to 120A, with setting resolution 1.8mA (readout resolution 0.001A) and the setting accuracy 1.8mA. The hold stability is 20ppm/hour. The output voltage setting range is 0 to 5V, with setting accuracy 20mV and resolution 0.1V. The digital ramp setting range is 10 to 100,000 seconds from zero to full output in 65 logarithmic steps, and the setting accuracy is 0.5% of the ramp rate set.

The recommended ramp rate is less than 0.7A/s. The switch heater (for changing the magnetic field) setting range is 0 to 8.0 V with 0.1V setting resolution and 100mA maximum current. For the superconducting magnet, the measured central field constant is calibrated and the value is 1497.3G/A. The maximum magnetic field achieved when the temperature of magnet is at 4.2K is 14.1T (the current is 93.5Amps) and 16.1T (106.85Amps) for 2.2K with homogeneity 0.1% over 10mm length. The coil inductance is around 48.5H.

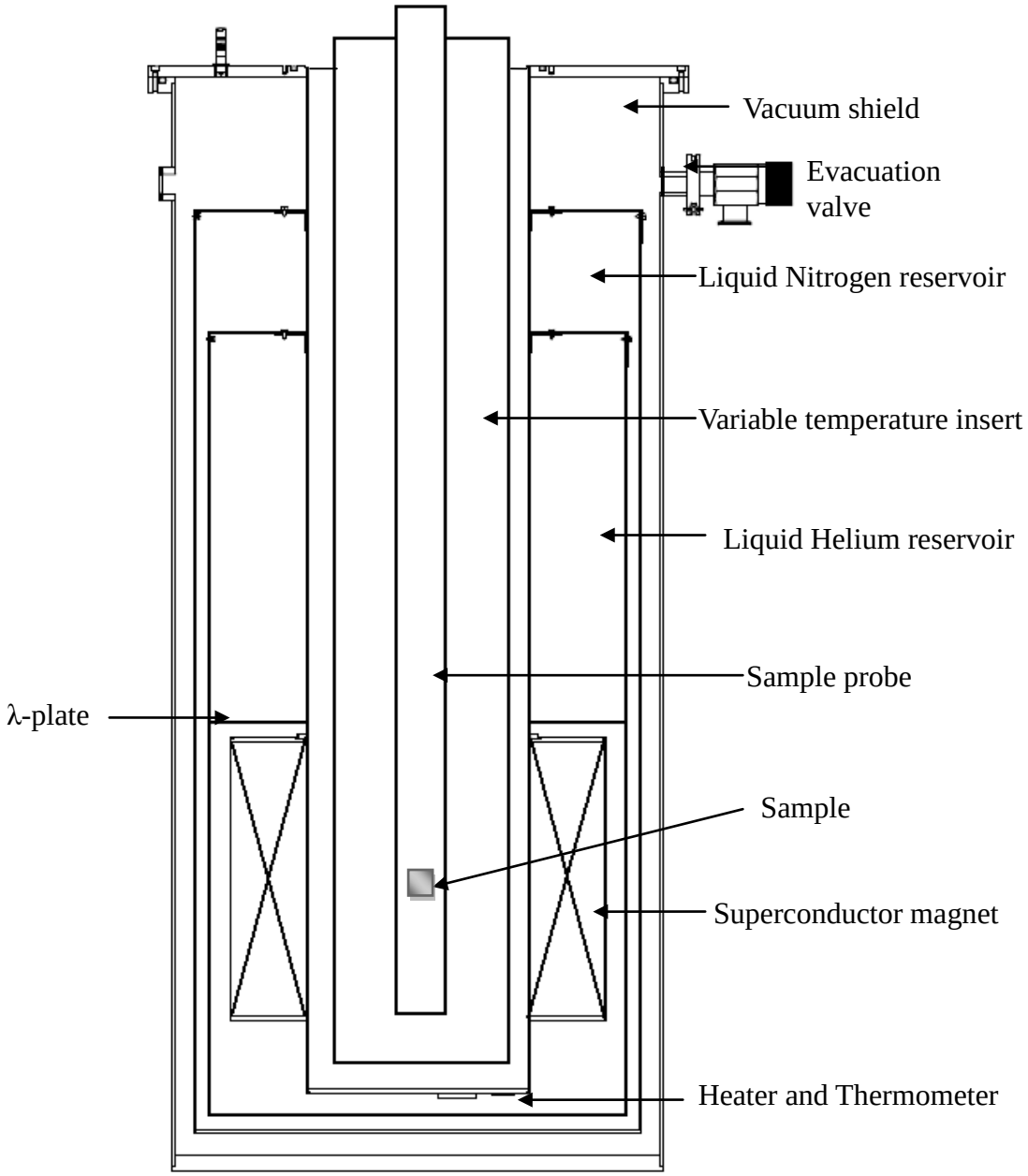

Figure B.4 *the block diagram of Cryogenic ^{4}He cryostat system with superconducting magnet*

B.4 The X'Pert Materials Research Diffractometer system

The X'Pert Materials Research Diffractometer (MRD) equipped with a Cu tube x-ray source was used for the x-ray reflectivity (XRR) measurement. (Figure **B.5**)A thin film attachment (for XRR measurement, includes a 0.1 mm slit between a parallel plate collimator and a flat secondary monochromator (Graphite)) is used for the reflectivity measurements. It is normally used with a divergence slit for the primary optics and the line focus. The 2θ resolution angle of the thin film attachment is 0.27º. A fine slit is required between the parallel plate collimator and the flat graphite monochromator to improve the 2θ resolution for reflectivity measurements. The flat graphite monochromator is used to improve the peak to background ratio in the measurements.

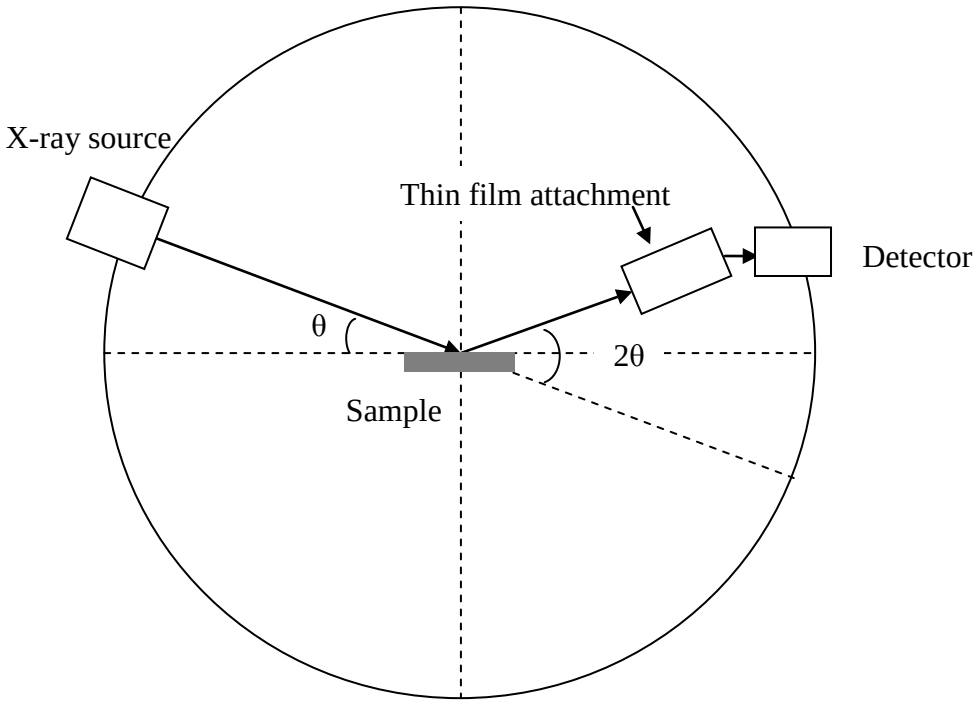

Figure B.5 *Schematic diagram of x-ray Diffractometer for the x-ray reflectivity (XRR) measurements.*

B.5 References

[1] B. D. Josephson, Phys. Lett. **1**, 251 (1962).

[2] B. D. Josephson, Rev. Mod. Phys. **46** (2), 251 (1974).

[3] A. Barone and G. Paterno, “Physics and Applications of the Josephson Effect.” New York: John Wiley & Sons. (1982).

[4] L. Fagaly, Rev. Sci. Instrum.**77**, 101101 (2006).

Appendix C

Magnetic Units

Name	Symbol	CGS units	SI units	Conversion
Magnetic B field Magnetic induction Magnetic flux density	**B**	Gauss (G)	Tesla(T)	$1T=10^4G$
Magnetic H field Magnetic field intensity Magnetic field strength Magnetic field	**H**	Oersted (Oe)	Ampere per meter (A/m)	$1A/m=4\pi\times10^{-3}Oe$
Magnetization	**M**	Electromagnetic units per cubic centimeter (emu/cm^3)	Ampere per meter (A/m)	$1A/m=10^{-3}emu/cm^3$

In CGS units, the relation between **B**, **H** and **M** is $\mathbf{B}=\mathbf{H}+4\pi\mathbf{M}$ and $1\mathrm{G}\equiv1\mathrm{Oe}\equiv\frac{1}{4\pi}\mathrm{emu/cm^3}$

In SI units, the relation between **B**, **H** and **M** is $\mathbf{B}=\mu_0(\mathbf{H}+\mathbf{M})$ where the permeability of free space $\mu_0=4\pi\times10^{-7}\,\mathrm{V\cdot s/(A\cdot m)}$